



Universidad Politécnica de Valencia
ESCUELA TÉCNICA SUPERIOR DE INGENIERÍA DEL DISEÑO

von Kármán Institute for Fluid Dynamics
AERONAUTICS AND AEROSPACE DEPARTMENT



Thermal Characterization of Ablative Materials

Torres Herrador, Francisco José

Supervisor VKI:
Thierry Magin

Advisors VKI:
Vincent Leroy
Bernd Helber

Supervisor UPV:
Laura Contat Rodrigo

March 6, 2018

Papa, siempre por ti.

Contents

Contents	I
List of Figures	III
List of Tables	VI
1 Introduction	1
2 Materials and Methods	8
2.1 Materials	8
2.2 Thermal Analysis Techniques	9
2.2.1 Differential Scanning Calorimetry	9
2.2.1.1 Specific heat capacity determination procedure (ISO 11357) . . .	10
2.2.2 Thermogravimetric Analysis	13
2.2.2.1 Kinetic Analysis of the Thermal Degradation Process	15
2.2.2.2 Numerical Methods	20
2.2.3 Thermal Analyzer at the VKI	27
3 Experimental methodology for heat capacity determination by DSC	31
3.1 Temperature Calibration	31
3.2 Heat Capacity accuracy verification	33
3.3 Experimental Campaign	34
3.4 Heat capacity results	37
3.4.1 Heat capacity of Graphite	38
3.4.2 Heat capacity of Preform	40
3.4.3 Heat capacity of Resin char	41
3.4.4 Heat capacity of Aterm char	43
4 TGA Curve Fitting — <i>FiTGA</i> Software Package	44
4.1 Fitting Algorithm	45
4.1.1 TGA Curve Reconstruction	45
4.1.2 Minimization Process	46
4.2 Sensitivity Analysis	47
4.2.1 Sensitivity Analysis using ANOVA	48
4.2.2 Sensitivity Analysis using Sobol Indices	49
4.2.2.1 Elementary Effects Test (EET)	49
4.2.2.2 Variance Based Sensitivity Analysis (VBSA)	50
4.2.2.3 Fourier Amplitude Sensitivity Analysis	52

4.2.2.4	Probability Distribution Function	53
4.3	Results of TGA Curve Fitting	54
4.3.1	Validation case: 2-reaction simulated data	55
4.3.2	Hybrid Genetic Algorithm test: two curves with different heating rates	56
4.3.3	Four-reaction experimental data fitting	57
5	Conclusions	60
5.1	Conclusions on DSC	60
5.2	Conclusions on TGA	60
5.3	Final Conclusions	61
6	Budget	62
Bibliography		63
Appendix A Simulation tools: <i>OpenFOAM</i> & <i>PATO</i>		70
A.1	<i>OpenFOAM</i>	70
A.2	<i>PATO</i>	72
Appendix B FiTGA User's Guide		74

List of Figures

1.1	Micrographs of LCAs.	3
1.2	Galileo Probe Heatshield [6]. Thickness distribution before and after reentry on Jupiter: almost all material ablated at the shoulder but stagnation point region was overestimated.	4
1.3	Different stages of pyrolysis as function of their temperature ranges [8].	5
1.4	Phenomenology of porous ablator material response [9]	6
2.1	Materials of analysis	9
2.2	Schemes of the two main types of DSC analyzers. It can be noted that the main differences are the location of the samples and the way used to calculate the heat.	10
2.3	DSC curve; striped areas correspond to different reactions	12
2.4	MDSC temperature increase scheme. The solid line is the actual temperature program. The dashed line is the linear increase ($\beta = 1 \text{ }^{\circ}\text{C} \cdot \text{min}^{-1}$) and the dot-dashed line is the derivative of the sinusoid curve ($T = 30 \text{ s}$, $A = 1 \text{ }^{\circ}\text{C}$) [24].	13
2.5	Schematic of a TGA analyzer. Adapted from “Thermal Characterization of Polymeric Materials” [23]	14
2.6	Example of thermogram depicting the mass loss during two different reactions of the pyrolysis process (arbitrary data). The left axis represents the TGA in terms of density ratio. The right axis is the DTGA; each peak indicates a reaction.	15
2.7	Advancement of the reaction. When $\chi = 0$ the reaction has not started, and when $\chi = 1$ the reaction has finished	16
2.8	Schematic of reaction types following model $f(\chi)$: 1 - Decelerating; 2 - Accelerating; 3 - Sigmoid [26]	17
2.9	Basic optimization scheme	21
2.10	2D representation of the Trust Region Algorithm. Adapted from “Numerical Optimization” [36]	23
2.11	Evolution of the population. It can be observed that in the final generation, one of the individuals is at the optimum. Adapted from “Numerical Optimization” [36] to exemplify the Trust-Region Algorithms.	26
2.12	NETZSCH 449 F3 Jupiter Simultaneous Thermal Analyzer. Courtesy of Netzschr GmbH.	27
2.13	Different components of the NETZSCH 449 F3 Jupiter Thermal Analyzer. Courtesy of NETZSCH GmbH.	29
2.14	Glovebox where the thermal analyzer is located at the VKI.	30
3.1	DSC curve for Zinc at $40 \text{ K} \cdot \text{min}^{-1}$. The onset temperature for melting is $419,8 \text{ K}$ which is close to the theoretical value ($419,5 \text{ K}$).	32

3.2	Quadratic fit obtained for the temperature calibration.	33
3.3	Comparison of experimental c_p of sapphire (1 mm thickness disk) and theoretical values at $\beta = 40 \text{ K} \cdot \text{min}^{-1}$. It can be observed that the experiment matches well the theoretical values in the range 300 to 1000 °C	34
3.4	DSC curves of both sapphire samples (0,5 mm and 1 mm).	34
3.5	Preliminary tests at $20 \text{ K} \cdot \text{min}^{-1}$. In red: theoretical c_p of POCO graphite (reference). In green and blue: tests of preform with the original microstructure. In purple: test of preform powder. The higher the mass, the smoother the curve.	35
3.6	Temperature profile used by the Sapphire technique	37
3.7	Comparison of experimental results of c_p for graphite and the reference from NETZSCH. Discrepancies are shown in dotted circle.	39
3.8	Curve fitting (green) for the experimental values of c_p of graphite (blue).	39
3.9	Comparison of experimental results of c_p for preform and the reference graphite from NETZSCH. Lower values of c_p have been obtained for preform.	40
3.10	Curve fitting (green) for the experimental values of c_p of preform (blue).	40
3.11	Apparent c_p of resin when chemical reactions are occurring.	41
3.12	Crucible with resin before (left) and after (right) the experiment.	42
3.13	Comparison of experimental results of c_p for the resin char and the graphite reference from NETZSCH.	42
3.14	Polynomial fit for resin char. Good agreement was found with the experimental data.	43
3.15	Comparison of experimental results of c_p for Asterm char and the graphite reference from NETZSCH. The values obtained are smaller than the previous cases. Axis omitted for confidentiality.	43
4.1	Workflow diagram for FiTGA.	45
4.2	Curve reconstruction for PATO.	45
4.3	Flowchart for the algorithm nonlinLSQ used in <i>FiTGA</i> to retrieve the kinetic parameters.	46
4.4	Flowchart for the Genetic Algorithm implemented in <i>FiTGA</i> .	46
4.5	Contribution of each variable to the main effects. The higher the slope, the more important a parameter is.	48
4.6	Pareto chart with first order interactions. It can be pointed out that the bars that do not reach the value of the vertical blue line (A , An) are not significant from the statistical point of view.	49
4.7	Results obtained with the EET test	50
4.8	VBSA results: left – main effects; right – total effects. It can be pointed out that the effect of the variables n and A is very small compared to the effect of the other two variables (F and E) in both main and total effects.	52
4.9	Convergence curves for VBSA algorithm. It can be observed that when increasing the number of evaluations of the model, the parameters tend to a value.	52
4.10	Results obtained with the FAST algorithm	53
4.11	Probability distribution plot of density loss over temperature.	54

4.12 PDFs obtained for different temperatures. It can be seen that at low temperatures, $T = 400\text{ K}$, no reaction has started yet (the pdf is equal to 1 for $\rho/\rho_v = 1$), as the temperature increases, the pdf evolves to lower values of density ratios until $T = 1400\text{ K}$ where almost all the reactions have already finished	54
4.13 Fitting process results (red) for 2 Reaction with simulated data (blue). Great agreement is found.	55
4.14 TGA and DTGA curves with different contributions. An overlapping area can be seen in the dashed circle.	56
4.15 HGA results with two different heating rates. The two curves are perfectly fitted.	57
4.16 Comparison of density ratio evolution: In blue the experimental points, in red the adjusted curve.	58
4.17 Decomposition of the reaction process. In red the totals (dashed line: TGA, solid line DTGA) and in the other colors the different contributions to the total DTGA.	58
A.1 Overview of <i>OpenFOAM</i> structure [57]	71
A.2 Typical structure of folders of a <i>OpenFoam</i> case	71
A.3 Main structure of folders and files of a PAM tutorial.	73

List of Tables

1.1	Parameters and materials used in previous missions [3]	2
2.1	Comparison of different methodologies for c_p determination	11
2.2	Selected kinetic models [27]. The variable n is the so-called order of the reaction	17
2.3	Comparison of the different algorithms presented in this section. The HGA presents the pros of the two other algorithms and with only a small increase in calculation time compared with a normal GA.	26
3.1	Temperature correction obtained with a quadratic fit	33
3.2	Preliminary tests with preform at $20\text{ K} \cdot \text{min}^{-1}$	35
3.3	Relation between heating rate and mass. The selected combination is shown in bold.	36
3.4	Breakdown of time spent by each measurement	37
3.5	Test matrix with the different experiments performed for c_p determination ($\beta = 40\text{ K} \cdot \text{min}^{-1}$). The subscript bis means repetition with the same material.	38
4.1	Aleatory numbers for the two reactions	55
4.2	Comparison between fitted and simulated parameters. The maximum difference found is 1.29% for the variable A of the second reaction.	56
4.3	Comparison between input and output data for the case of two different heating rates. The difference obtained for the variable A is approximately 30 %	57
4.4	Arrhenius parameters and peak temperatures for the different reactions obtained with FiTGA.	59
4.5	Arrhenius parameters and peak temperatures obtained by Lachaud [43].	59
6.1	Personal costs of the project	62
6.2	STA Measurements Costs	62

1 Introduction

The Space Race started on the 4th of October 1957 with the USSR launching the first artificial satellite, the Sputnik 1. This event can be considered as an inflection point in history, which changed the perspective of humanity; science and technology can take us further (and faster) than we could have ever imagined. After this, many projects¹ have successfully been carried out: returning manned missions to the Moon (Apollo program, 1960s), having people living for months in space (International Space Station, 2000s), sending unmanned vehicles to other planets for orbiting (Mars Express, 2003 or the Voyager Program, 1970s) and landing (Mars Science Laboratory, 2011), collecting and returning samples from asteroids (Hayabusa 1, 2003 and Hayabusa 2, 2014) or comet dust (Stardust, 1999). It can be noted that the complexity of the missions has increased throughout the years. Future steps include manned missions to Mars, unmanned exploration of other planets and sample return from them.

New developments are required for these incredibly challenging projects. One critical step of the mission is the atmospheric entry. When a spacecraft performs atmospheric entry from space at high velocities (hypersonic flows), a detached shock wave is generated around the blunt body. This shock wave increases the temperature of the flow to temperatures exceeding 10 000 K depending on the speed. The proper design of thermal protection systems (TPS) is essential to accomplish the mission successfully.

There are two main types of TPS: the reusable heat shields (used in the space shuttle, ceramic materials and composites with a high melting point temperature but high density which dissipate heat in terms of radiation) and the ablative group [1]. An ablative material decomposes absorbing heat (endothermic reaction), this process results in a loss of mass and recession of the material surface during the entry. The decomposition process can be divided into two mechanisms: pyrolysis and ablation. The pyrolysis is the mechanism by which the resin gets degraded and carbonized; and the ablation is a group of processes that induces the removal of material from the surface.

The very early idea of using ablative materials for atmospheric reentry came from Robert H. Goddard in 1920, who explained that a way to protect a spacecraft during an entry process would be to apply the same concept as meteors: “layers of a very infusible hard substance with layers of a poor heat conductor between”. Based on this idea, the Apollo capsule returned to Earth from the Moon back in 1969 using an ablative TPS composed by a resin impregnated in a fiberglass honeycomb matrix.

¹The cited programs are just some examples among many other projects performed by different space agencies (or collaborations).

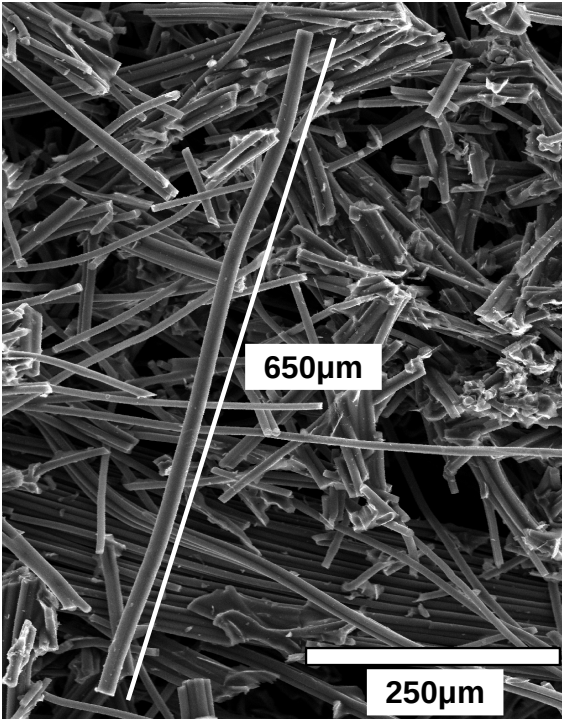
New advances in material sciences have led to a new type of ablative material composed of carbon fibers impregnated with phenolic resin. This material is known as Lightweight Ceramic Ablator (LCA). Some examples of LCA include PICA, developed by NASA and its European counterpart Asterm, developed by Airbus. Despite having a low density, around 80 to 90 % porosity, LCA are able to absorb a large amount of heat due to the endothermic chemical reactions of pyrolysis. The low density, about a half compared with AvCoat (Table 1.1), and the high heat absorption make LCAs recommendable over the older derivatives of ablative TPS used during the Apollo Era [2] in many cases.

Table 1.1: Parameters and materials used in previous missions [3]

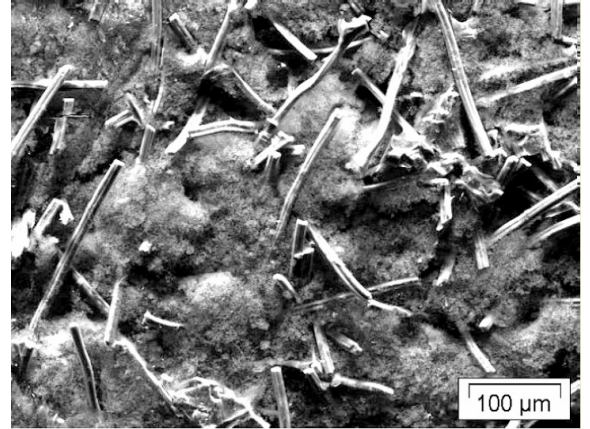
Mission	Re-entry Year	Planet	Material	Density [kg · m ⁻³]	Velocity [km · s ⁻¹]	Heat Load [MJ · m ⁻²]
Apollo 4	1967	Earth	Avcoat	530	11.14	300
Galileo	1995	Jupiter	TWCP	1450	47.4	2000
Pathfinder	1997	Mars	SLA	260	7.26	-
Huygens	2006	Titan	Prosial	540	6.1	-
Stardust	2006	Earth	PICA	250	12.8	360
Hayabusa	2010	Earth	TWCP	1450	11.3	212

In this type of material, two parts can be clearly observed:

- ***Carbon-bonded carbon fiber preform (CBCF)***: short carbon fibers randomly oriented with a density ranging between 180–210 kg · m⁻³ and a porosity higher than 80 %. In Figure 1.1a, one can observe the randomly oriented fibers with a scanning electron microscopy (SEM) micrograph. This preform is a short fiber insulation originating from rayon, the fibers of which are interconnected in a matrix produced by the fully carbonization of phenol-formaldehyde resin. The material is cured at high temperatures (~2000 °C) to ensure stability and evacuation of trapped gases [4].
- ***Resin***: The preform is impregnated with a specific type of phenolic resin (Figure 1.1b). A particular curing process and polymerization is needed to achieve the desired characteristics, but this information is not available publicly.



(a) Micrograph of preform using SEM [4].



(b) Micrograph of LCA [5]. The fibers surrounded by the phenolic resin can be observed.

Figure 1.1: Micrographs of LCAs.

Nevertheless, the tools available nowadays for design and analysis have marginally evolved since the Apollo Era and are not accurate enough to predict with precision the behavior of these materials.

An example that shows the inaccuracies of the available design tools is the Galileo Probe, which entered the atmosphere of Jupiter back in 1995. As it can be observed in Figure 1.2, it was thought that the heat shield was going to suffer a much higher recession at the stagnation point than at the edges. However, the predictions did not come true and the recession at the stagnation point was not as high as expected. It can be clearly seen that the thickness was overestimated near the nose, and it barely could stand the entry process near the edges. This fact shows that further research is needed since a failure in the TPS will suppose a failure in the whole mission. In other words, the heat shield is a mission killer. In addition, the TPS is an important contributor to the total mass of the spacecraft (for example, up to 50 % in the Galileo probe), thus optimizing its mass is a high-priority task since it will allow to increase the payload. This is also important in terms of budget, due to the high cost of sending a kg to orbit.

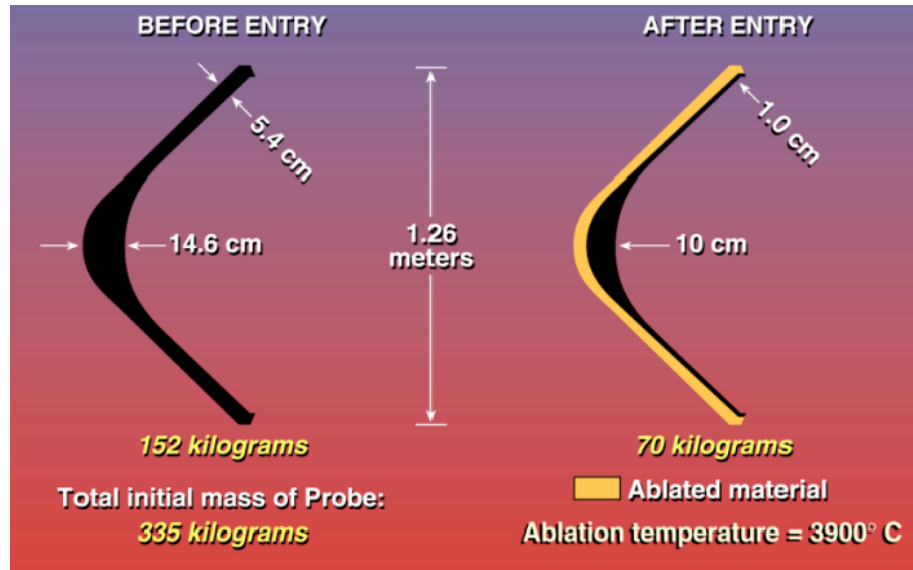


Figure 1.2: Galileo Probe Heatshield [6]. Thickness distribution before and after reentry on Jupiter: almost all material ablated at the shoulder but stagnation point region was overestimated.

Even though some characterization has been carried out on LCAs, there is not much data available in the literature since many of the documentation is classified. The community accepts the model proposed by Trick and Saliba [7] back in the 1990s and reformulated by Bessire et al. with more recent findings [8] (Figure 1.3). When this material gets pyrolysed, different stages can be observed from the chemical point of view depending on the major gas-phase product generated:

- **Stage 0:** During this stage, the sample is heated from ambient temperature to 400 °C. Trapped gases during the curing process and absorbed water are released (no chemical processes associated).
- **Stage 1:** This stage ranges from 200 °C to 550 °C. It is characterised by the depolymerization of the resin, producing phenol and its methyl substituted derivatives. In addition, H₂O is released due to the reaction of hydroxyl or methylol functional groups.
- **Stage 2:** During this stage (T ≈ 400 °C–800 °C) links are broken leading to the formation of H₂, CO and CH₄ (for example, C₆H₆ + H₂ ⇌ C₆H₆ + H₂O).
- **Stage 3:** In this last stage (T ≈ 560 °C–1000 °C) the aromatic rings fuse to form the residual char, releasing H₂ (dehydrogenation).

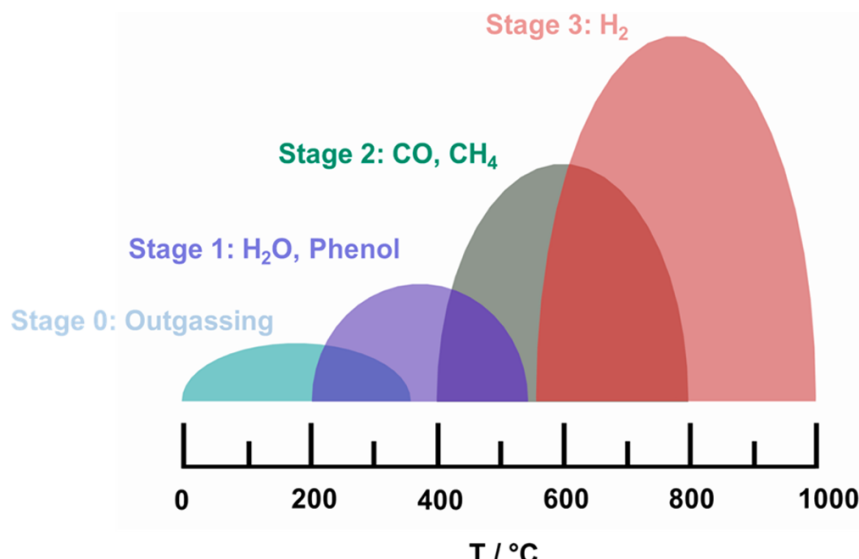


Figure 1.3: Different stages of pyrolysis as function of their temperature ranges [8].

Due to the chemistry mentioned above, the material undergoes several transformations from the macroscopic point of view. They can be divided into different zones considering the predominant mechanism as depicted in Figure 1.4.

- Virgin material zone: in this zone no pyrolysis reactions have occurred, some decomposition (release of trapped water) can be observed but can be considered negligible.
- Pyrolysis zone: the phenolic polymer is decomposed and pyrolysed releasing gases and becoming a char according to Figure 1.3.
- Coking zone: this zone is predominantly pyrolysed. Some compounds can be formed ($C_6H_6 \rightleftharpoons C_6 + 3 H_2$).
- Ablation zone: in this part, the charred material, composed of carbon fibers and charred fibers, is removed by ablation. There are several processes that promote ablation: oxidation (forming CO), nitridation (generating CN), phase changes (sublimation of carbon) and mechanical erosion.

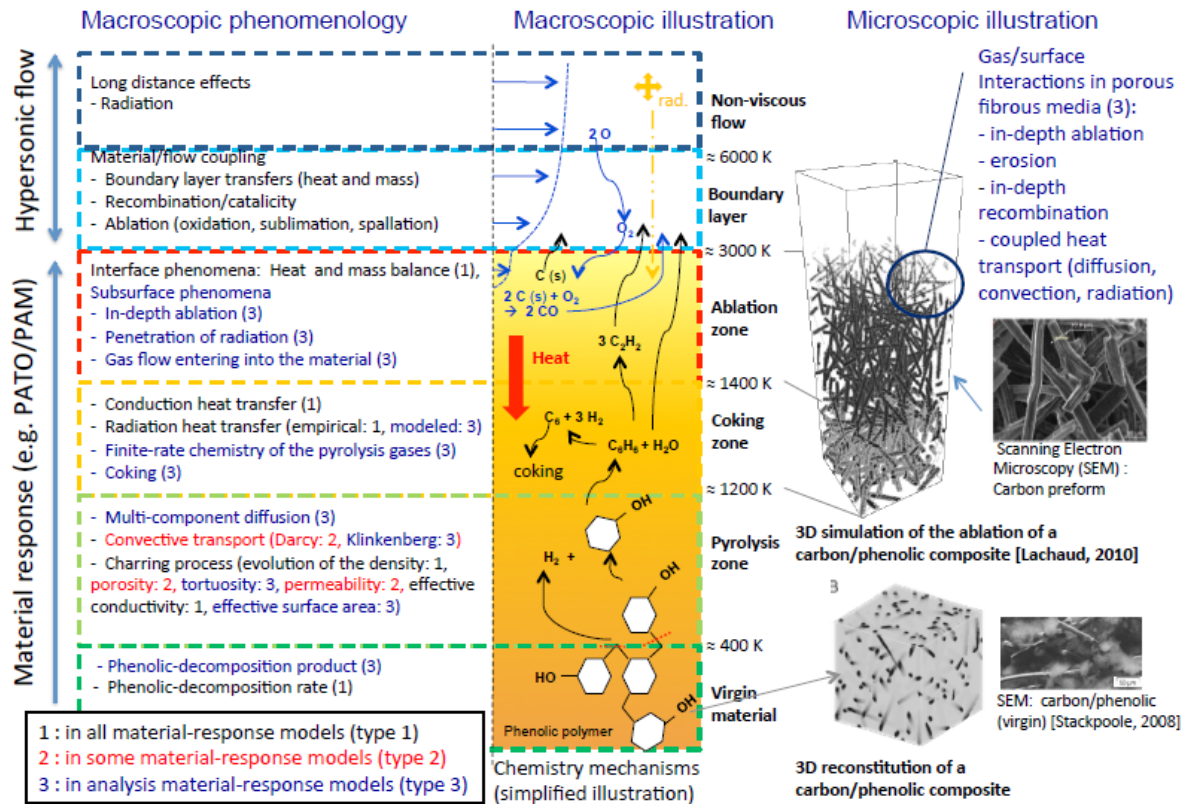


Figure 1.4: Phenomenology of porous ablator material response [9]

In other studies, Wong et al. focused on the identification and quantification of the different species generated during the pyrolysis processes using spectroscopy and chromatography techniques [10, 11]. Moreover, Torre et al. did several thermal analysis experiments obtaining satisfactory results about the reaction mechanisms involved in the pyrolysis of a material made of silicone resin filled with phenolic spheres, quartz spheres and fibers [12–14]. In addition, G. Pinaud et al. [15] developed a thermo-chemical and mechanical coupled analysis for TPS materials which gave good results in terms of tendencies despite the assumed simplifications.

Several tests involving spectrometry, mass loss and recession measurements have been done at the VKI Plasmatron facility in order to characterize the response of low density carbon-phenolic ablators [4, 5, 16]. The VKI Plasmatron is the most powerful induction coupled plasma wind tunnel in the world. This unique facility of 1,2 MW is capable of ionizing the gas (N_2 O_2 , Ar, CO_2) generating a pure plasma flow at temperatures up to 10 000 K, allowing to replicate the high-enthalpy flow that is produced during a re-entry process[5].

Therefore, it can be clearly seen that even though a huge amount of scientific effort has already been carried out, there are still some processes that need a deeper understanding such as a detailed characterization of the pyrolysis processes occurring in LCA.

The main objective of this project is to obtain reliable experimental data on thermal decomposition through pyrolysis of LCAs. In order to do so, Thermogravimetric Analysis (TGA)

and Differential Scanning Calorimetry (DSC) techniques have been used. These techniques consist of measuring a series of parameters (mass loss and heat flux respectively) against an imposed temperature program. These methodologies are extensively used in polymer research. Some applications include determination of the heat capacity [17], characterization of the different reactions undergone by the material [18] or thermal degradation [19].

The structure of the thesis is as follows:

Chapter 2 - Materials and Methods. In this chapter, the different materials are presented showing their different characteristics. The thermal analysis techniques and the thermal analyzer available at the VKI are explained in detail.

Chapter 3 - Experimental methodology for heat capacity determination by DSC. This chapter presents the methodology followed to perform DSC measurements for heat capacity determination. The calibration procedure and results are also shown in this section.

Chapter 4 - TGA Curve Fitting. The FiTGA package, which has been specifically developed to analyze TGA experimental data, is described in this Chapter. A statistical analysis to show the relative influence of the variables in the equation of the kinetic model using Sobol' Indices (technique based on ANOVA and Monte Carlo methods) is described too. Finally, some examples for verification of the package as well as a test with experimental data are presented.

Chapter 5 - Conclusions. First, specific conclusions for DSC and TGA results are presented, and after, some final conclusions are highlighted.

Chapter 6 - Budget. A review of the costs of this project is described.

2 Materials and Methods

2.1 Materials

In this work, we have tested different LCA materials used as TPS in space missions in order to characterize their thermal response. Firstly, graphite is used as reference material for comparisons because a part of LCAs are carbon based materials (carbon fibers and char produced by the pyrolysis of the resin). Secondly, the two components of a LCA: carbon fibers and resin; and an example of a complete LCA material: Asterm were analyzed.

Graphite was obtained from a sample used in the VKI Plasmatron to perform ablation experiments. The samples were cut directly from the sample in form of thin layers of a few mm and mass $m \approx 10 - 20\text{mg}$ per piece. After, they were heated in the oven at 500 K during 2 h to eliminate possible impurities or trapped gases.

The carbon fibers were provided by Mersen Scotland Holytown Ltd. (CALCARB CBCF 18-2000). They were machined in-house for the VKI plasmatron (Figure 2.1a). The samples used in TGA/DSC experiments were obtained from one of those samples used in Plasmatron experiments. An annulus of $\sim 5\text{ mm}$ thickness was cut from the bottom part of one sample. This annulus was cut in small cubes with a mass $m \approx 2 - 5\text{mg}$. It was also heated in the oven with the same conditions of graphite. Part of these samples were crushed to create a powder of preform. They were inserted in the glovebox (where the TGA/DSC device is located) in an open container to ensure that possible trapped molecules ($\text{O}_2, \text{N}_2, \text{H}_2\text{O}$) will be diffused in the Argon atmosphere of the glovebox.

The resin was provided by Durez Corporation and it was cured at 450 K for 30 min [11]. The final form of the material when received is shown in Figure 2.1b. Afterwards, it was crushed and powdered. It was also inserted in the glovebox in an open container.

Asterm is a LCA manufactured by Airbus DS. The final density of the composite material has a range between $240 - 550\text{ kg} \cdot \text{m}^{-3}$. The techniques used to cure and manufacture the materials are not available since it is classified material. The samples for the TGA/DSC measurements were obtained from a sample for the VKI plasmatron (Figure 2.1c). The material was crushed and put into the glovebox in an open container with water absorbing polymer spheres.



(a) Machined preform prepared to be tested in the VKI plasmatron [4]



(b) Phenolic resin as it was received.



(c) Machined Asterm sample prepared to be tested in the VKI plasmatron [5]

Figure 2.1: Materials of analysis

2.2 Thermal Analysis Techniques

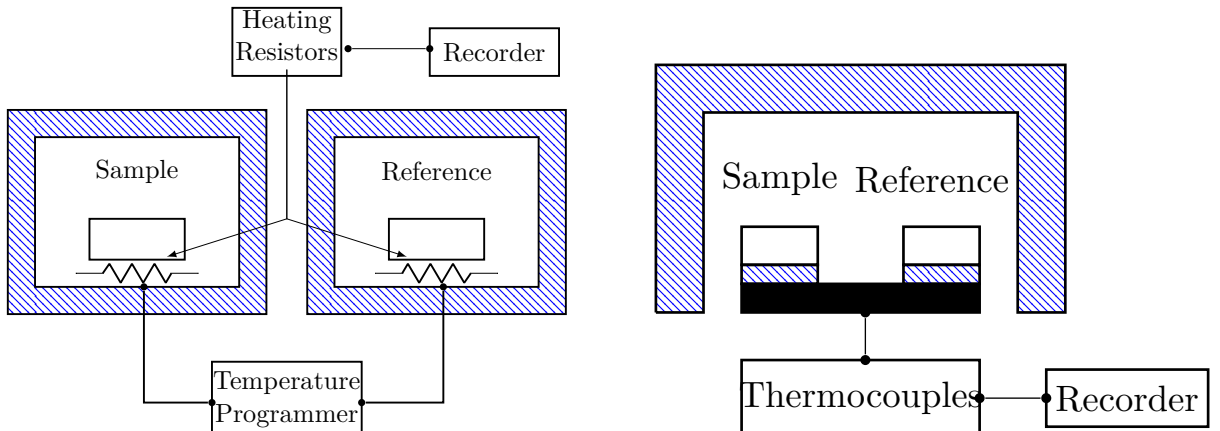
2.2.1 Differential Scanning Calorimetry

Differential Scanning Calorimetry (DSC) is a technique in which the heat flux provided to a sample is monitored against time or temperature [20]. Normally, the evolution of the temperature with respect to time is pre-programmed, allowing different linear or constant sections (depending on the type of study).

There are two main types of DSC instruments depending on the location of the samples: a power-compensating DSC and a heat-flux DSC.

In the power-compensating DSC (Figure 2.2a), there are two different furnaces, one is for the reference and the other is for the sample. Both furnaces are maintained at the same pre-programmed temperature using a control loop in order to ensure that the temperature is increased at the same rate. Another control loop adjusts the power input as soon as a temperature difference starts to appear (due to endothermic or exothermic reactions in the sample). The differential power signal is recorded as a function of the temperature of the sample. This difference will provide the heat flux.

In the heat-flux DSC (Figure 2.2b), both the sample and the reference are located in the same furnace, in different crucibles. Small temperature differences are recorded using thermocouples (one in the reference zone and another in the sample zone). From these temperature differences, the heat flow that should be provided or absorbed can be calculated [21]. This is the type of analyzer available at the VKI.



(a) Power-compensating DSC. Adapted from “Thermal Analysis of Polymeric Materials” [22]

(b) Heat flux DSC. Adapted from “Thermal Characterization of Polymeric Materials” [23]

Figure 2.2: Schemes of the two main types of DSC analyzers. It can be noted that the main differences are the location of the samples and the way used to calculate the heat.

The DSC technique is extensively used in material research, specifically in polymer investigation since it allows the computation of different transition points (such as glass-rubber temperature; crystallization, melting, recrystallization temperatures and heat; cure measurements, etc). In the studied case, the main interest is to calculate the heat capacity and the heat that the sample absorbs (due to endothermic reactions) when it is pyrolysed. A detailed description of the procedure is described in the following section.

2.2.1.1 Specific heat capacity determination procedure (ISO 11357)

There are different procedures to estimate the specific heat capacity (c_p) of a substance using DSC. The c_p is defined as the energy needed to increase the temperature of a unit mass by 1 K (Equation 2.1).

$$c_p = \left(\frac{\partial h}{\partial T} \right)_p \quad (2.1)$$

If the mass is assumed to be constant and the heat losses can be neglected, Equation 2.1 can be expressed in terms of the quantities obtained in the DSC analysis as:

$$c_p = \frac{1}{m} \frac{\dot{Q}}{\beta} \quad (2.2)$$

where β is the heating rate.

The different methodologies involve increasing the temperature and use the Equation 2.2. The main differences between the different methods are summarized in Table 2.1.

Table 2.1: Comparison of different methodologies for c_p determination

	Direct	Steady State	Sapphire	Modulated DSC
Principle	Directly from 2.2	Directly from 2.2	Comparing with a reference	Comparing with a reference
Temp. Increase	Linear	sawtooth	Linear	Sinusoidal
Advantages	Shortest time easy to implement	quasi isothermal c_p	High accuracy	c_p also during non-reversing reactions
Disadvantages	not very accurate	not very accurate, long measurement time	three measurements required	three measurements required

Although all these methods are commonly used for c_p determination, in this work the sapphire method has been chosen, since it is the only one that has been standardized.

The sapphire method can be summarised as follows:

- Calibration and adjustment of the DSC device: this temperature calibration is done at the beginning of every experimental campaign. It consists of running tests for different materials (usually metals) the melting point of which is well known. These metals are usually run twice to ensure repeatability.
- Blank measurement: this measurement is performed with the two empty crucibles. It is used as a baseline to take into account the heat absorbed by the crucible and the buoyancy effect. It will be subtracted from the other measurements to actually measure the heat absorbed by the sample (or the standard) with a higher precision.
- Reference measurement: a sapphire standard disk is used (in our case 0,5 mm thickness disk). This measurement will provide the heat absorbed by the sapphire standard whose c_p is well known.
- Sample measurement: the actual material of interest.

It should be noted that the blank and the reference runs can be used for several measurements if the instrument is sufficiently stable. It is recommended to run them at least twice to ensure that they are stable and reproducible.

When the sapphire method is applied, Equation 2.2 cannot be used (directly). Since the heat absorbed by the crucibles is obtained during the blank run and considering that heat is linear (i.e. $Q_{\text{total}} = Q_{\text{sample}} + Q_{\text{crucible}}$) it can be written:

$$m^{\text{sample}} \cdot c_p^{\text{sample}} \propto \dot{Q}_{\text{sample}} - \dot{Q}_{\text{base}} \quad (2.3)$$

Considering Equation 2.3 for both the sample and the reference material (sapphire) and manipulating:

$$c_p^{\text{sample}} = c_p^{\text{sapphire}} \frac{m^{\text{sapphire}} (\dot{Q}^{\text{sample}} - \dot{Q}^{\text{base}})}{m^{\text{sample}} (\dot{Q}^{\text{sapphire}} - \dot{Q}^{\text{base}})} \quad (2.4)$$

Equation 2.3 gives the c_p as function of the input heat flux. Nevertheless, the thermal analyzer registers the voltage difference, therefore Equation 2.3 can be rewritten in terms of voltages as:

$$c_p^{\text{sample}} = \frac{m^{\text{sapphire}}}{m^{\text{sample}}} \frac{(V^{\text{sample}} - V^{\text{blank}})}{(V^{\text{sapphire}} - V^{\text{blank}})} c_p^{\text{sapphire, theoretical}} \quad (2.5)$$

where c_p^{sapphire} is the theoretical c_p of sapphire.

Using this methodology, we are correcting the c_p with the reference material obtaining more accurate results. The post-processing has been done with the software provided by the manufacturer of the TGA/DSC apparatus *NETZSCH Proteus v6.1*.

Another important fact is that the c_p can be only accessed easily during the sections in which the material does not undergo any transformation (such as crystallisation, rubber transition, pyrolysis, etc). In those regions where the c_p is not accessible, the heat absorbed or released can be calculated as the area under the curve considering that the c_p evolves linearly in that part (Figure 2.3 explains better the previous statement). To actually determine the c_p in those sections, Modulated DSC should be used.

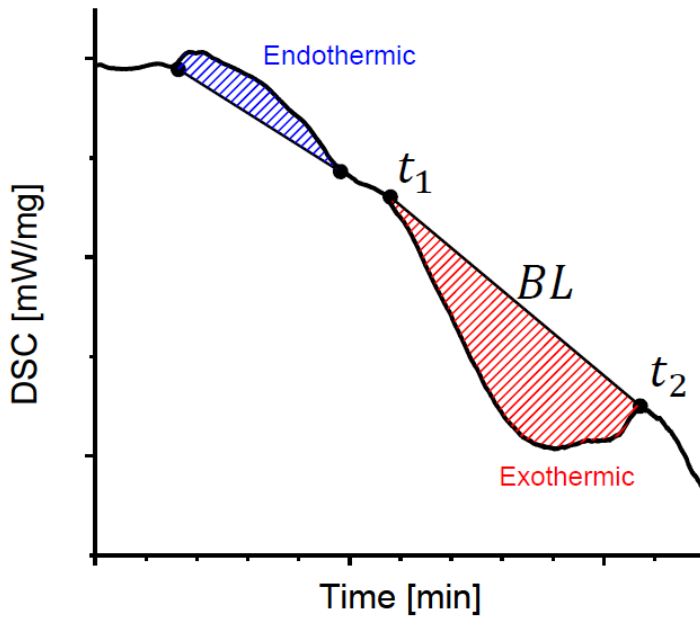


Figure 2.3: DSC curve; striped areas correspond to different reactions

Even though the thermal analyzer available at the VKI is not capable of performing MDSC, a word of explanation should be done to this technique that has been growing in popularity over the last years since it allows to separate the reversing and non-reversing components of the DSC measurement. In this methodology, the temperature is increased with the sum of a linear increase and a sinusoid curve as shown in the following equation:

$$\frac{dT}{dt} = \beta + A\omega \cos(\omega t) \quad (2.6)$$

where:

- $\frac{dT}{dt}$: instantaneous heating rate ($^{\circ}\text{C} \cdot \text{min}^{-1}$)
- β : heating rate ($^{\circ}\text{C} \cdot \text{min}^{-1}$)
- A : Amplitude of the sinusoid signal ($^{\circ}\text{C}$)
- ω : angular frequency ($2\pi/T$)
- T : Period of the sinusoid signal (min)

Figure 2.4 shows the decomposition of the different temperature signals of MDSC: the dashed line is the linear increase, the dot-dashed line represents the derivative of the sinusoid curve, and the solid line is the resulting sum. This can be very useful when chemical reactions occur. However, this technique requires some expertise in the field since the modulation adds two new variables to be tuned in the experiments: the amplitude and the frequency of the modulations.

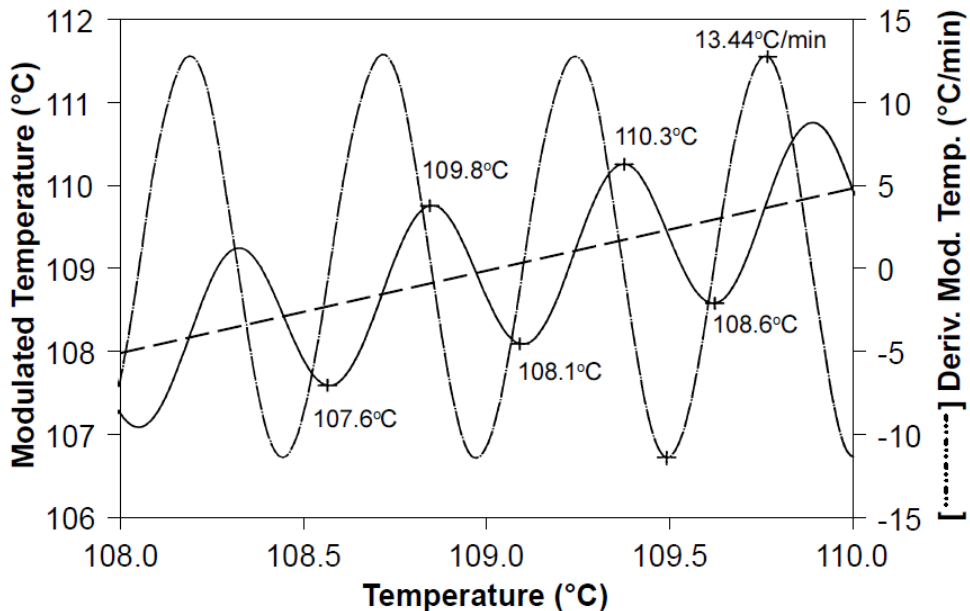


Figure 2.4: MDSC temperature increase scheme. The solid line is the actual temperature program. The dashed line is the linear increase ($\beta = 1^{\circ}\text{C} \cdot \text{min}^{-1}$) and the dot-dashed line is the derivative of the sinusoid curve ($T = 30\text{s}$, $A = 1^{\circ}\text{C}$) [24].

2.2.2 Thermogravimetric Analysis

Thermogravimetric Analysis (TGA) is a technique in which the mass of a sample is monitored against time and temperature [21] (Figure 2.5). Usually, the temperature is pre-programmed and controlled during the whole process. A common practice consists of increasing the temperature at a constant rate (i.e. $10\text{K} \cdot \text{s}^{-1}$). In addition, different heating rates are usually studied because the kinetics can vary, thus resulting in the production of different compounds.

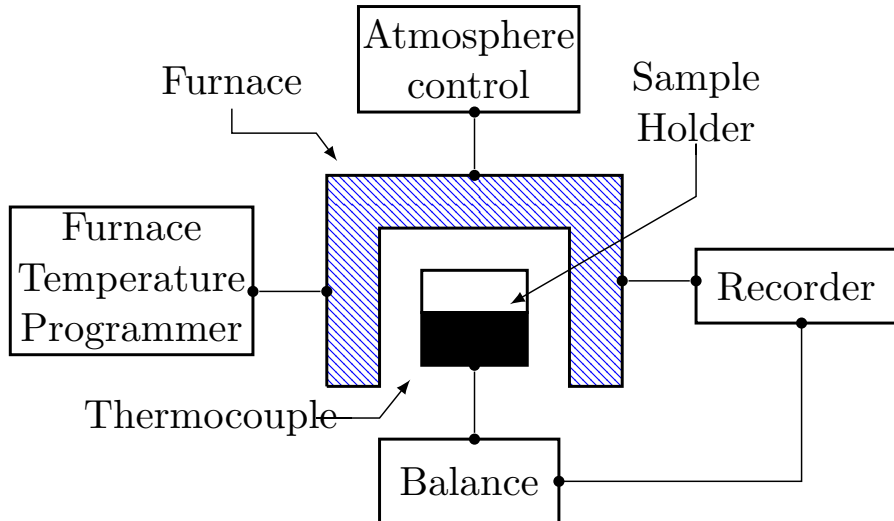


Figure 2.5: Schematic of a TGA analyzer. Adapted from “Thermal Characterization of Polymeric Materials” [23]

The increase of temperature of the sample produces a series of physical and chemical reactions that will generally result in a mass loss due to the removal of the volatile compounds. The balance is purged using a constant flow rate of a specific gas (usually oxygen, nitrogen or argon) which depends on the type of study. For example, oxygen (or air) is used in cases where it is interesting to simulate real conditions allowing oxidation. Argon is used when only the reactions that occur in the sample are analysed since it is a non-reacting gas.

The density (or mass) loss can be plotted against temperature (blue line in Figure 2.6). This type of plot is called a *thermogram* and gives an idea of the different processes that the sample has undergone. In Figure 2.6, the two steps can be interpreted as two pyrolysis reactions. 25 % of the total density is lost in the first reaction, and 50 % on the second. In addition, the derivative of the density loss curve (DTGA) can be also plotted (red line). In this curve, the maxima are the inflection points of the TGA curve, and they usually correspond to a reaction.

The sample size is an important parameter in TGA because during the heating process, homogeneity of temperature in the sample needs to be ensured. Furthermore, the sample has to be representative of the material being studied. Therefore, the following criterion is usually followed: the bigger the sample, the slower the heating rate.

A thermocouple located at the base of the sample holder and a high precision balance are used to measure the parameters of interest. High precision and accuracy has to be achieved by these two instruments in order to be able to perform a proper TGA.

When running TGA experiments, the buoyancy effect due to Archimedes' principle should be taken into account. This effect will generate an apparent increase of mass in the TGA curves. To correct this undesirable effect, a baseline with empty crucibles is run before the actual experiment. This baseline will be subtracted from the actual experiment, hence compensating

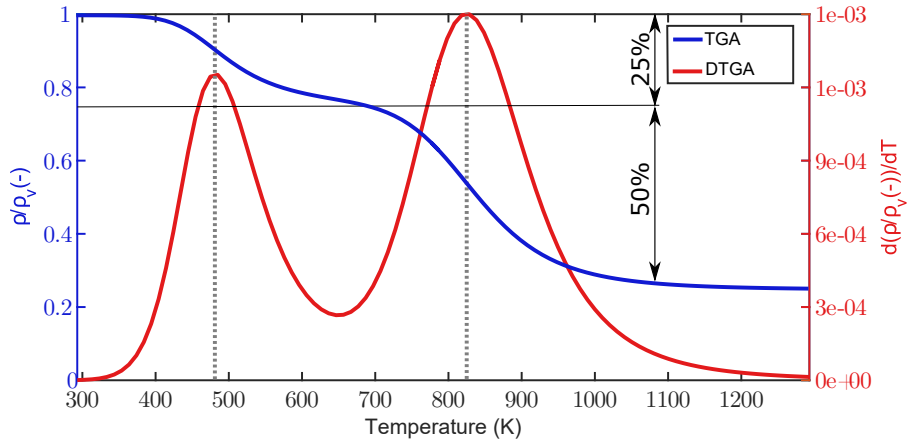


Figure 2.6: Example of thermogram depicting the mass loss during two different reactions of the pyrolysis process (arbitrary data). The left axis represents the TGA in terms of density ratio. The right axis is the DTGA; each peak indicates a reaction.

the buoyancy effect [25].

2.2.2.1 Kinetic Analysis of the Thermal Degradation Process

The kinetic analysis consists of obtaining the different laws related with each reaction produced as a function of the concentrations (of reactants and products) and temperature.

First of all, the difference between homogeneous and heterogeneous reactions should be clarified. For a reaction to be homogeneous, the reactants should be miscible at the molecular level and be present in the form of a single phase. In that case, the reaction will take place in the whole volume and the reaction rate will be proportional to the concentration of the reactants [26]. For example, gases usually react in homogeneous reactions. On the other hand, when the reactants are not miscible in the molecular level, the reactions can only take place at the interface of the reactants, therefore the reaction rate is not related to the concentration of the components, but rather with the area of the interface; in this case, the reaction is heterogeneous. Processes that include a reacting solid phase are usually considered to be heterogeneous.

To study heterogeneous reactions, the Arrhenius law is the commonly accepted model:

$$k(T) = A \exp\left(\frac{-E}{RT}\right) \quad (2.7)$$

$k(T)$ is defined as the rate constant and it expresses how and when the degradation is produced, E is the activation energy, A is a pre-exponential factor, R is the gas constant and T is the temperature, which in material research is kept as a constant or as linear function of time.

Another variable can be defined in order to consider the state of the decomposition at a given time t . This variable, usually called degree of conversion or advancement of reaction χ , is defined in Equation 2.8. This variable indicates in how the reaction advances, in other words, it

evolves as a function of time. When $\chi = 0$ the reaction has not started, and when $\chi = 1$ the reaction has finished (Figure 2.7).

$$\chi(t) = \frac{m_0 - m(t)}{m_0 - m_\infty} \quad (2.8)$$

Where:

- m_0 : initial mass.
- m_∞ : final mass.

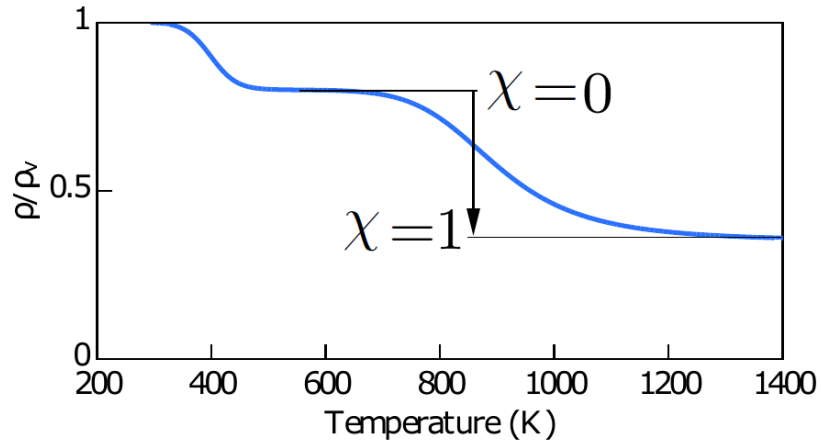


Figure 2.7: Advancement of the reaction. When $\chi = 0$ the reaction has not started, and when $\chi = 1$ the reaction has finished

If the volume of the sample is assumed to be constant, which can be considered in some studies, this equation can be expressed in terms of density.

$$\chi(t) = \frac{\rho_0 - \rho(t)}{\rho_0 - \rho_\infty} \quad (2.9)$$

Therefore, the degradation equation can be expressed as follows:

$$\frac{d\chi}{dt} = f(\chi)k(T) = f(\chi)A \exp\left(\frac{-E}{RT}\right) \quad (2.10)$$

where the function $f(\chi)$ depends on the mechanism of degradation. Different mechanisms can be considered depending on the reactions that are present in each particular case [21] (Table 2.2 displays a small review of commonly used models). The microstructure, the density and other material properties also affect the decomposition mechanisms. Determining the reaction mechanism is usually very complicated, especially when there are different reactions occurring at the same time and they overlap in time and space.

Table 2.2: Selected kinetic models [27]. The variable n is the so-called order of the reaction

Kinetic model	Function $f(\chi)$
Nucleation and Grow	$f(\chi) = 1/n(1 - \chi)(-\ln(1 - \chi))$
Phase boundary reaction	$f(\chi) = n(1 - \chi)^{(n-1)/n}$
Diffusion	$f(\chi) = 1/\chi$
Power Law	$f(\chi) = (1/n)\chi^{1-n}$
Chemical Reaction	$f(\chi) = (1 - \chi)^n$

These models can be grouped into three main types of heterogeneous reactions: accelerating, decelerating and sigmoid (or auto-catalytic). To determine if one reaction corresponds to one of these groups, the most common practice is to perform isothermal experiments. In a isothermal run, Equation 2.10 becomes:

$$\frac{d\chi}{dt} = C f(\chi) \quad (2.11)$$

It can be clearly seen that the reaction rate is only a function of the model $f(\chi)$, thus the type of reaction can be determined based on the shape of the curve (Figure 2.8).

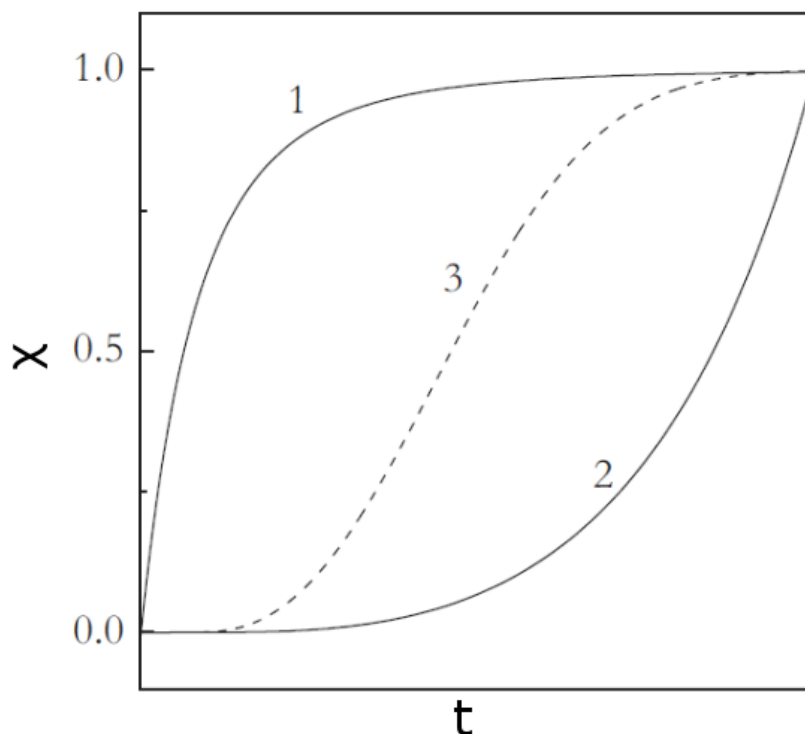


Figure 2.8: Schematic of reaction types following model $f(\chi)$: . 1 - Decelerating; 2 - Accelerating; 3 - Sigmoid [26]

Note that if the reaction is studied in a non-isothermal run, the reaction type cannot be determined easily since there is the effect of the rate constant $k(T)$.

The kinetic parameters cannot be directly obtained from the experiments. The experimental data have to be processed in such a way that the parameters are retrieved. There are two main

families of methods: model fitting and model free (often also called isoconversional) which will be described in more detail in the following sections.

Isoconversional Methods The isoconversional principle states that the process rate at constant advancement of reaction χ is only a function of temperature. This can be shown taking the logarithmic derivative of Equation 2.10 at constant χ :

$$\left[\frac{\partial \ln d\chi/dt}{\partial T^{-1}} \right]_{\chi} = \left[\frac{k(T)}{\partial T^{-1}} \right]_{\chi} + \left[\frac{f(\chi)}{\partial T^{-1}} \right]_{\chi} \quad (2.12)$$

It can be observed that if $\chi = \text{constant}$ the second term of the right hand side (RHS) of the equation will be 0. The first term of the RHS can be obtained deriving Equation 2.7. And combining it with Equation 2.12, one gets:

$$\left[\frac{\partial \ln d\chi/dt}{\partial T^{-1}} \right]_{\chi} = -\frac{E_{\chi}}{R} \quad (2.13)$$

Here it can be clearly seen that the isoconversional activation energy can be obtained at a given extent of conversion without assuming any model for $f(\chi)$. Even though this method seems a great solution for kinetic analysis, it gets very complicated to apply it in the case of a multi-step case since the different contributions cannot be easily extracted.

Model-fitting Methods This approach is especially convenient when the number of pyrolysis reactions and the model are known. There are different ways to apply it: integral, differential and optimization-based methods. The first two methods consist in determining some of the parameters (for example the triplet A, E, n) associated with a reaction applying some simplifications such as linearizing the model. The list of methods available is large and different authors use one or the other depending on the particular case. A good review of the different methods is presented in [21].

The optimization-based methods consist in using optimization (minimization) techniques to generate simulated data that is as close as possible to the experimental values. There are different techniques used for the minimization procedure such as genetic algorithms, trust region methods, line search, particle swarm, etc. This is the methodology applied in this dissertation using the two first approaches (genetic algorithms and trust region methods). They can be used separately or combined. It is important to highlight that although these methods are conceptually simple, they also have limitations:

- Difficulty to define the appropriate model.
- Different triplets may fit the data properly which leads to a non-uniqueness solution.
- If there are overlapping reactions, it may be difficult to deconvolute them.

Some of these limitations were revealed in the IATAC kinetics project-data [28–32] and the experts in the topic came to the conclusion that for using this method, different heating rates should be used.

In this dissertation, two different models to describe the pyrolysis process are used. One model is used in the *OpenFoam* library *Porous Material Analysis Toolbox based on OpenFoam (PATO)* [33]. This CFD library, which is currently under development, is used to study material response with a high-fidelity ablation model (a brief description of this package is provided in Appendix A.2) and the other one has been used in the computations performed by Airbus [15].

Kinetic model used in *PATO* This model (Equation 2.14) was proposed by J. Lachaud and N. Mansour [34] and it is used in the *PATO*. As can be observed, it has five unknowns per reaction. This is a very general and flexible model which allows the decomposition of the different components independently, thus making it more appropriate for materials with many different decomposing stages.

$$\frac{\partial \chi_i}{\partial t} = (1 - \chi_i)^{M_i} T^{N_i} A_i \exp\left(-\frac{E_i}{RT}\right) \quad i = 1, n_{Reactions}$$

$$\rho = \rho_v (1 - \sum_{i=1}^n F_i \chi_i)$$
(2.14)

Where:

- χ : advancement of the reaction.
- E_i : activation energy.
- A_i : pre-exponential factor.
- M_i : model parameter.
- N_i : Arrhenius parameter.
- F_i : maximum decomposition associated to the reaction.
- ρ_v : Density of the virgin material.

Kinetic model used by Airbus This model was originally developed by G. Pinaud et al. [15] and it has been used by Airbus. The formulation is very similar to the one proposed by Lachaud and Mansour. Nevertheless, this model has the limitation that only a part of the material can be pyrolyzed and it needs the density of the charred material (ρ_c) to calculate the decomposition.

$$\frac{\partial \chi_i}{\partial t} = A_i (\rho_v)^{1-n_i} (\rho_v - \rho_c)^{n_i-1} (1 - \chi_i)^{n_i} \exp\left(-\frac{E_i}{RT}\right) \quad i = 1, N_{Reactions}$$

$$\rho = \rho_v \left(1 - \sum_{j=1}^{N_j} F_i \chi_i\right)$$
(2.15)

Where:

- χ : advancement of the reaction.
- E_i : activation energy.
- A_i : pre-exponential factor.
- n_i : model parameter.
- F_i : maximum decomposition associated to the reaction.
- ρ_v : Density of the virgin material.
- ρ_c : Density of the charred material.

2.2.2.2 Numerical Methods

As commented in the previous section, the kinetic models are non-linear ordinary differential equations. Therefore, to extract the kinetic parameters that describe the process two steps are needed. On the one hand, we need to generate decomposition curves using a model, in other words, integrate the equation that describes the model. On the other hand, we need to find the parameters that minimize the difference between the experimental data and the model, thus an optimization problem.

In this section both integration and optimization schemes used by *FiTGA* package developed in this work are presented.

Integration Scheme The method used to reconstruct the TGA curves is an explicit Runge-Kutta 4(5) method formulated by Dormand and Prince in the 1980s [35]. This method is the default ODE solver of Matlab for non-stiff problems and it is implemented in the function `ode45`. It has adaptive time step, which reduces the calculation time without losing accuracy.

Optimization Optimization means to select the best element from a set using a criterion and usually subjected to some constraints. In many cases, it corresponds to find the maximum or the minimum of an objective function, which is also called “cost function”. A more mathematical description (for a one objective function) of the previous statements is the following equation:

$$\begin{aligned}
\text{Minimize:} \quad & f(\vec{x}) \\
\text{Subject to:} \quad & g_j(\vec{x}) \leq 0 \quad j = 1..m \\
& h_k(\vec{x}) = 0 \quad k = 1..l \\
& x_i^l(\vec{x}) \leq x_i \leq x_i^u(\vec{x}) \quad i = 1..n
\end{aligned}
\tag{2.16}$$

Where: $\vec{x} = \begin{Bmatrix} x_1 \\ x_2 \\ \cdot \\ \cdot \\ \cdot \\ x_n \end{Bmatrix}$

Where the objective function is $f(\vec{x})$, which can be constrained with inequality constraints ($g_j(\vec{x})$), equality constraints ($h_k(\vec{x})$), or bounds. The vector \vec{x} is the vector of parameters that can be modified in the optimization process in order to minimize the objective function.

An optimization procedure can be described with the graph shown in Figure 2.9.

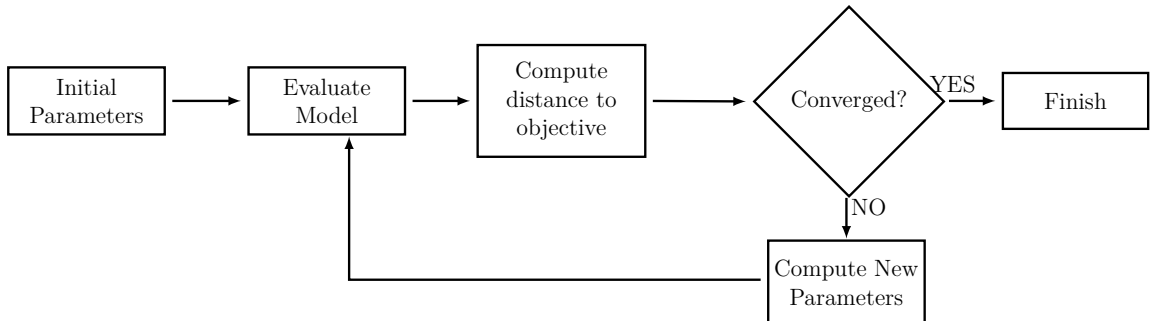


Figure 2.9: Basic optimization scheme

Next, two different optimization algorithms are presented: Trust-Region algorithm and Genetic Algorithm.

Trust-Region algorithm The procedure of fitting TGA data relies on a non-linear least squares method which is capable of obtaining the triplets associated with each reaction that will minimize the difference between the experimental points and the curve generated using a kinetic model. There are many different algorithms that can be used for this application but in this work, it has been found that the most appropriate method is a Trust-Region Reflective algorithm [36] (which, in fact, is the default solver for non-linear least squares fitting in Matlab). This solver shows great robustness, can handle a high number of variables (for each reaction, there are about 4-5 parameters to be fitted, depending on the model chosen), and it allows the user to impose bounds for each variable. Nevertheless, this algorithm only finds local minima which rely on a initial guessing, which in some cases may be difficult to estimate.

In order to understand the basis of the algorithm, it is easier to consider a 2D case (ie. with two unknowns) in which the function $f(x)$ (objective function) is going to be minimized. It can be generalized to n-dimensions. Figure 2.10 is a visual representation of the optimization algorithm.

Let's consider a point x_k which is the point of the current iteration. A Taylor-Series expansion (usually second order) is made around this point, this function is called model function m_k . The calculation of this expansion can be done in different ways depending on the assumptions and the accuracy needed¹.

After this, a region where the model function is a good estimator of the objective function around the current point is calculated, it is a region where the model function is said to be **trusted**. The radius of the Trust Region (Δ_k in Figure 2.10) is calculated based on the agreement between the objective function and the model function in the previous step (Equation 2.17). If the agreement is good ($0 < \rho < 1$), the Trust Region radius is kept for the next iteration; otherwise, the radius will be reduced, since the model function is not a good representation in that region (it cannot be trusted). There are different techniques to calculate the trust region radius, some more conservative and others more aggressive. The conservative techniques are usually slower because they require more steps to reach the solution. On the other hand, more aggressive techniques (which allow bigger Trust Region radius) can be faster in some cases, but they may fail and diverge.

$$\rho_k = \frac{f(x_k) - f(x_k + p_k)}{m_k(0) - m_k(p_k)} \quad (2.17)$$

Once the Trust Region is calculated, the next step is to minimize the model function in this region (which is easier to calculate than the objective function). And since the m_k is a good estimator of $f(x)$, minimizing m_k is equivalent to minimize $f(x)$ inside the Trust Region. By iterating and repeating this process, a local minimum of the objective function $f(x)$ can be found.

¹“Numerical Optimization” [36] presents a good description of the different techniques used in this work.

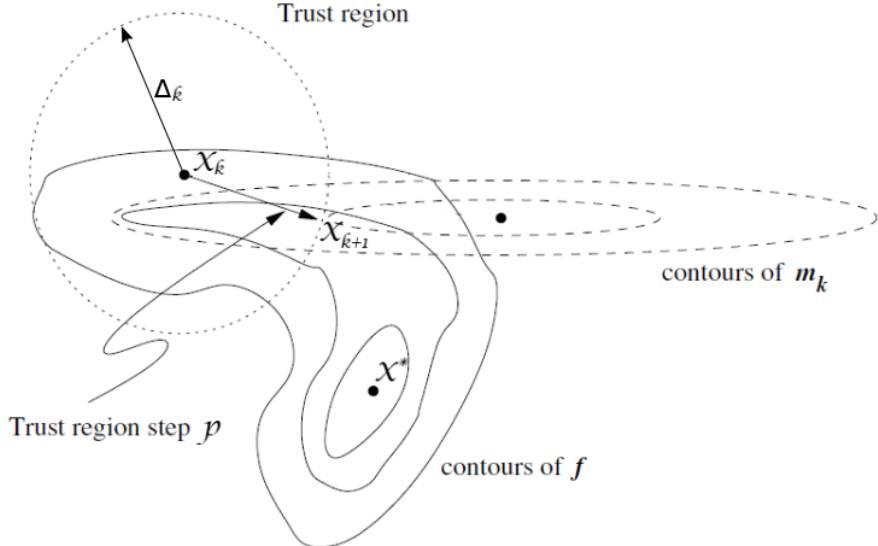


Figure 2.10: 2D representation of the Trust Region Algorithm. Adapted from “Numerical Optimization” [36]

Genetic Algorithm Genetic algorithms try to mimic biological systems: survival of the fittest². In this work, “the fittest” individual, will be the one with the triplet that minimizes the difference between the experimental data and the model. This algorithm is implemented in Matlab in the function `ga`. The following concepts are essential to understand how a genetic algorithm works:

- Population: group of individuals.
- Individual: each of the components of a population, it represents a point in the search space.
- Chromosome: it is the essence of the individual. Each individual has its chromosome which represents the variables of the problem considered.
- Generation: evolution over time (iteration) of the population. In each generation, a new population will be generated following some probabilistic rules.
- Fitness function: function that evaluates how good an individual is.
- Search space: n -dimensional space defined by the bounds of each of the n variables of a GA problem.

In the first generation, a population of a determined size is aleatory generated (or around some specific points, depending on the technique) in the search space. Each of the individuals will have a chromosome representing a specific point of the search space. The fitness of each of the individuals will be evaluated, in other words, see which individuals are the best among the

²More information about genetic algorithms can be found in “Genetic Algorithms in search, optimization and machine learning” [37]

entire population.

The population of the following generation will be created attending to three mechanisms: reproduction, mutation and elitism.

- Reproduction (also known as crossover): Highly fit individuals have a higher probability to mate and reproduce, whereas less fit individuals tend to not reproduce and disappear from the population. These new individuals will have a chromosome which is a kind of mix between the parents.
- Mutation: Some of the individuals will produce a specific mutation creating a new individual with new and different characteristics. This will be used to ensure that all the search space is covered, leading to find a global optimum rather than a local one.
- Elitism: the individuals with the highest fitnesses will pass directly to the following generation.

Different methods can be applied to perform reproduction and mutation calculations. These methods are commonly based on more or less complex statistics.

As said, mutation adds small variations to some of the parameters in a part of the individuals. The selection of parameters and individuals to be mutated is basically performed using probabilities (e.g. Gaussian or uniform) and ensuring, if applicable, that the constraints are accomplished.

Since the parameters intended to be recovered in this work by *FiTGA*, ie. the triplets associated with each chemical reaction, have some boundaries, the method chosen to be applied by default is the *adaptive feasible* method. This method randomly generates directions and step sizes that satisfy the boundaries. The so called “1/5 success rule” of Rechenberg is usually applied to calculate the step size. This rule consists in trying to keep the ratio of successful mutated individuals to 1/5. In other words, if the ratio of successful³ mutated individuals from the previous generation is greater than 1/5, the algorithm has some “confidence” to take bigger steps, which will tend to reduce the ratio since some individuals will mutate to a non-desired part of the search space (but will help to cover it, possibly discovering new points with higher fitnesses); on the other hand, if the ratio is lower than 1/5, the steps taken will be smaller, being more conservative.

The reproduction step is a bit more complex. There are two steps involved: choosing the individuals and performing the reproduction.

The selection of the individuals can be performed in many different ways, some possibilities are listed below:

³An individual is considered successful if it reproduces or it is part of the elite.

- *Tournament*: This is the default method used here in FiTGA. The individuals are arranged in groups of a size that the user has to specify. Then, the individual with the highest fitness will be chosen to be a parent. A variation of this approach consists in sorting the individuals and assigning a decreasing probability to each individual to be chosen.
- *Roulette*: the selection is performed using an idea similar to a fortune wheel. The area corresponding to each individual is proportional to its fitness. This makes individuals with higher fitnesses are more likely to be chosen.
- *Stochastic Uniform*: the individuals are located in a line in intervals proportional to their fitness. A step size is chosen arbitrarily and the algorithm follows the line, if it falls in the interval allocated to an individual, this individual is chosen. This method is similar to the roulette method, however in this case the individuals with higher fitnesses are even more favored.

Once the individuals have been chosen and paired, there are different ways to combine the parameters of each parent individual to create the new generation (reproduction):

- *Scattered*: this is the simplest approach. Some parameters are randomly chosen from one parent or from the other to create the new individual⁴.
- *Arithmetic*: in this approach the child is calculated as a weighted average of the parents, so the child will lay exactly in the middle of the hypercube defined by the parents.
- *Intermediate*: similar to arithmetic, but in this case, a factor controls how close to the parent with the best fitness it will be. This is the default option used in this work, in FiTGA.

Figure 2.11 shows the evolution of a population after several generations. The black dot is the minimum of this function. It can be observed that at the first generation, the dots are more or less randomly distributed. After some generations they go closer to the minimum of the function, in other words, these new individuals have better fitnesses than their parents. At the last generation, it can be observed that all the points are around the minimum, and one of the individuals is exactly in the position of the minimum.

⁴This is equivalent to when a baby is born and people say that he has the eyes of the mom, the nose of the dad, etc.

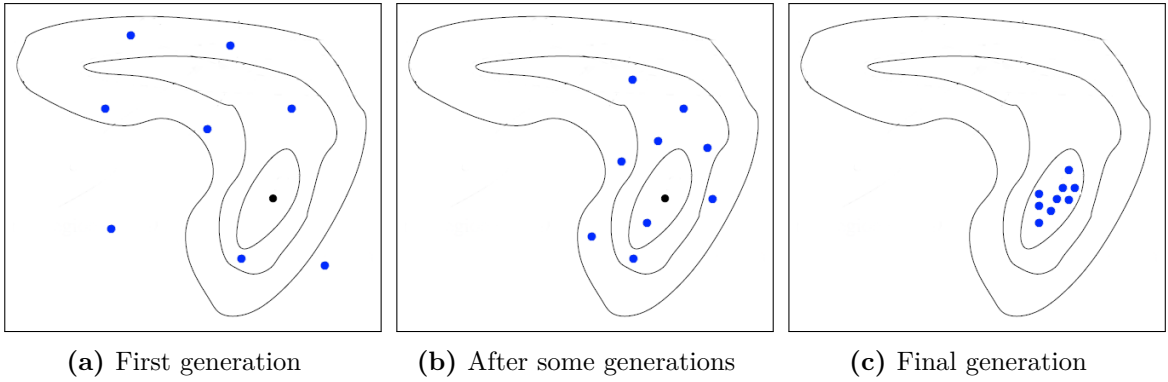


Figure 2.11: Evolution of the population. It can be observed that in the final generation, one of the individuals is at the optimum. Adapted from “Numerical Optimization” [36] to exemplify the Trust-Region Algorithms.

Hybrid Genetic Algorithm A Hybrid Genetic Algorithm (HGA) is a general concept that states the combination of a genetic algorithm with another optimization method. In this case, the hybridization was done with the Trust-Region algorithm presented previously. A HGA pretends to compensate the weaknesses of the two methods that compose it, creating a more robust, accurate, and precise algorithm. Normally, a genetic algorithm (good accuracy, bad precision) is performed until convergence. After that, the other optimization method (bad accuracy, good precision) is launched using as initial guess the individual with the highest fitness obtained by the GA.

Table 2.3 presents a small comparison of the different algorithms. To conclude with this section, we will highlight that if a good initial guess can be achieved, using approximations or literature (if available), the Trust-Region algorithm achieves the solution much faster than the other methods. Nevertheless, if the function has several minima, there is the risk that the Trust-Region Algorithm finds a local minimum and not a global one. Therefore, in cases in which the function is not well known or where a proper initial guessing cannot be done, it is preferable to use HGA.

Table 2.3: Comparison of the different algorithms presented in this section. The HGA presents the pros of the two other algorithms and with only a small increase in calculation time compared with a normal GA.

	Trust Region Algorithm	Genetic Algorithm (GA)	Hybrid GA
Pros	Fast	Global minimum	Global minimum
	High precision	High accuracy Simple calculation	High precision High accuracy
Cons	Local minimum	Slow	Slow
	Needs calculation of gradients	Low precision	More complex calculation

2.2.3 Thermal Analyzer at the VKI

The VKI has a NETZSCH 449 F3 Jupiter Thermal Analyzer capable of performing simultaneous TGA and DSC analysis (Figure 2.12). This model is based on the heat-flux principle. This analyzer has great flexibility and can be adapted to different operating conditions and different types of experiments. TGA/DSC analyzers can be divided into different parts:



Figure 2.12: NETZSCH 449 F3 Jupiter Simultaneous Thermal Analyzer. Courtesy of Netzscht GmbH.

- Furnace: it is the main structure of the TGA/DSC device. It can be made of different materials depending the range of temperatures desired and the atmosphere generated by the samples (oxidizing, reducing, corrosive, etc). Commonly used materials for furnaces are: steel (–150 to 1000 °C), silicon carbide (RT to 1550 °C), platinum (RT to 1500 °C), rhodium (RT to 1650 °C) or graphite (RT to 2000 °C).
- Sample carrier or holder: where the crucibles are located (Figures 2.13a & 2.13b).
- Thermocouples: the sample carrier usually has thermocouples to monitor the temperature of the samples in order to adjust the heat flux.
- Crucibles: capsules where the samples are located. As with the furnaces, they can be made of different materials depending on the requirements. There are several options available (Figure 2.13c): metallic materials as aluminium, silver or platinum; ceramic materials as

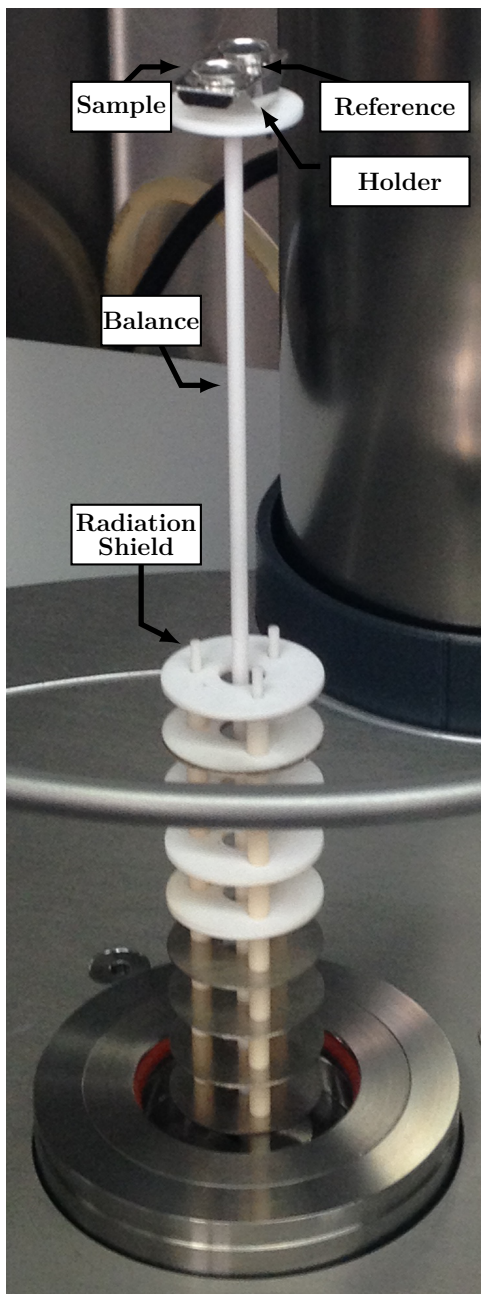
alumina (Al_2O_3), magnesia (MgO), zirconia (ZrO_2); or graphite. The most important characteristic considered when choosing a material for the crucible is that it does not react with the sample. Different types of analysis will require the use of a lid while others will not. For example, an open crucible is used to observe evaporation, a pierced lid creates a self-generated atmosphere slowing down the gas purging process, and with a closed lid, the sample is hermetically sealed (warning: a closed lid can increase the pressure and finally burst the crucible).

- Gas purging system: it is used to purge the gases produced due to the different reactions that the material undergoes. Depending on the sample and the type of analysis, different gases may be used to purge (Nitrogen, Argon, Oxygen or air are commonly used).

When performing c_p determination measurements, it is recommended to use:

- Platinum furnace
- Thermocouples type S (rhodium-10% platinum) for high-precision measurements of temperatures up to 1600 K.
- Rhodium and Platinum (Rh-Pt) with a liner of alumina (Al_2O_3) pierced crucible.

Which is the configuration of our Simultaneous Thermal Analyzer (STA).



(a) Ensemble of components of the thermal analyzer



(b) DSC sensor used for c_p determination



(c) Examples of crucibles. The one used for c_p determination is bottom-right

Figure 2.13: Different components of the NETZSCH 449 F3 Jupiter Thermal Analyzer. Courtesy of NETZSCH GmbH.

The thermal analyzer available at the VKI is located inside a glovebox (Figure 2.14). The glovebox allows to have a very controlled environment to perform the experiments. Temperature, pressure and composition of the gas inside the glovebox are monitored and controlled if needed. The gas that is being used for the moment is Argon due to its non reactive properties.



Figure 2.14: Glovebox where the thermal analyzer is located at the VKI.

All the experiments have been performed with the same temperature range, 30 to 1100 K. This range is the maximum the TGA/DSC device could achieve with the configuration described. Argon is used as atmosphere in the glovebox and in the device as protective gas ($20 \text{ ml} \cdot \text{min}^{-1}$) and purging gas ($50 \text{ ml} \cdot \text{min}^{-1}$). The heating rate (and consequently the mass) were varied in order to optimize the experimental methodology for the thermal characterization of LCAs (Section 3.3).

3 Experimental methodology for heat capacity determination by DSC

In this section, the methodology followed to determine c_p is described in detail. As commented previously, the technique used is the so-called Sapphire method (which is described in the standard ISO 11357 [38]).

3.1 Temperature Calibration

Initially, the calibration of temperature is performed using pure metals whose melting point is well-known. In this case, 6 different metals were chosen: Aluminum, Bismuth, Indium, Silver, Tin, and Zinc. These metals cover the whole range of temperatures of study (30 to 1000 °C).

Each of the metals is heated at a temperature higher than their melting point, followed by two cycles of cooling and heating around the melting point. Each time the metal suffers a transformation (ie. from solid to liquid or vice versa), the DSC curve will register a peak: endothermic or exothermic, depending whether the transformation is a melting or a solidification, respectively.

Since the interest is to heat the materials, only the heating temperature segments of cycles are considered. The experimental temperature at which the melting starts is obtained using *NETZSCH Proteus v6.1* with the onset temperature option. This temperature is the actual temperature measured by the thermocouple, and it is assumed that the metal inside the crucible will be at its theoretical melting point. Figure 3.1 shows as an example, this calibration procedure for Zinc. The onset temperature obtained in this case is 419,8 K, which is very close to its theoretical value (419,5 K).

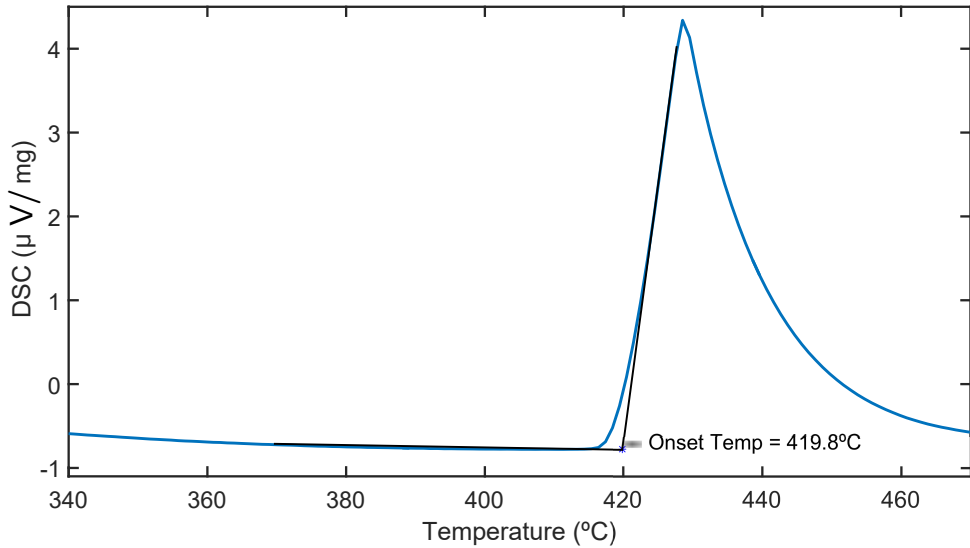


Figure 3.1: DSC curve for Zinc at $40\text{ K} \cdot \text{min}^{-1}$. The onset temperature for melting is 419.8 K which is close to the theoretical value (419.5 K).

The calibration curve can be obtained calculating the onset point of each material and comparing it with the theoretical values. Figure 3.2 shows the quadratic fit obtained using the tool provided by NETZSCH and Equation 3.1 shows the expression of the corrected value of the temperature. In addition, some weighting can be given to each of the metals to increase their importance in the fitting (the higher the weight, the higher the importance), Table 3.1 summarizes the temperatures obtained using a second order polynomial fitting. It can be observed that the errors obtained are very small, under 0.5%.

$$\text{Correction} = 10^{-3}B_0 + 10^{-5}B_1T_{exp} + 10^{-8}B_2T_{exp}^2 \quad (3.1)$$

where $B_0 = 3675$, $B_1 = -2321.6$, $B_2 = 2255.4$ are the coefficients of the 2nd order polynomial.

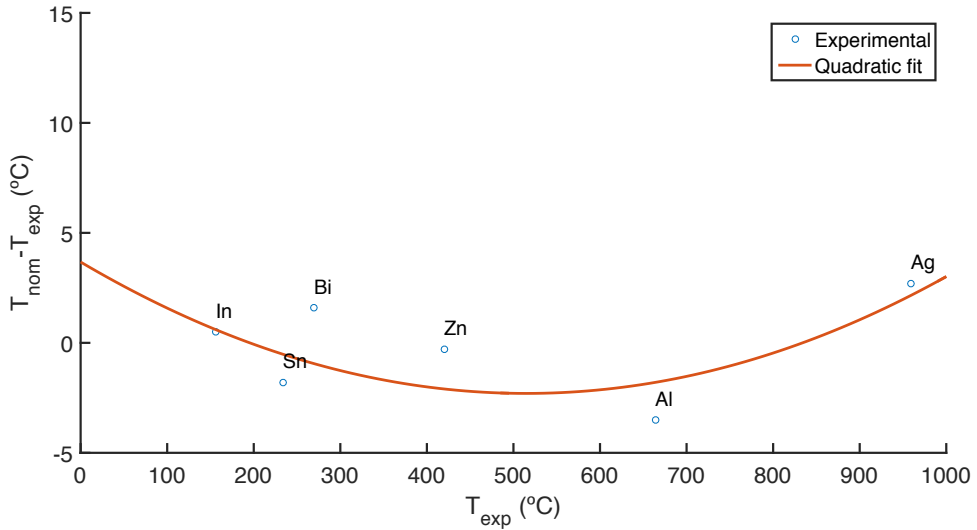


Figure 3.2: Quadratic fit obtained for the temperature calibration.

Table 3.1: Temperature correction obtained with a quadratic fit

	Theoretical [°C]	Observed [°C]	Weight	Corrected [°C]	Percent Error [%]
In	156.6	156.1	10	156.7	0.38
Sn	231.9	233.7	1	233.2	0.22
Bi	271.4	269.8	1	268.9	0.33
Zn	419.5	419.8	0.5	417.7	0.50
Al	660.3	663.8	1	662.0	0.27
Ag	961.8	959.1	1	961.3	0.23

3.2 Heat Capacity accuracy verification

Since the heat capacity of sapphire is well known, two disks of different thickness will be used to verify the accuracy of the measurements. This method consists in checking that one sapphire disk (which will be considered as the sample in this case), provides the proper value for c_p when it is compared with the other sapphire disk.

Following the methodology of the ISO 11357 [38], first we run the blank measurement. After that, in the sample crucible, the sapphire disk of 0,5 mm is inserted to perform the sapphire run. And finally, the other sapphire disk of 1 mm is inserted into the sample crucible.

It can be observed that the c_p obtained for the sapphire disk of 1 mm, which in this case can be considered as the sample, is very close to the theoretical values provided by NETZSCH (Figure 3.3). This indicates that the measurement has been properly performed and that measurements with the real samples can be carried out. Only a certain deviation at the beginning, in the range 25 to 300 °C, can be observed. In this range, the c_p obtained is smaller than the theoretical value about a 3 to 10 %.

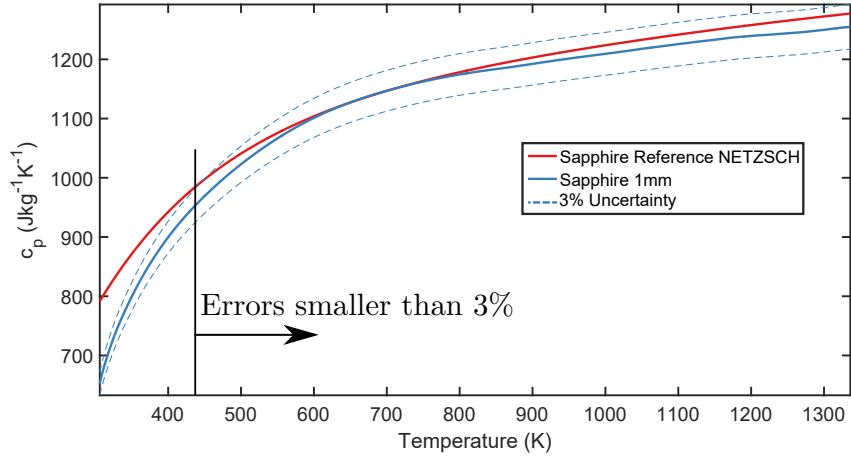


Figure 3.3: Comparison of experimental c_p of sapphire (1 mm thickness disk) and theoretical values at $\beta = 40 \text{ K} \cdot \text{min}^{-1}$. It can be observed that the experiment matches well the theoretical values in the range 300 to 1000 °C

This phenomena can be explained by looking at the DSC curves of both sapphire samples: 0,5 mm and 1 mm (Figure 3.4). Ideally, since the material is the same, the two curves should perfectly overlap in the entire range. Nevertheless, in the range from 25 to 300 °C, the sapphire of 0,5 mm requires more heat per unit mass to increase its temperature. This effect is due to the heating rate and the thermal lag produced in the sample with higher mass (sapphire 1 mm) due to the sudden change from a constant temperature to a heating rate of $40 \text{ K} \cdot \text{min}^{-1}$. Since in this work, we focus on the thermal characterization at high temperatures, we can conclude that in that range, the experimental results show good accuracy presenting errors smaller than 3%.

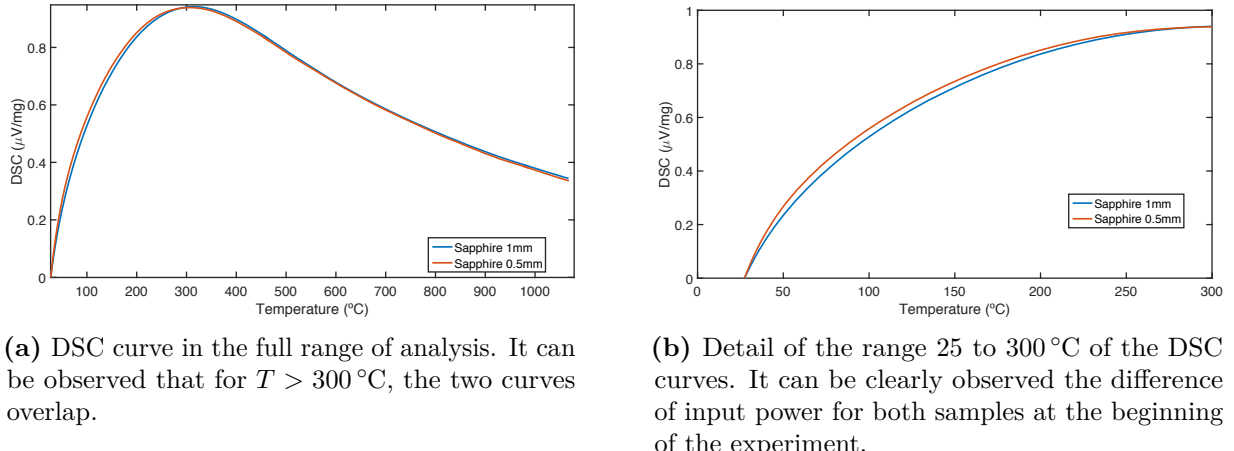


Figure 3.4: DSC curves of both sapphire samples (0,5 mm and 1 mm).

3.3 Experimental Campaign

The first experiments, used to optimize the experimental protocol, were performed with the preform at $20 \text{ K} \cdot \text{min}^{-1}$ and with the original microstructure (small pieces of preform). Another test was also performed with preform powder at $20 \text{ K} \cdot \text{min}^{-1}$. The experimental results of these

samples were compared with c_p data of POCO graphite from the NETZSCH Proteus library.

In general, these experiments showed wrong and inconsistent results (Figure 3.5). First of all, it can be seen that the values of c_p obtained for *Preform 1* are higher than those of the reference graphite. In addition, there are some temperature ranges for the three tests in which the c_p decreases with increasing temperature (dotted circles), which violates physics laws. Furthermore, there are some sudden changes on c_p (solid circles) which do not correspond with any transition of the material. These sudden changes are usually due to poor contact between the material and the crucible, and/or movement and bouncing of the material inside the crucible as pointed out in the literature [39]. In fact, the high porosity of the material hinders the contact between the fibers and the bottom of the crucible, and due to its low density, the material may undergo buoyancy effects inside the crucible. In addition, it can be observed that when the preform gets powdered, the curve obtained is much more smooth and it does not present such artifacts.

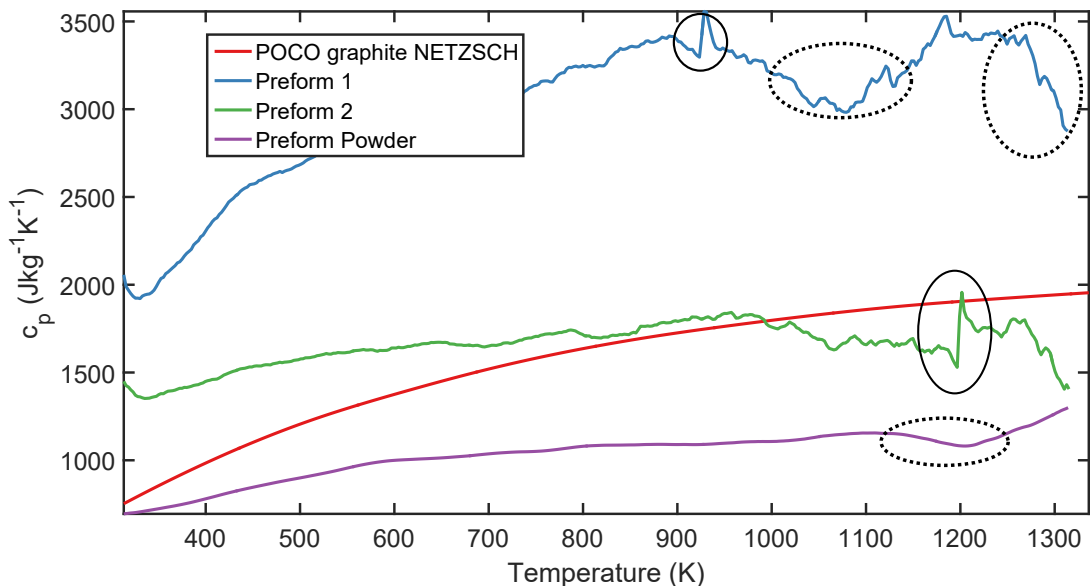


Figure 3.5: Preliminary tests at $20\text{ K} \cdot \text{min}^{-1}$. In red: theoretical c_p of POCO graphite (reference). In green and blue: tests of preform with the original microstructure. In purple: test of preform powder. The higher the mass, the smoother the curve.

On the other hand, the poor accuracy observed in these preliminary tests could also be explained by the low sample mass fitted in the crucible to perform these tests (Table 3.2). This indicates that this sample mass is clearly insufficient to match the sensitivity of the device at this heating rate ($20\text{ K} \cdot \text{min}^{-1}$).

Table 3.2: Preliminary tests with preform at $20\text{ K} \cdot \text{min}^{-1}$.

Test	Mass (mg)
Preform 1	1.613
Preform 2	2.669
Preform Powder	7.603

We can conclude after these preliminary tests that we need to:

- Improve the contact material - crucible.
- Increase the mass that can be fitted in the crucible.

These issues can be sorted out crushing and powdering the material and compressing it inside the crucible, even though this will destroy the microstructure of the material, making impossible to study the effect of the microstructure on the kinetics. Therefore, it was decided to crush the materials and compress them with a Teflon rod in the crucible improving contact and increasing the mass as recommended in [40].

From the user guide of NETZSCH we found out that for a proper measurement, the minimum input power should be at least $P = 5 \text{ mW}$. Considering that the recommended heating rate for c_p measurements is $\beta = 20 \text{ K} \cdot \text{min}^{-1}$ [38] and assuming that $c_p \approx 1 \text{ J} \cdot \text{kg}^{-1} \cdot \text{K}^{-1}$ [41]:

$$\begin{aligned} mc_p\beta &= P \\ m &= \frac{P}{c_p\beta} \\ m &= \frac{5 \text{ mW}}{1 \text{ J} \cdot \text{g}^{-1} \cdot \text{K}^{-1} 20 \text{ K} \cdot \text{min}^{-1}} = 15 \text{ mg} \end{aligned} \quad (3.2)$$

Therefore, it can be assumed that the sample mass needed for the instrument to work properly at $20 \text{ K} \cdot \text{min}^{-1}$ should be $m \approx 15 \text{ mg}$.

However, it was complicated to reach a mass $m \approx 15 \text{ mg}$ in most of the cases. Thus, it was decided to increase the heating rate to $\beta = 40 \text{ K} \cdot \text{min}^{-1}$; by keeping the other parameters of Equation 3.2 as constants, the minimum mass needed could be reduced to $m \approx 7,5 \text{ mg}$ (Table 3.3). This new heating rate may introduce some thermal lag and uncertainties on temperature due to the higher temperature ramp, as well as, it can also affect the kinetics (in the cases of materials that suffer chemical reactions). Nevertheless, in this case there is a trade-off between the heating rate and the mass that can be fitted in the crucible.

Table 3.3: Relation between heating rate and mass. The selected combination is shown in bold.

Heating Rate ($\text{K} \cdot \text{min}^{-1}$)	Minimum mass (mg)
20	15
40	7.5

Another issue we had to deal with when performing the experiments was the high time consumption of the sapphire technique. As previously explained, this technique needs three consecutive measurements. Each measurement takes about 2,5 h, hence 7,5 h per each c_p experiment. For each measurement, we have to perform temperature equilibration (isothermal) until the temperature at which the experiment starts (30°C), next a linear increase of

temperature at $40 \text{ K} \cdot \text{min}^{-1}$ until 1100°C followed by another equilibration (isothermal) at the maximum temperature (Figure 3.6), and after that there is the cooling down. In addition, we need to include the sample preparation time. Table 3.4 summarizes an estimate of the time consumed by each activity.

Therefore, after some satisfactory experiments, it was decided to use the same two blank and sapphire measurements for more than one sample. In other words, every day we performed a blank and a sapphire measurement and after that, we performed two samples of actual material of interest.

Table 3.4: Breakdown of time spent by each measurement

	Time (h)
Isothermal @ 30°C	0.25
Heating @ $40^\circ\text{C} \cdot \text{min}^{-1}$	0.4
Isothermal @ 1100°C	0.25
Cooling	1
Manipulation	0.5
Time per measurement	2.5
Total time	7.5

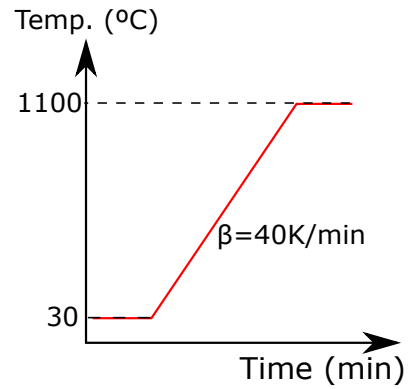


Figure 3.6: Temperature profile used by the Sapphire technique

3.4 Heat capacity results

In this section, the results of the experiments, once the methodology has been optimized, will be presented and compared with the literature available also pointing out possible improvements that should be done in future studies.

Four different materials have been tested following the methodology presented above. First of all, since most of the materials that were going to be tested are carbon-based, we decided to perform a test case with POCO Graphite, whose c_p can be easily found in literature and use it as reference for comparisons [41]. After that, we moved to the preform, followed by the phenolic resin and Asterm. Table 3.5 presents the test matrix with the experiments performed.

In the cases of Asterm and the phenolic resin, since there are chemical reactions of pyrolysis where c_p cannot be obtained easily¹, it was decided to **run the experiment twice**: first with the virgin material and after with the char produced, and **analyze the char** which does not undergo any reaction in the temperature range considered. In addition, considering that the phenolic resin has about a 40% of mass loss, the char produced during several experiments was

¹Obtaining c_p in cases with chemical reactions needs special data treatment. The two contributions (c_p and chemical reactions) to the heat absorbed by the sample need to be separated. This is out of the scope of this thesis.

Table 3.5: Test matrix with the different experiments performed for c_p determination ($\beta = 40 \text{ K} \cdot \text{min}^{-1}$). The subscript bis means repetition with the same material.

Material	Name	Mass (mg)	Comments
Graphite	Graphite 1	13.644	Piece of graphite
	Graphite 1 bis	13.644	Repetition of Graphite 1
Preform	Preform Powder 1	11.871	
	Preform Powder 2	13.669	
	Preform powder 3	15.216	
	Preform powder 3 bis	15.216	Repetition of Preform Powder 3
Resin	Resin 1	9.958	
	Resin 2	14.069	
	Resin 3	13.064	
Resin char	Resin Char 1	12.471	Char of the three experiments of resin above
	Resin Char 1 bis	12.471	Repetition of Resin Char 1
Asterm	Asterm 1	16.976	
	Asterm 2	18.077	
Asterm char	Asterm 1 bis	13.626	Test with char of Asterm 1
	Asterm 2 bis	14.347	Test with char of Asterm 2

collected, compressed and tested following the same methodology.

The results will be presented following the same structure: firstly, a comparison between the average c_p obtained for the material and a reference (graphite), focusing in possible discrepancies and errors. Secondly, a curve will be calculated using a regression model from the literature [41] (Equation 3.3), for data validation. Furthermore, this empirical relation can be used to predict c_p at any point of the temperature range.

$$c_p(T) = a + b \cdot T + c/T \quad (3.3)$$

3.4.1 Heat capacity of Graphite

Graphite is not an aerospace material, however carbon is the main component of some of the other materials (carbon fibers, resin char, Asterm char). In addition, there is literature available [41, 42] for comparison. Therefore, it was decided to conduct some tests with graphite in order to check literature results, thus having a reference for the other measurements.

In Figure 3.7, the red curve is the reference of POCO graphite from NETZSCH Proteus software library and the blue curve is the average of the two tests performed with graphite, with the 3% of uncertainty boundaries. It can be seen that the two curves have a similar shape and they are almost overlapped in part of the temperature range. Nevertheless, some discrepancies are observed:

- At the beginning of the curve, one can see that the c_p obtained is slightly higher than the reference. This discrepancy can be explained by the thermal lag for the sudden change from a constant temperature to a heating rate of $40 \text{ K} \cdot \text{min}^{-1}$, similarly to what was previously found in the validation tests with the sapphires disks.
- At high temperatures (dotted circle in Figure 3.7), one can observe also some discrepancies. Even though the values obtained are still close to the reference curve, the slope increases rapidly at $T = 1200 \text{ K}$. The literature has been reviewed and no answer has been found yet for this disagreement. Further measurements at different heating rates should be performed in order to check whether it is an artifact, or an unexpected phenomena is occurring.

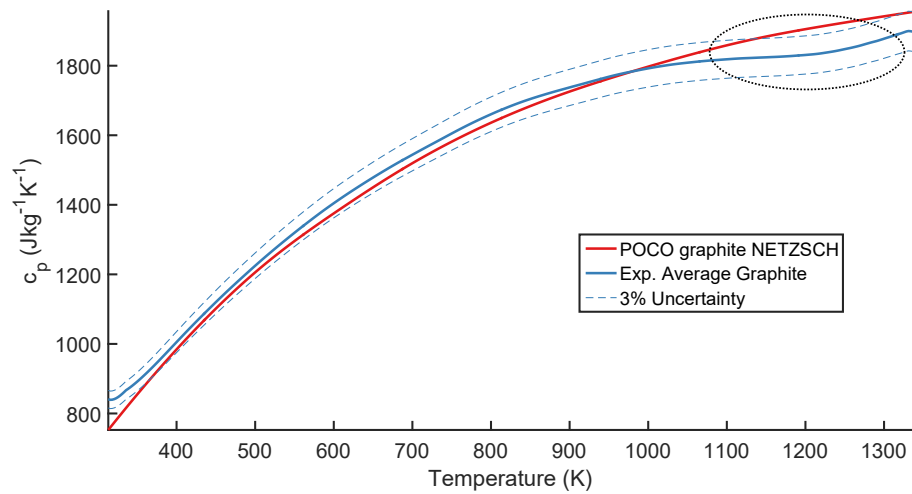


Figure 3.7: Comparison of experimental results of c_p for graphite and the reference from NETZSCH. Discrepancies are shown in dotted circle.

Next, the experimental data were fitted to Equation 3.3. In this case, the relationship is given by: $c_p(T) = 2126.8 + 0.0911T - 4,537 \times 10^5 / T (\text{J} \cdot \text{kg}^{-1} \cdot \text{K}^{-1})$ with a regression coefficient equal to $R^2 = 0.991$, which shows good agreement between the experimental data and the model. The dotted line represents the 95 % confidence interval for the constants that fit the model.

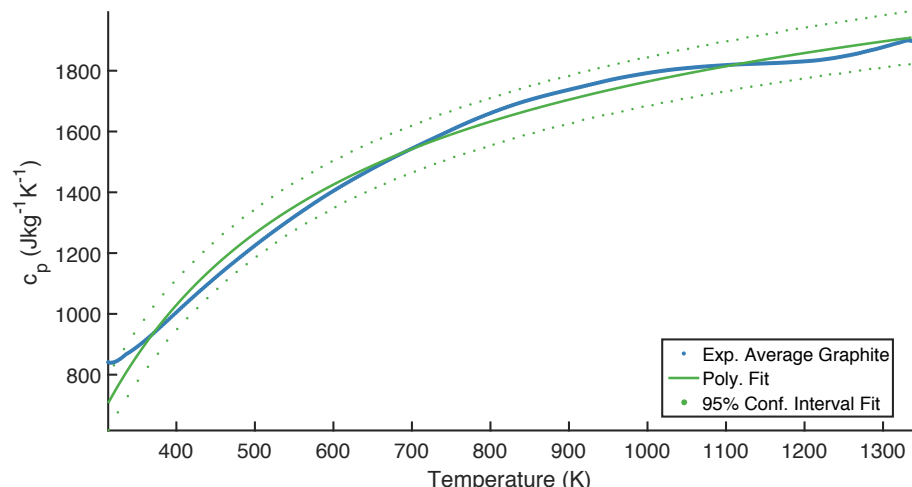


Figure 3.8: Curve fitting (green) for the experimental values of c_p of graphite (blue).

3.4.2 Heat capacity of Preform

Since the preform is composed by short carbon fibers, it seems a reasonable hypothesis to consider that the c_p obtained with the powder of these fibers should be similar to the c_p of graphite. Figure 3.9 shows that the values of c_p obtained from preform are slightly smaller than those of the reference graphite, but both curves follow the same tendencies. As for graphite samples a change in the slope can be also observed around $T = 1200\text{ K}$ (dotted circle) which requires further investigations.

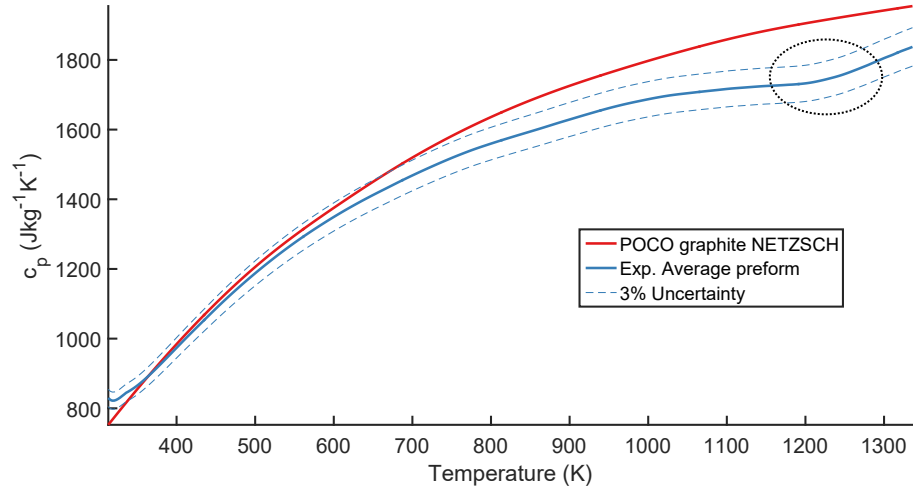


Figure 3.9: Comparison of experimental results of c_p for preform and the reference graphite from NETZSCH. Lower values of c_p have been obtained for preform.

These experimental data have also been fitted to a polynomial model. The results obtained are shown in Figure 3.10. One can observe that there is a good agreement, as proven by the regression coefficient $R^2 = 0.995$. In this case, the relationship is given by: $c_p(T) = 1933.8 + 0.1305T - 3,945 \times 10^5/T (\text{J} \cdot \text{kg}^{-1} \cdot \text{K}^{-1})$.

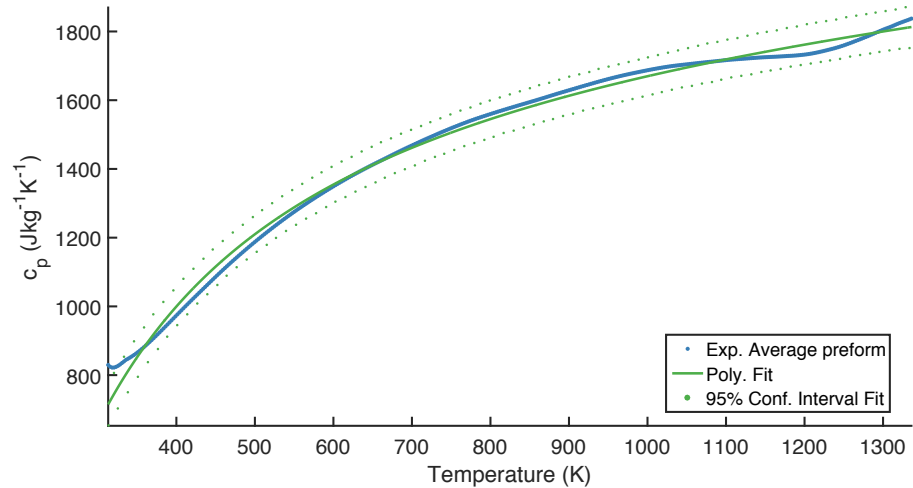


Figure 3.10: Curve fitting (green) for the experimental values of c_p of preform (blue).

3.4.3 Heat capacity of Resin char

As previously explained, the heat capacity cannot be easily calculated when chemical reactions are occurring. The virgin phenolic resin undergoes several chemical reactions in the range of temperatures of study. Figure 3.11 shows the apparent c_p obtained for resin when chemical reactions are occurring. This data need special treatment to decouple the effect of the pyrolysis processes and the actual c_p with a correction for the mass loss.

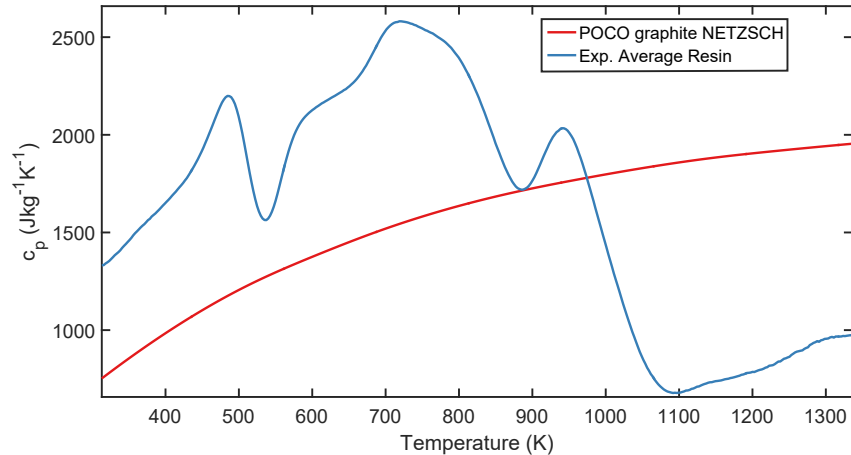
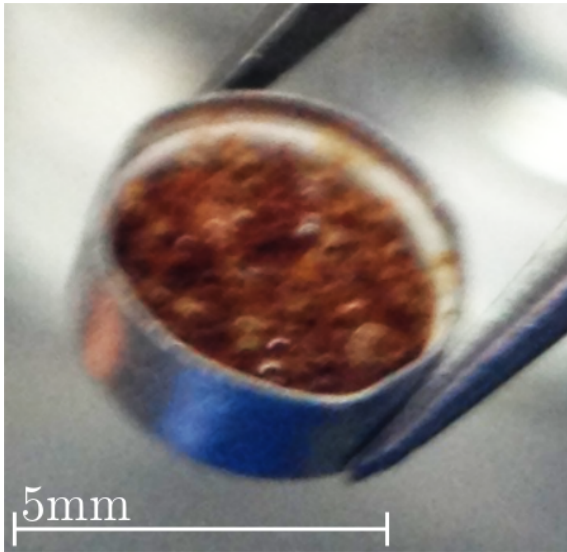
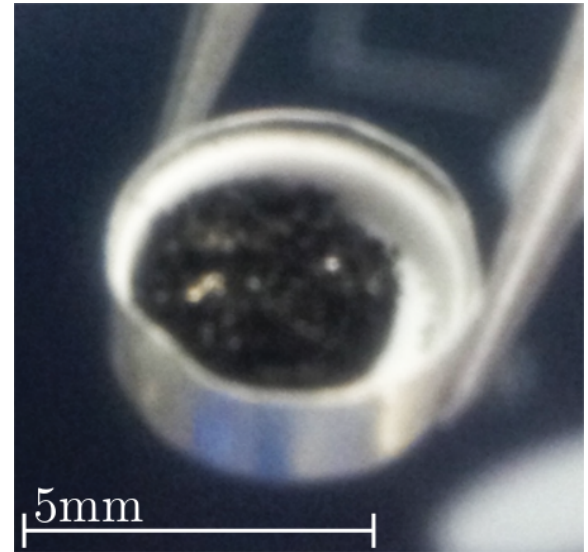


Figure 3.11: Apparent c_p of resin when chemical reactions are occurring.

Therefore, for validation purposes it was decided to calculate the c_p of the char of the material. This char was obtained performing three experiments with resin and collecting the residue (Figure 3.12). This residue was compressed and tested afterwards. The experiment was repeated with the same conditions and material to observe the repeatability of these type of experiments. In Figure 3.13a, the average c_p obtained for the two repetitions can be seen. The values obtained are lower than the graphite reference, being similar to the values obtained for preform. Nevertheless, as it can be seen in Figure 3.13b the differences between the two experiments are significant thus, from here one can conclude that the repeatability of DSC experiments is low, and many repetitions should be performed in order to have proper averaged values.

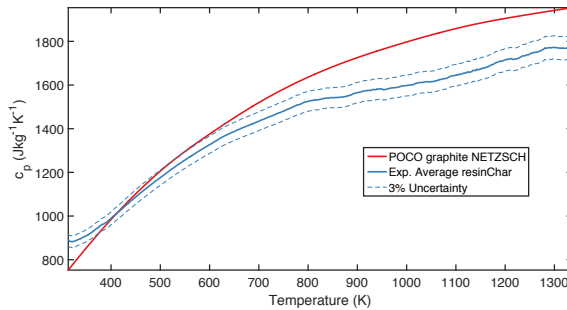


(a) Virgin resin. A brownish color can be seen.

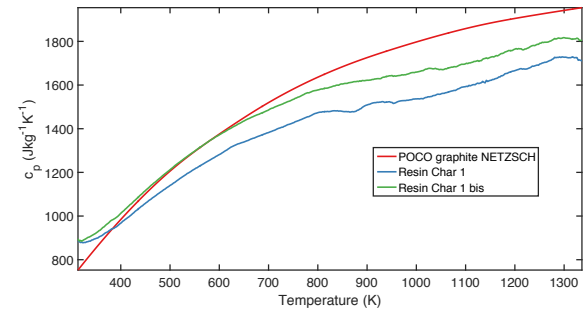


(b) Charred resin. The black color denotes that it has been carbonized.

Figure 3.12: Crucible with resin before (left) and after (right) the experiment.



(a) Lower values have been obtained for the average c_p of the resin char.



(b) Two repetitions of the test of the resin char. The low repeatability of DSC experiments can be observed.

Figure 3.13: Comparison of experimental results of c_p for the resin char and the graphite reference from NETZSCH.

A polynomial fit was then performed with these experimental data. The results (Figure 3.14) show good agreement with the experimental data and the correlation coefficient is also good ($R^2 = 0.993$). In this case the empirical relation was found to be: $c_p(T) = 1700 + 0.2224T - 3.07 \times 10^5/T$ ($\text{J} \cdot \text{kg}^{-1} \cdot \text{K}^{-1}$)

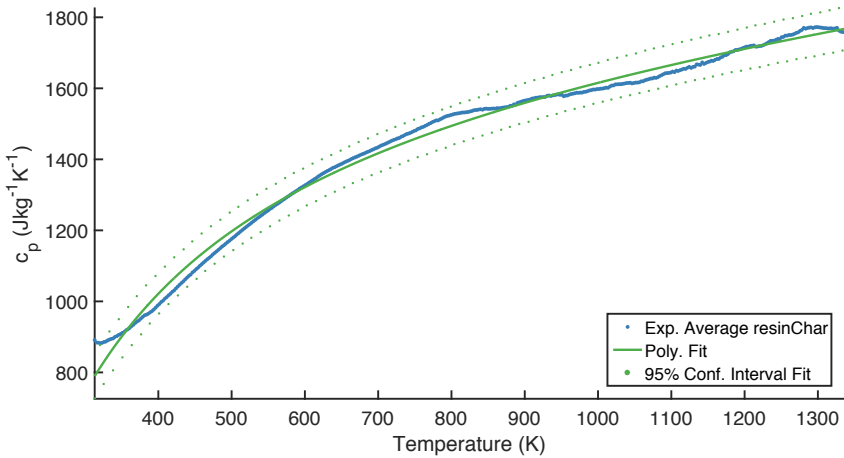


Figure 3.14: Polynomial fit for resin char. Good agreement was found with the experimental data.

3.4.4 Heat capacity of Astem char

The case of Astem is similar to that of the pure phenolic resin because this composite material will undergo similar chemical reactions than the resin. Therefore, an experiment with virgin Astem was done, and that char was directly tested. The char of Astem is composed by residue of both phenolic resin and carbon fibers. Therefore, it was expected to obtain similar values to the resin and the preform. Nevertheless, as seen in Figure 3.15 the results obtained are smaller. This may be due to a poor contact between the material and the crucible since the char was tested without being compressed. Further tests should be performed to confirm this hypothesis.

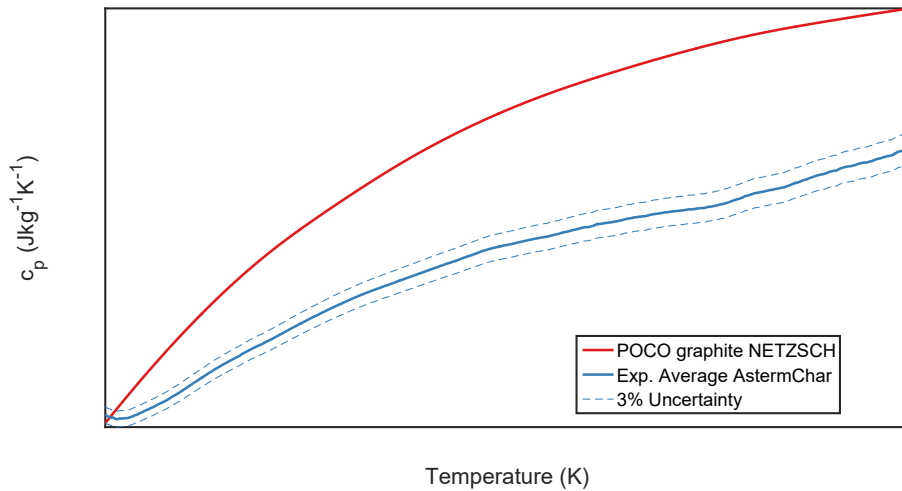


Figure 3.15: Comparison of experimental results of c_p for Astem char and the graphite reference from NETZSCH. The values obtained are smaller than the previous cases. Axis omitted for confidentiality.

4 TGA Curve Fitting — *FiTGA* Software Package

Thermogravimetric Analysis experiments need to be processed in such a way that the kinetic parameters associated with each reaction are recovered. As previously explained, there are different ways to obtain them depending on the model used, but they usually rely on simplifications [21] or on commercial software. In addition, the models that are currently used in aerospace research are not available (yet) in commercial codes.

Therefore, it was decided to develop a software named *FiTGA*, capable of fitting experimental TGA data using a kinetic model. Thus, being able to recover the kinetic triplets associated with each reaction.

The main objective of *FiTGA* is to provide an open-source environment to analyze TGA data for aerospace research. It has been developed in MATLAB because it has many built-in functions for integration and optimization problems, and it can be run in different Operative Systems. The implementation has been done in such a way that any user can add and use new models easily. For the moment, there are two models available: the one proposed by G. Pinaud [15] and the one proposed by J. Lachaud [43] and three different optimization algorithms: A non-linear least squares method, a genetic algorithm and a hybrid genetic algorithm.

The structure of *FiTGA* can be divided in three parts: preprocessing, fitting and post-processing. The preprocessing module offers the user the possibility to perform some data treatment (sampling, smoothing using a moving average method, and selecting a specific range of temperatures to study) as well as to specify other parameters such as the material of the sample, the model that will be used, or the optimization algorithm. The fitting module will be described in detail in the next section but it basically performs the appropriate calculations to obtain the kinetic parameters. And finally, the post-processing module is used to generate different files (plots and tables) so that the user can interpret the results easily. Figure 4.1 shows the structure described previously.

For its input files, *FiTGA* uses YAML config files. YAML is a data storage language specifically designed to be human readable [44]. There are input/output libraries available for many different programming languages including MATLAB and Python. In addition, many of the data types of MATLAB are directly read/written by YALM, simplifying importing/exporting data. It was decided to use a config file system for *FiTGA* in order to completely separate the code from the user inputs clearing up the code for non-MATLAB users.

A more complete review of the package with step-by-step tutorials and examples can be found in the Annex B.

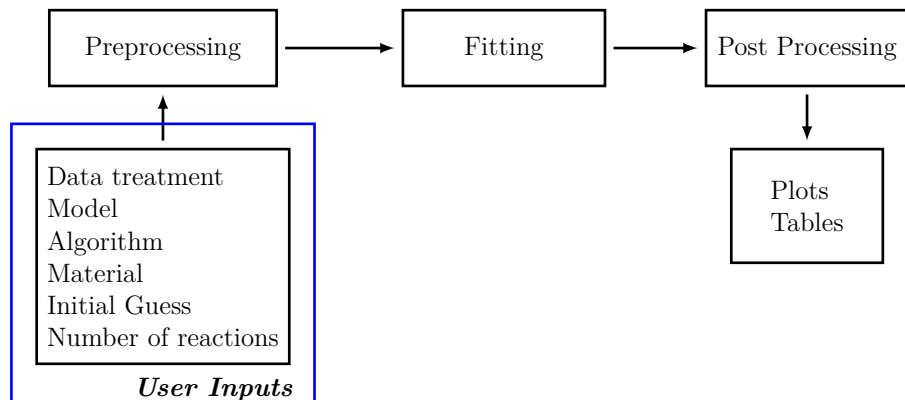


Figure 4.1: Workflow diagram for FiTGA.

4.1 Fitting Algorithm

The Fitting algorithm can be divided in two main tasks: **curve reconstruction** and **optimization of the parameters**. Curve reconstruction consists in generating a theoretical TGA profile using an imposed model. And the optimization of the parameters consists in finding the set of kinetic parameters associated to the chosen kinetic model that minimizes the difference between the reconstructed curve and the experimental data.

4.1.1 TGA Curve Reconstruction

The curve reconstruction is nested inside the optimization process. In other words, the algorithm will generate theoretical curves and compare them to the experimental data until convergence.

Given a set of parameters and a model, the algorithm reconstructs a TGA profile: it integrates the equation corresponding to the model used. Figure 4.2 exemplifies the process considering the case of the PATO model.

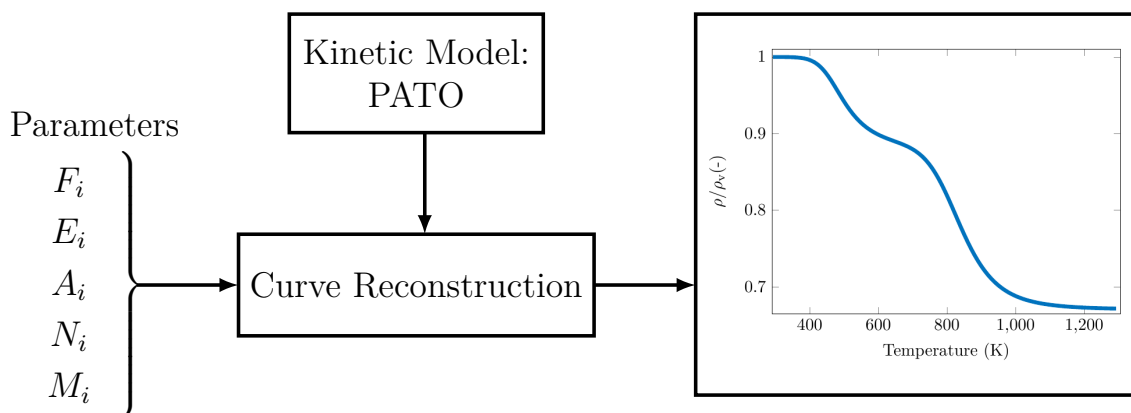


Figure 4.2: Curve reconstruction for PATO.

4.1.2 Minimization Process

As commented before, the minimization process is an iterative process. In this process, the difference between the reconstructed curve (generated with a specific set of kinetic parameters) and the experimental data will be evaluated trying to find a minimum, which will be the solution to the fitting problem. This process is a bit different depending on the chosen optimization algorithm.

In the case of the non-linear Least Squares Method (nonlinLSQ)¹, the algorithm starts with an initial guess (and boundaries) for each parameter. This initial guess, will generate a reconstructed curve using the methodology explained previously. This curve will be compared to the experimental data, and once the tolerances have been accomplished, the algorithm will stop. Otherwise, it will calculate a new set of parameters and repeat the process until convergence. As previously explained, this optimization method can lead to a local minimum rather than a global one, and hence to a wrong solution.

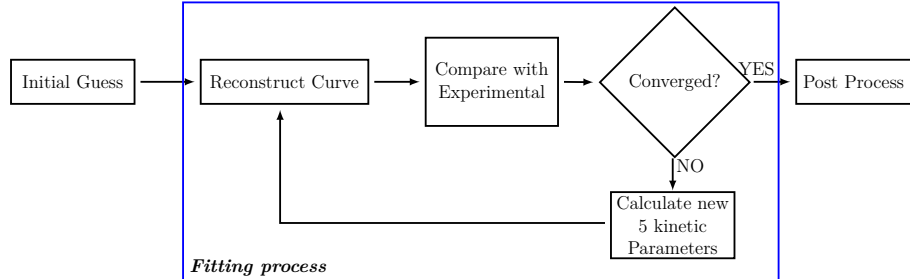


Figure 4.3: Flowchart for the algorithm nonlinLSQ used in *FiTGA* to retrieve the kinetic parameters.

The genetic algorithm (GA) does not need an initial guess. For the GA, the bounds for each variable are provided and the algorithm will generate a population of a determined size. In each generation, each individual will be compared to the experimental data. Using mechanisms such as mutation and crossover, generation after generation the population will be better and closer to the solution.

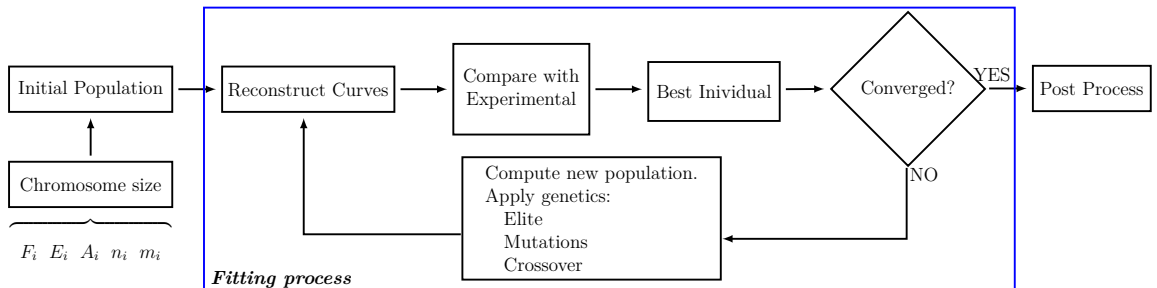


Figure 4.4: Flowchart for the Genetic Algorithm implemented in *FiTGA*.

¹nonlinLSQ is implemented on MATLAB in the function `lsqnonlin`.

The two methods described before can be combined in a Hybrid Genetic Algorithm (GA+LSQ), providing with the benefits of both algorithms. First, a GA is launched until it reaches a solution. This solution is the best that GA could find with the parameters given, but it may not be the best. Therefore, a nonlinLSQ is launched after using as initial guess the fittest individual obtained by GA. This second optimization will lead to a result with a higher accuracy.

This third algorithm may seem more computationally expensive than the other two. Nevertheless, it ensures independence from the initial guess thanks to the use of GA leading to a global minimum rather than the possible local minimum that may be found with nonlinLSQ. In addition, for a given accuracy, this method converges faster than the GA; once a good approximation of the solution is obtained by GA, the nonlinLSQ will run much faster and converge in a few more iterations.

4.2 Sensitivity Analysis

When performing the first tests of the code using simulated TGA data, small discrepancies were found between the input data and the recovered parameters. Therefore, it was concluded that it was necessary to perform a sensitivity analysis in order to quantify the impact of each parameter in the Equation 2.15²(Airbus kinetic model).

The idea proposed was to consider a simulated curve with one Arrhenius reaction using arbitrary numbers for the triplet (F, n, A, E) as a baseline. Once the baseline is defined, each variable is increased and decreased at fixed percentage (15%) obtaining 4-dimension hypercube where the baseline point is located at the center and each variable of the kinetic triplet defines a dimension of the hypercube. Doing this, we can simulate a new curve at any point of the hypercube and measure the error using Equation 4.1:

$$S = \sum_{k=1}^{n_{\text{points}}} (\rho_{\text{baseline},k}(A, N, E, F) - \rho_{\text{calc},k}(A', N', E', F'))^2 \quad (4.1)$$

from this point, two approaches were followed: the first one consists of a basic ANalysis Of VAriance (ANOVA) technique and the second one using a more complex ANOVA applying a Monte Carlo approach, the so called Sobol Indices.

A function $f(x)$ (where x is a vector of the input variables), can be expressed in the so called ANOVA form (Equation 4.2). This equation allows to calculate the simple (main) effects (due to the change of the input variable) and the total effects (considering also interactions). In the case of interactions, usually only first order interactions are studied, this is to study the effect of changing two variables at a time. A detailed mathematical description is available in the

²The same approach could be used to analyze Equation 2.14. It was decided to skip this step since both equations are very similar.

literature [45].

$$f(x) = \underbrace{f_0}_{\text{main effects}} + \underbrace{\sum_{i=1}^n \sum_{j_1 < \dots < j_i} f_{j_1 \dots j_i}(x_{j_1}, \dots, x_{j_i})}_{\text{interactions}} \quad (4.2)$$

4.2.1 Sensitivity Analysis using ANOVA

For the ANOVA approach, it was considered that the boundaries of the hypercube define two levels for each variable (low and high). Therefore, there are $2^4 = 16$ combinations. These points were evaluated using Equation 4.1 and the parameter S was obtained. These results were put in a statistical package (StatGraphics) and an ANOVA analysis was performed. Figure 4.5 shows the effect of the variation of each parameter, where the ordinate axis is the sum of the squares of the main effects which is the variation attributed to the change in one variable. It can be seen that changing the value of the parameter A does not affect significantly the solution (the curve is almost flat). On the other hand, the variation of E affects considerably the solution (the slope is much higher).

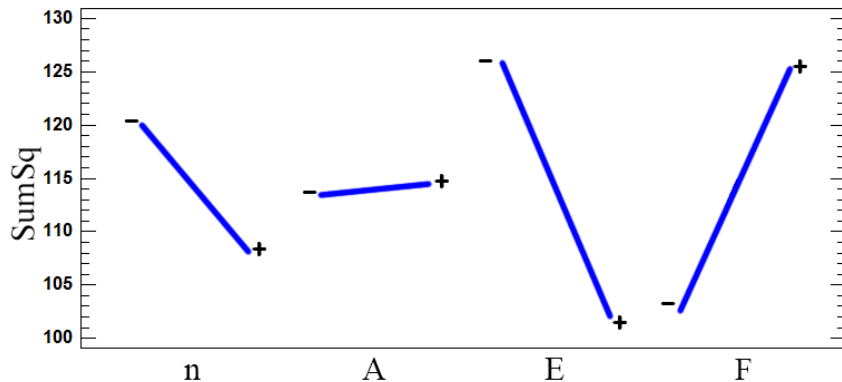


Figure 4.5: Contribution of each variable to the main effects. The higher the slope, the more important a parameter is.

Considering also first order interactions, this is when more than one variable is changed at a time, it can be observed that the parameter A does not have statistical significance (for $\alpha = 0.05$). The most important effect takes place when the combination between E and F is negative (ie. E low and F high, Figure 4.6).

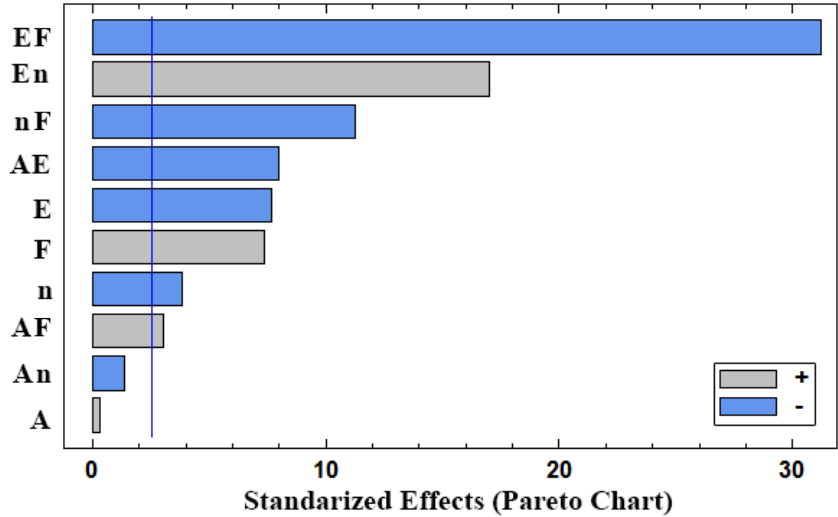


Figure 4.6: Pareto chart with first order interactions. It can be pointed out that the bars that do not reach the value of the vertical blue line (A , An) are not significant from the statistical point of view.

4.2.2 Sensitivity Analysis using Sobol Indices

The second approach is based on a Monte Carlo technique. It was decided to use a Global Sensitivity Analysis package developed by Francesca Pianosi et al. [46]. Three different techniques were used: Elementary Effects Test (EET), Variance Based Sensitivity Analysis (VBSA or Sobol Method) and Fourier Amplitude Sensitivity Test (FAST).

4.2.2.1 Elementary Effects Test (EET)

The ETT is a simple test with relatively low computational cost that calculates the total effect of an input variable (x_i) on its mean μ_i . The standard deviation σ_i gives an idea of the interactions and non-linear effects. In this test, only one variable is varied at a time. The EET for a variable x_i is calculated as follows:

$$EE_i = \frac{f(x_1, x_2, \dots, x_{i-1}, x_i + \Delta, \dots, x_k) - f(x_1, x_2, \dots, x_k)}{\Delta}$$

$$\mu_i^* = \frac{1}{r} \sum_{j=1}^r |EE_i^j|$$

$$\sigma_i = \sqrt{\frac{1}{(r-1)} \sum_{j=1}^r (EE_i - \mu_i)^2} \quad (4.3)$$

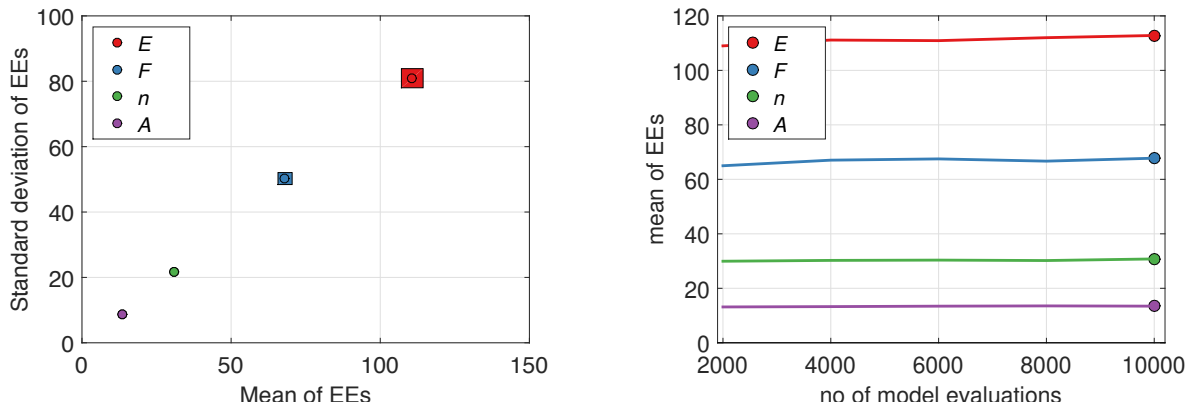
Where:

- x_i is each of the variables.
- $f(x_1, x_2, \dots, x_k)$ is a scalar result of the evaluation of the function.
- EE_i is the elementary effect associated to the variable x_i .

- r is the number of points for each factor.
- Δ is the increment for the variable x_i .
- μ_i^* is the mean associated with the variable x_i .
- σ_i is the standard deviation associated with the variable x_i .

Figure 4.7a shows the mean and the standard deviation of the EET, it can be observed that E has the most important effect since its mean is higher than the other effects. Its standard deviation is also high, which means that non-linear effects and interactions are important (as it was already guessed with ANOVA). On the other hand, the parameter A presents a small mean and standard deviation. F is also a critical parameter, but as commented previously, it can be estimated with reasonable accuracy from the plots.

Since this methodology is based on a Monte Carlo method, it is compulsory to check if the number of samples is representative performing a convergence analysis (ie. repeating the test for different number of samples, and checking that the values obtained tend to a constant value). In Figure 4.7b, it can be observed that the mean of the input parameters follow almost a straight line, which means that they have reached convergence, and validates the methodology applied.



(a) Mean and standard deviation of the EET with confidence bounds. A high mean implies that a parameter is more important with respect to the others. The standard deviation gives an idea of the importance of non-linear effects.

(b) Convergence curves. It can be observed that after ~ 3000 iterations the curves are totally horizontal, which indicates that converge has been reached.

Figure 4.7: Results obtained with the EET test

4.2.2.2 Variance Based Sensitivity Analysis (VBSA)

The second methodology applied for the sensitivity analysis is VBSA or Sobol's method. This technique provides the so called Sobol's indices which represent the effect of an input variable over the output value. Using this procedure, it is possible to calculate the first order effects (main contribution of each input factor to the variance of the output) and the total effects (effect of the main contribution plus higher order effects). The first order effects (or main effects) for

each input are calculated using Equation 4.4.

$$S_i = \frac{V[EV(f|x_i)]}{V(f)} \quad (4.4)$$

In order to calculate the total effects for the input variable x_i , Equation 4.5 is applied. In this case, the expected value (EV) is calculated considering all the variables except the variable of interest ($x_{\sim i}$).

$$S_{T_i} = 1 - \frac{V[EV(f|x_{\sim i})]}{V(f)} \quad (4.5)$$

Figure 4.8 shows both main and total effects, with their confidence bounds (considering a 95 % confidence level). The main conclusions that can be extracted from here are analogous to the ones presented for EET. It can be observed that in the case of main effects, the parameters A and n present a negative Sobol index, this would mean that the variance is negative which is not possible. This is due to the applied methodology and according to the literature [45] a negative Sobol index should be considered as 0, which means that it does not have significance on the space considered. In addition, it can be observed that positive values may be obtained when considering the confidence bounds, which justifies that A and n have small influence on the equation.

In this case, it is also essential to perform a convergence study (Figure 4.9). It can be seen that now, the convergence is not as good as in the previous case, but it also seems to tend to a value. A higher number of iterations could be done to ensure convergence, but due to technical limitations (CPU and time) we decided to stop at this point. It can be clearly seen that the results are more accurate (and there is a distinction between first order and total effects), but this methodology is more computationally expensive.

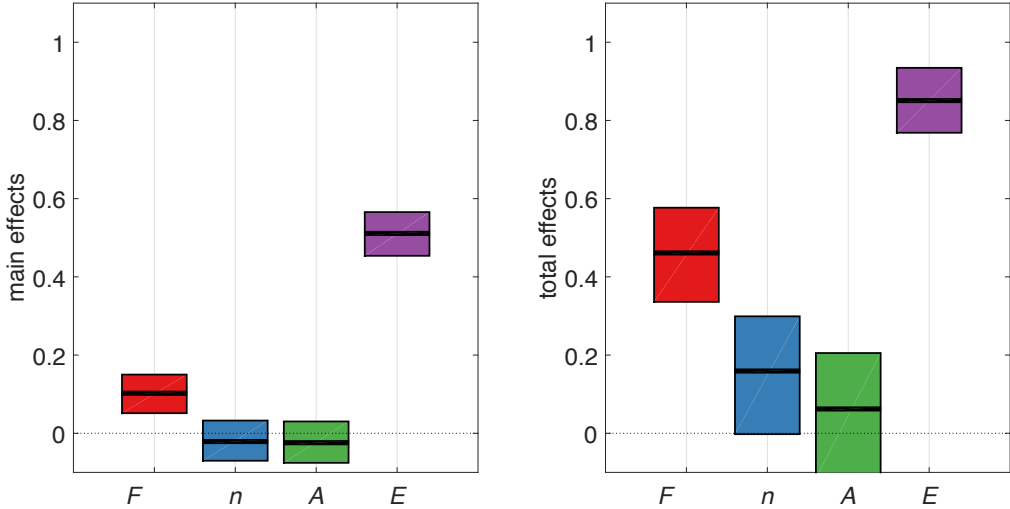


Figure 4.8: VBSA results: left – main effects; right – total effects. It can be pointed out that the effect of the variables n and A is very small compared to the effect of the other two variables (F and E) in both main and total effects.

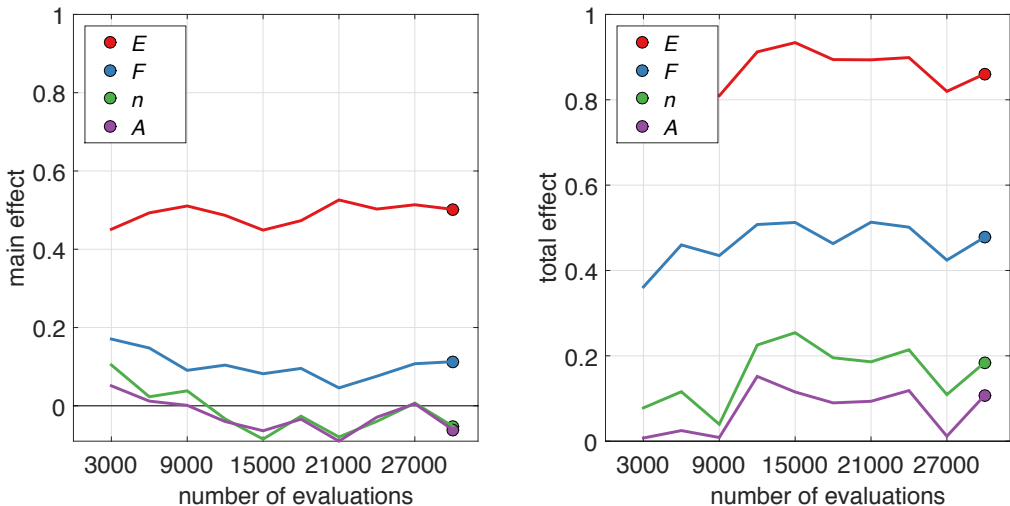


Figure 4.9: Convergence curves for VBSA algorithm. It can be observed that when increasing the number of evaluations of the model, the parameters tend to a value.

4.2.2.3 Fourier Amplitude Sensitivity Analysis

The last methodology used is Fourier Amplitude Sensitivity Analysis (FAST). This procedure uses a Fourier series decomposition on the output to calculate first order sensitivity indices [45]. It needs to be highlighted that this method calculates the number of points needed and samples the space automatically ensuring that there are no interferences. In the present case, the number of sample points is reduced to two orders of magnitude, which reduces calculation time considerably (from around 5 h to about 30 min). This can be very interesting for future studies with a higher computational cost involving Sensitivity Analysis. Figure 4.10a shows that the first order effects calculated using this method are similar to the values obtained using VBSA

(Figure 4.8). In addition, the converge of this method seems much better than VBSA (Figures 4.9 and 4.10b) since it keeps an almost horizontal line from 1500 evaluations.

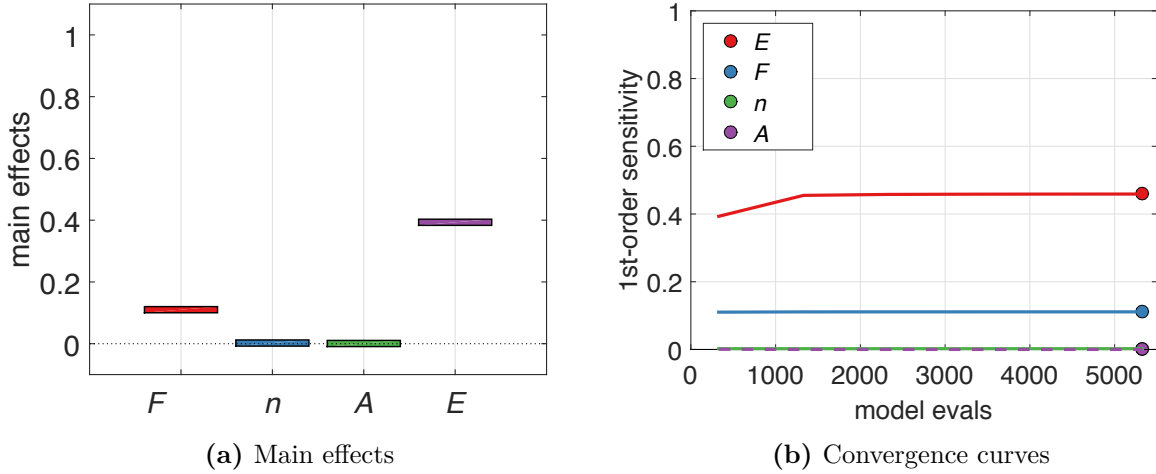


Figure 4.10: Results obtained with the FAST algorithm

4.2.2.4 Probability Distribution Function

To conclude with the statistical analysis, it was considered interesting to see the evolution of the probability distribution function (PDF) associated to the density loss generated with the Monte Carlo sampling (with 16000 points). The following graph has been generated considering a fixed value of $F = 0.66$. This consideration will produce the same density loss for all the cases, providing clearer PDF function and interpretations. Figure 4.11 shows the probability distribution of the density variation as a function of the temperature. It can be observed that at low temperatures ($T = 400$ K), the PDF shows that the most probable value is almost one, in other words, no reaction has started yet. At $T = 600$ K some reactions have already started but the PDF is still highly skewed to the right (which again means that many reactions have not taken place yet). When $T = 800$ K all the reactions have already started and the PDF resembles to a uniform distribution function. At $T = 1000$ K some reactions have already finished, and finally at 1400K almost all the reactions have finished reaching the final value of the ratio of densities imposed for the simulation. In addition, some PDFs at certain temperatures have also been plotted to better illustrate this evolution (Figure 4.12).

To sum up, we have used four different techniques (ANOVA, EET, Sobol Indices and FAST) to study the impact of each variable in the kinetic model used by Airbus (Equation 2.15). The four techniques have led to similar conclusions: the variable E has the highest impact in the equation, followed by F . The variables n and A have very low impact in the equation, which means that even though their value change, the shape of the decomposition curve will remain basically the same. This is a problem when performing a fitting because different sets of parameters can fit the same experimental data with good accuracy.

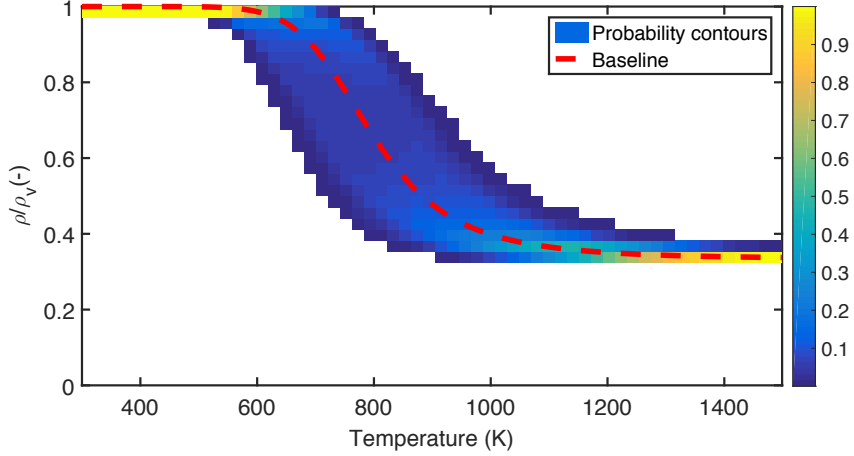


Figure 4.11: Probability distribution plot of density loss over temperature.

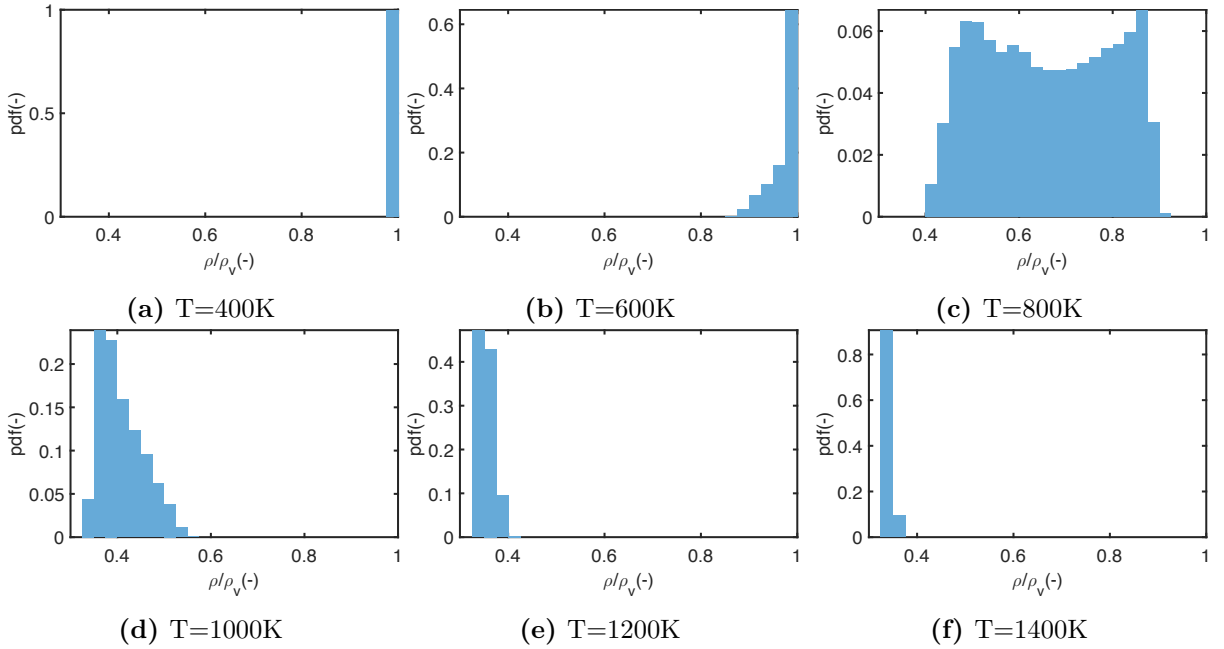


Figure 4.12: PDFs obtained for different temperatures. It can be seen that at low temperatures, $T = 400\text{ K}$, no reaction has started yet (the pdf is equal to 1 for $\rho/\rho_v = 1$), as the temperature increases, the pdf evolves to lower values of density ratios until $T = 1400\text{ K}$ where almost all the reactions have already finished

4.3 Results of TGA Curve Fitting

In this section, some capabilities of the FiTGA package will be presented as well as a case with experimental data. First of all, a basic validation case will be reported in order to show that the code is capable of recovering the parameters associated to a reaction. Secondly, a more complex validation, fitting two curves at different heating rate will be presented. Finally, a fitting of an experimental case will be used to show the capabilities of FiTGA to identify and separate the different overlapped reactions.

4.3.1 Validation case: 2-reaction simulated data

This is a validation case with simulated data generated with aleatory numbers using the kinetic model of PATO. Two reactions with different kinetic parameters have been considered. They are summarized in Table 4.1.

Table 4.1: Aleatory numbers for the two reactions

	Reaction 1	Reaction 2
<i>F</i>	0.12	0.21
<i>N</i>	0	0
<i>A</i>	10747	60747
<i>E</i>	53000	105000
<i>M</i>	2.8	2.2

The algorithm chosen to solve this case is the non linear least squares method. Figure 4.13 shows the results of the fitting process. It can be seen that the fitted curve, which is the red solid line, follows almost perfectly the simulated data.

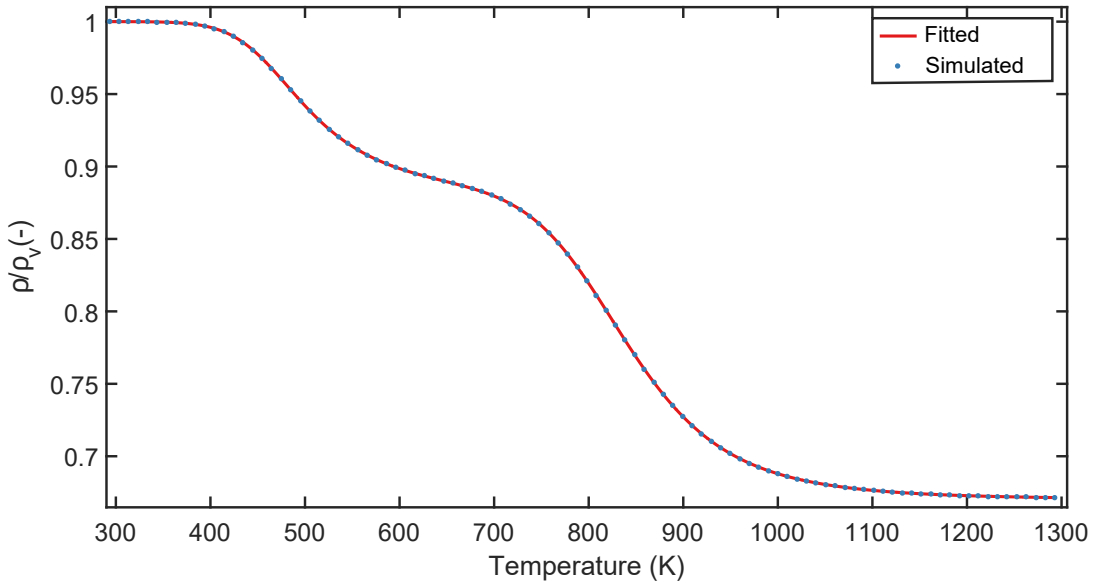


Figure 4.13: Fitting process results (red) for 2 Reaction with simulated data (blue). Great agreement is found.

Nevertheless, the most important part is to compare the triplets obtained in the fitting with the simulated data. In Table 4.2, one can observe that the parameters obtained for the two reactions are very close to the simulated data. Only the variable *A* presents some discrepancies. These discrepancies can be explained with the sensitivity study performed previously in which we determined that the variable *A* has very small influence in the results, thus changing its value may not change significantly the shape of the curve.

In addition, the package allows to separate the different reactions. Figure 4.14 shows this capability of the code. The red dotted line represents the TGA curve (left axis) and the solid lines the DTGA (right axis). It can be observed that the two peaks of the DTGA (solid red line)

Table 4.2: Comparison between fitted and simulated parameters. The maximum difference found is 1.29% for the variable A of the second reaction.

	F_1	E_1	N_1	M_1	A_1	F_2	E_2	N_2	M_2	A_2
Simulated	0.12	53000	0	2.8	10747	0.21	105000	0	2.2	60747
Fitted	0.12	52974	0	2.8	10669	0.21	104917	0	2.2	59964
Rel. Error (%)	0	0.05	0	0	0.73	0	0.08	0	0	1.29

define the points where the two reactions reach their maximum decomposition rate. The two contributions can be separated (blue and green curves), and it can be observed that there is a region where the two reactions are overlapped (dashed circle).

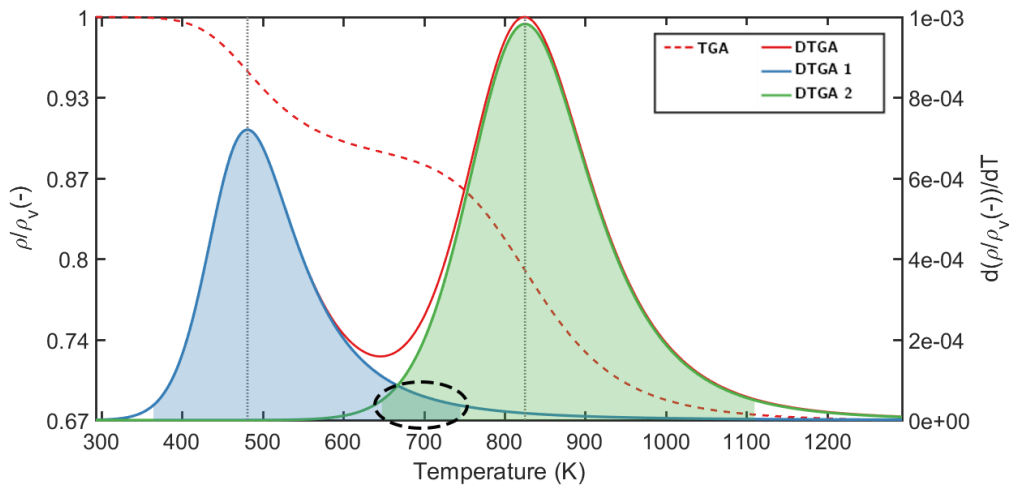


Figure 4.14: TGA and DTGA curves with different contributions. An overlapping area can be seen in the dashed circle.

4.3.2 Hybrid Genetic Algorithm test: two curves with different heating rates

This case is also performed with simulated data to demonstrate the capability of FiTGA to deal with multiple heating rates. This is essential to analyze TGA data and being able to predict thermal decomposition behavior accurately [28].

In this case, only a one-reaction case has been considered with two different heating rates ($\beta = 15 \text{ K} \cdot \text{min}^{-1}$ and $\beta = 45 \text{ K} \cdot \text{min}^{-1}$) and the HGA will be used to solve the minimization process using the kinetic model of PATO.

Figure 4.15 shows the results obtained in this case. It can be seen that the curve generated (solid line) using the obtained parameters fits almost perfectly the simulated data (circles) for both heating rates. Nevertheless, the values of fitted parameters do not correspond with the input data (Table 4.3): the error obtained for the variable A is about 30 %.

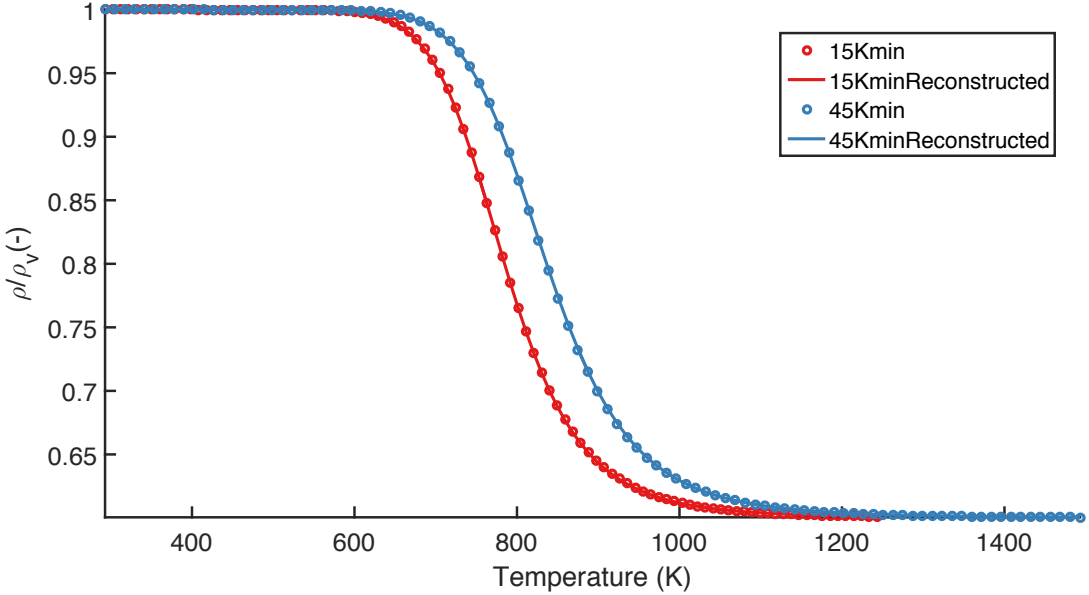


Figure 4.15: HGA results with two different heating rates. The two curves are perfectly fitted.

Table 4.3: Comparison between input and output data for the case of two different heating rates. The difference obtained for the variable A is approximately 30 %

	F_1	E_1	N_1	M_1	A_1
Simulated	0.4	105000	0	2.2	60747
Fitted	0.4	102949	0	2.15	42948
Rel. Error (%)	0	1.95	0	2.27	29.30

4.3.3 Four-reaction experimental data fitting

In this section, we present a fitting of experimental LCA data³ (TACOT). The four reaction mechanism used to fit the data is that described by Lachaud & Mansour [43].

Figure 4.16 shows both the experimental and the adjusted curves, it can be observed that the adjusted curve follows very precisely the experimental points. Only at the beginning there is an apparent increase of mass. This increase is due to the buoyancy effect and the low mass of the sample, and it can be considered negligible since no reaction has started yet at that point.

³These data were provided by Jean Lachaud from University of New Caledonia.

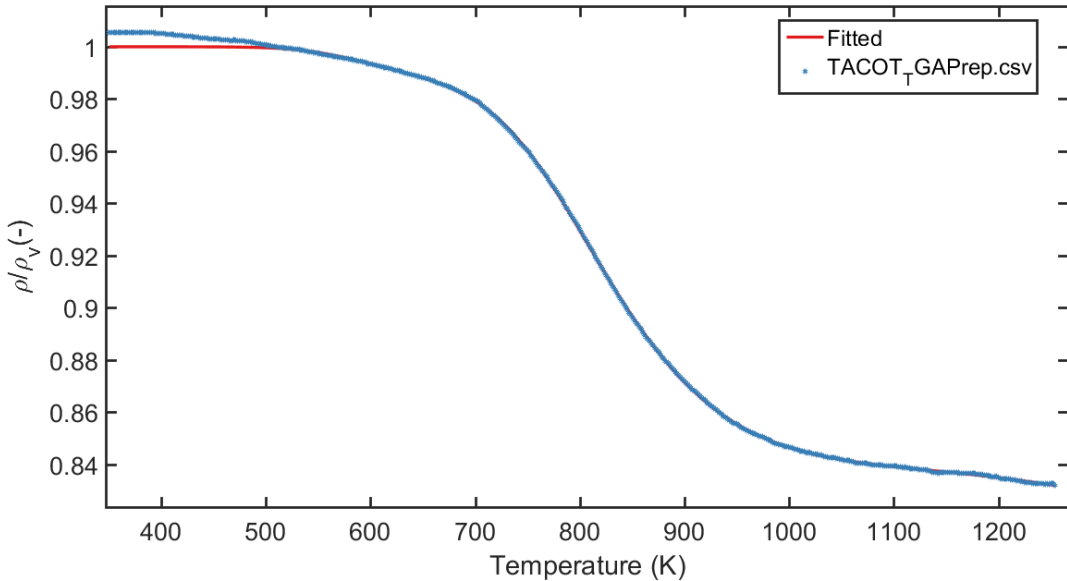


Figure 4.16: Comparison of density ratio evolution: In blue the experimental points, in red the adjusted curve.

Figure 4.17 shows the DTGA curve and the different contributions of each reaction to the total. It also shows the TGA curve in red dashed line. It can be observed that the final density ratio $\rho/\rho_v \approx 0.78$ is in good agreement with the experiments performed by B. Helber on the VKI Plasmatron [5].

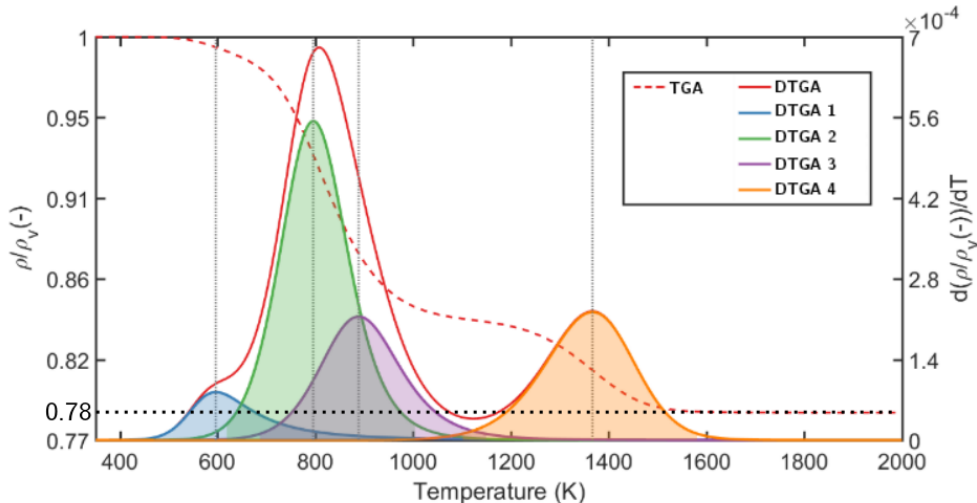


Figure 4.17: Decomposition of the reaction process. In red the totals (dashed line: TGA, solid line DTGA) and in the other colors the different contributions to the total DTGA.

In this case, the results obtained (Table 4.4) can be compared, in terms of orders of magnitude, with a first approach with simplified methods performed by Lachaud & Mansour [43] (Table 4.5). One can observe that the variables E , M and N have a good agreement. The temperature peaks have some agreement for reactions 2 and 3, but not for reactions 1 and 4. And the variables F and A do not agree.

Table 4.4: Arrhenius parameters and peak temperatures for the different reactions obtained with FiTGA.

	Reaction 1	Reaction 2	Reaction 3	Reaction 4
F	0.01	0.10	0.05	0.03
N	0	0	0	0
A	3×10^4	$3,91 \times 10^3$	2×10^3	$2,61 \times 10^4$
E	$7,74 \times 10^4$	$9,33 \times 10^4$	$9,93 \times 10^4$	$1,81 \times 10^5$
M	2.55	1.79	1.94	4.00
$T_{peak}(\text{K})$	595	790	890	1350

Table 4.5: Arrhenius parameters and peak temperatures obtained by Lachaud [43].

	Reaction 1	Reaction 2	Reaction 3	Reaction 4
F	0.01	0.24	0.03	0.06
N	0	0	0	0
A	$8,56 \times 10^3$	$8,56 \times 10^3$	$4,98 \times 10^8$	$4,98 \times 10^8$
E	$7,12 \times 10^4$	$7,12 \times 10^4$	$1,70 \times 10^5$	$1,70 \times 10^5$
M	3	3	3	3
$T_{peak}(\text{K})$	373	773	873	1073

5 Conclusions

In this thesis, two Thermal Analysis techniques, Differential Scanning Calorimetry (DSC) and Thermogravimetric Analysis (TGA), have been used for the characterization of the thermal decomposition of Lightweight Ceramic Ablators (LCA) used as Thermal Protection Systems in space exploration missions.

5.1 Conclusions on DSC

First, an experimental methodology for heat capacity determination of these ablative materials by DSC has been developed based on the standard Sapphire method (ISO 11357). This methodology includes initial baseline measurement, followed by calibration measurement with sapphire (used as reference material of well-known c_p), measurement of samples under study and, final validation of these experimental results with literature data.

- It has been shown that the heating rate and the sample mass are the two key variables when running these DSC tests, due to the low density of the LCAs. For these materials, it is suggested to run DSC tests at $40\text{ K} \cdot \text{min}^{-1}$ heating rate with 7,5 mg of sample.
- The sample preparation is another critical issue, due to the low density of these materials. Materials were powdered and compressed in the crucible in order to improve contact. A limitation of this procedure is that the effect of the microstructure cannot be studied.
- Results in good agreement with literature data have been obtained for samples (like graphite, preform, and resin char) with simple c_p curves, with no chemical reactions overlapping, confirming validity of this methodology.
- Improvements of this experimental methodology should however be developed for increasing repeatability.

5.2 Conclusions on TGA

Next, a software package (FiTGA) using MATLAB has been specifically developed for LCAs, capable of fitting TGA experimental data using a kinetic model for pyrolysis. As a result, the kinetic parameters of the different reactions involved in the thermal decomposition process of these materials can be obtained.

- The FiTGA package consists of three modules: preprocessing, fitting and post-processing.
- The preprocessing module allows the user to perform some preliminary data treatment, to define the material type, the kinetic model, or the optimization algorithm that will be used.

- The fitting module performs the appropriate calculations to obtain the kinetic parameters. It consists of two tasks: curve reconstruction (generation of a theoretical TGA curve according to an imposed model), and optimization of the parameters (iterative process to find the set of parameters associated to the chosen kinetic model that minimizes the difference between the reconstructed curve and the experimental data). Three different optimization algorithms have been implemented in FiTGA: a non-linear Least Squares Method (using a trust region approach), a Genetic Algorithm, and a Hybrid Genetic Algorithm that combines the benefits of the other two methods.
- The post-processing module is used to generate different files (plots and tables) for better results analysis.
- In addition, a sensitivity analysis was performed using four different approaches (ANOVA, EET, Sobol Indices and FAST) to study the impact of each variable in the kinetic model. Similar conclusions have been obtained in all cases: the activation energy E is the parameter with highest impact in the model, followed by the maximum decomposition F . In contrast, the pre-exponential factor A has lower impact on the model. This means that when changing the value of A , the shape of the decomposition curve will remain basically the same. This is a limitation since different values of this parameter can fit the same experimental data with good accuracy.
- Finally, different validation cases of the FiTGA package have been presented. It was demonstrated the capability of this code to deal with multiple heating rate decomposition curves, and to identify and separate several overlapped reactions occurring during pyrolysis. In general, good agreement has been found for all the kinetic parameters extracted with FiTGA, except for the pre-exponential factor A . This could be probably due to the small influence of this variable on the model, as shown by the sensitivity analysis.

5.3 Final Conclusions

- In conclusion, this thesis demonstrates that Simultaneous Thermal Analysis (STA) can be successfully used for the thermal characterization of a new generation of low density carbon/resin composite ablators.
- Differential Scanning Calorimetry in conjunction with Thermogravimetric Analysis can be used to provide useful parameters for future response modeling of these materials. Data such as the heat capacity that can be obtained from DSC experiments, and the kinetic decomposition parameters that can be extracted from TGA data, are required as inputs for high-fidelity modeling codes of the thermal response of ablative materials.
- STA can therefore be considered a promising technique for Aerospace Materials research.

6 Budget

The following tables present a breakdown of the different costs of this project. The personal costs has been calculated with the different grants that I have received during my time at the VKI: Erasmus internship grant for three months, Short Training Program grant from VKI for other three months and Education Ministry of Spain grant. Considering personal and measurement costs, the total cost of the project is 8172 €.

Table 6.1: Personal costs of the project

	Hours (h)	Cost (€)
Development of FiTGA	300	1500
STA measurements	60	300
Analysis of results	150	750
Report and conclusions	500	2500
TOTAL	5050	

Table 6.2: STA Measurements Costs

	Measurements	Cost (€)
Graphite	2	360
Preform	4	720
Resin	4	720
Asterm	4	720
TOTAL	3122	

Bibliography

- [1] Bernd Helber et al. “Material response characterization of a low-density carbon composite ablator in high-enthalpy plasma flows”. In: *J Mater Sci* 49.13 (Apr. 1, 2014), pages 4530–4543. URL: <http://link.springer.com/article/10.1007/s10853-014-8153-z> (visited on 12/03/2015).
- [2] Bernd Helber et al. “Space and Time-Resolved Emission Spectroscopy of Carbon Phenolic Ablation in Air and Nitrogen Plasmas”. In: *44th AIAA Thermophysics Conference*. American Institute of Aeronautics and Astronautics. URL: <http://arc.aiaa.org/doi/abs/10.2514/6.2013-2770> (visited on 12/03/2015).
- [3] Georges Duffa. *Ablative Thermal Protection Systems Modeling*. American institute of aeronautics and astronautics, 2013. 431 pages.
- [4] Bernd Helber et al. “Ablation of Carbon Preform In the VKI Plasmatron”. In: *43rd AIAA Thermophysics Conference*. American Institute of Aeronautics and Astronautics. URL: <http://arc.aiaa.org/doi/abs/10.2514/6.2012-2876> (visited on 12/03/2015).
- [5] Bernd Helber. *Material response characterization of low-density ablators in atmospheric entry plasmas*. Rhode-St-Genese, belgium von Karman Institute 2016, 2016. 225 pages.
- [6] B. LAUB and E. Venkatapathy. “Thermal Protection System Technology and Facility Needs for Demanding Future Planetary Missions”. In: (Oct. 6, 2013).
- [7] Kimberly A. Trick and Tony E. Saliba. “Mechanisms of the pyrolysis of phenolic resin in a carbon/phenolic composite”. In: *Carbon* 33.11 (1995), pages 1509–1515. URL: <http://www.sciencedirect.com/science/article/pii/000862239500092R> (visited on 12/03/2015).
- [8] Brody K. Bessire, Sridhar A. Lahankar, and Timothy K. Minton. “Pyrolysis of Phenolic Impregnated Carbon Ablator (PICA)”. In: *ACS Appl. Mater. Interfaces* 7.3 (Jan. 28, 2015), pages 1383–1395. URL: <http://dx.doi.org/10.1021/am507816f> (visited on 12/03/2015).
- [9] Jean Lachaud and Nagi Mansour. “Porous-material Analysis Toolbox based on OpenFOAM-extend and Applications”. In: *44th AIAA Thermophysics Conference*. American Institute of Aeronautics and Astronautics. URL: <http://arc.aiaa.org/doi/abs/10.2514/6.2013-2767> (visited on 12/08/2015).
- [10] Hsi-Wu Wong et al. “Quantitative determination of species production from the pyrolysis of the Phenolic Impregnated Carbon Ablator (PICA)”. In: *53rd AIAA Aerospace Sciences Meeting*. American Institute of Aeronautics and Astronautics. URL: <http://arc.aiaa.org/doi/abs/10.2514/6.2015-1447> (visited on 12/08/2015).

- [11] Hsi-Wu Wong et al. “Quantitative determination of species production from phenol-formaldehyde resin pyrolysis”. In: *Polymer Degradation and Stability* 112 (Feb. 2015), pages 122–131. URL: <http://www.sciencedirect.com/science/article/pii/S0141391014004534> (visited on 12/08/2015).
- [12] L. Torre, J. M. Kenny, and A. M. Maffezzoli. “Degradation behaviour of a composite material for thermal protection systems Part I Experimental characterization”. In: *Journal of Materials Science* 33.12 (June 1998), pages 3137–3143. URL: <http://link.springer.com/article/10.1023/A%3A1004399923891> (visited on 12/03/2015).
- [13] L. Torre, J. M. Kenny, and A. M. Maffezzoli. “Degradation behaviour of a composite material for thermal protection systems Part II Process simulation”. In: *Journal of Materials Science* 33.12 (June 1998), pages 3145–3149. URL: <http://link.springer.com/article/10.1023/A%3A1004352007961> (visited on 12/03/2015).
- [14] L. Torre et al. “Degradation behaviour of a composite material for thermal protection systems Part III Char characterization”. In: *Journal of Materials Science* 35.18 (Sept. 2000), pages 4563–4566. URL: <http://link.springer.com/article/10.1023/A%3A1004828923152> (visited on 12/03/2015).
- [15] Gregory Pinaud. “Thermo-Chemical and Mechanical Coupled Analysis of Swelling, Charring and Ablative Materials for Re-Entry Applications”. In: *Ablation Workshop* (Feb. 29, 2012). URL: <http://uknowledge.uky.edu/ablation/2012/Coupling/1>.
- [16] Bernd Helber et al. “Experimental investigation of ablation and pyrolysis processes of carbon-phenolic ablators in atmospheric entry plasmas”. In: *International Journal of Heat and Mass Transfer* 100 (Sept. 2016), pages 810–824. URL: <http://www.sciencedirect.com/science/article/pii/S0017931015310243> (visited on 06/06/2016).
- [17] Gaurav Agarwal and Brian Lattimer. “Method for measuring the standard heat of decomposition of materials”. In: *Thermochimica Acta* 545 (Oct. 10, 2012), pages 34–47. URL: <http://www.sciencedirect.com/science/article/pii/S0040603112003139> (visited on 09/30/2015).
- [18] Jing Li and Stanislav I. Stolarov. “Measurement of kinetics and thermodynamics of the thermal degradation for charring polymers”. In: *Polymer Degradation and Stability*. Special Issue Based on the 14th European meeting on Fire Retardancy and Protection of Materials, held at Ecole Nationale Supérieure de Chimie de Lille (U. Lille-1), France, July 2013 106 (Aug. 2014), pages 2–15. URL: <http://www.sciencedirect.com/science/article/pii/S0141391013003108> (visited on 09/16/2015).
- [19] M. M. Hirschler. “Thermal decomposition (STA and DSC) of PVC compounds under a variety of atmospheres and heating rates”. In: *European Polymer Journal* 22.2 (1986), pages 153–160. URL: <http://www.sciencedirect.com/science/article/pii/0014305786901114> (visited on 09/30/2015).
- [20] W. M. Groenewoud. *Characterisation of Polymers by Thermal Analysis*. Elsevier, May 21, 2001. 407 pages.

- [21] Francisco Vilaplana Domingo, Amparo Ribes Greus, and Laura Contat Rodrigo. *Thermal Characterisation of Polymeric Materials*. Departamento de Maquinas y Motores Termicos, Escuela Tecnica Superior de Ingenieria del Diseno, Universidad Politecnica de Valencia, 2008. 94 pages.
- [22] Bernhard Wunderlich. *Thermal Analysis of Polymeric Materials*. Springer Science & Business Media, Apr. 4, 2005. 918 pages.
- [23] Edith Turi. *Thermal Characterization of Polymeric Materials*. Elsevier, Dec. 2, 2012. 987 pages.
- [24] TA Instruments. “Thermal Analysis Review: Modulated DSC theory”. In: () .
- [25] Mettler-Toledo. “Thermal Analysis UserCom 29”. In: (). URL: http://us.mt.com/content/us/en/home/supportive_content/usercom/TA_UserCom29.html (visited on 07/07/2016).
- [26] Sergey Vyazovkin. *Isoconversional Kinetics of Thermally Stimulated Processes*. Cham: Springer International Publishing, 2015. URL: <http://link.springer.com/10.1007/978-3-319-14175-6> (visited on 05/30/2016).
- [27] B. Saha, P. Karthik Reddy, and A. K. Ghoshal. “Hybrid genetic algorithm to find the best model and the globally optimized overall kinetics parameters for thermal decomposition of plastics”. In: *Chemical Engineering Journal* 138.1 (May 1, 2008), pages 20–29. URL: <http://www.sciencedirect.com/science/article/pii/S1385894707003580> (visited on 05/26/2016).
- [28] M. E. Brown et al. “Computational aspects of kinetic analysis: Part A: The ICTAC kinetics project-data, methods and results”. In: *Thermochimica Acta* 355.1 (July 31, 2000), pages 125–143. URL: <http://www.sciencedirect.com/science/article/pii/S0040603100004433> (visited on 05/30/2016).
- [29] Marek Maciejewski. “Computational aspects of kinetic analysis.: Part B: The ICTAC Kinetics Project — the decomposition kinetics of calcium carbonate revisited, or some tips on survival in the kinetic minefield”. In: *Thermochimica Acta* 355.1 (July 31, 2000), pages 145–154. URL: <http://www.sciencedirect.com/science/article/pii/S0040603100004445> (visited on 05/30/2016).
- [30] Sergey Vyazovkin. “Computational aspects of kinetic analysis.: Part C. The ICTAC Kinetics Project — the light at the end of the tunnel?” In: *Thermochimica Acta* 355.1 (July 31, 2000), pages 155–163. URL: <http://www.sciencedirect.com/science/article/pii/S0040603100004457> (visited on 05/30/2016).
- [31] Alan K Burnham. “Computational aspects of kinetic analysis.: Part D: The ICTAC kinetics project — multi-thermal-history model-fitting methods and their relation to isoconversional methods”. In: *Thermochimica Acta* 355.1 (July 31, 2000), pages 165–170. URL: <http://www.sciencedirect.com/science/article/pii/S0040603100004469> (visited on 05/30/2016).

- [32] B. Roduit. “Computational aspects of kinetic analysis.: Part E: The ICTAC Kinetics Project—numerical techniques and kinetics of solid state processes”. In: *Thermochimica Acta* 355.1 (July 31, 2000), pages 171–180. URL: <http://www.sciencedirect.com/science/article/pii/S0040603100004470> (visited on 05/30/2016).
- [33] Jean Lachaud and Nagi N. Mansour. “Porous-Material Analysis Toolbox Based on OpenFOAM and Applications”. In: *Journal of Thermophysics and Heat Transfer* 28.2 (2014), pages 191–202. URL: <http://dx.doi.org/10.2514/1.T4262> (visited on 01/25/2016).
- [34] Jean Lachaud et al. “Detailed chemical equilibrium model for porous ablative materials”. In: *International Journal of Heat and Mass Transfer* 90 (Nov. 2015), pages 1034–1045. URL: <http://www.sciencedirect.com/science/article/pii/S0017931015006006> (visited on 09/16/2015).
- [35] J. R. Dormand and P. J. Prince. “A family of embedded Runge-Kutta formulae”. In: *Journal of Computational and Applied Mathematics* 6.1 (Mar. 1, 1980), pages 19–26. URL: <http://www.sciencedirect.com/science/article/pii/0771050X80900133>.
- [36] Jorge Nocedal and Stephen Wright. *Numerical Optimization*. Springer Science & Business Media, Dec. 11, 2006. 686 pages.
- [37] David Edward Goldberg. *Genetic Algorithms in Search, Optimization, and Machine Learning*. Addison-Wesley Publishing Company, Jan. 1, 1989. 436 pages.
- [38] ISO 11357-4:2014 - Plastics – Differential scanning calorimetry (DSC) – Part 4: Determination of specific heat capacity. ISO. 2014. URL: http://www.iso.org/iso/catalogue_detail.htm?csnumber=65087 (visited on 06/28/2016).
- [39] Mettler-Toledo. “Thermal Analysis UserCom 11”. In: (). URL: http://us.mt.com/content/us/en/home/supportive_content/usercom/TA_UserCom11.html (visited on 07/07/2016).
- [40] Mettler-Toledo. “Thermal Analysis UserCom 7 - Measuring specific heat capacity”. In: (1998). URL: http://us.mt.com/content/us/en/home/supportive_content/usercom/TA_UserCom7.html (visited on 06/07/2016).
- [41] Hugh O. Pierson. *Handbook of Carbon, Graphite, Diamonds and Fullerenes: Processing, Properties and Applications*. William Andrew, Dec. 2, 2012. 420 pages.
- [42] Soo-Jin Park. *Carbon Fibers*. Springer, Oct. 8, 2014. 337 pages.
- [43] Nagi Mansour et al. “High-Fidelity Charring Ablator Thermal Response Model”. In: *42nd AIAA Thermophysics Conference*. AIAA: American Institute of Aeronautics and Astronautics, June 30, 2011. URL: <http://arc.aiaa.org/doi/abs/10.2514/6.2011-3124> (visited on 04/20/2016).
- [44] Clark Evans. *YAML Ain't Markup Language*. May 1, 2016. URL: <http://www.yaml.org/start.html>.
- [45] A. Saltelli et al. *Global Sensitivity Analysis: The Primer*. John Wiley & Sons, Feb. 28, 2008. 307 pages.

- [46] Francesca Pianosi, Fanny Sarrazin, and Thorsten Wagener. “A Matlab toolbox for Global Sensitivity Analysis”. In: *Environmental Modelling & Software* 70 (Aug. 2015), pages 80–85. URL: <http://www.sciencedirect.com/science/article/pii/S1364815215001188> (visited on 01/08/2016).
- [47] S. Whitaker. *The Method of Volume Averaging*. Springer Science & Business Media, Nov. 30, 1998. 242 pages.
- [48] R. C. Rossi and W. C. Wong. “Availability of Aerospace Rayon for SRM Nozzle Insulators”. In: (), page 7. (Visited on 06/20/2016).
- [49] L. G. St leger J. E. Pavlosky. “Apollo experience report: Thermal protection subsystem”. In: (1974).
- [50] J. E. Daw. “Measurement of Specific Heat Capacity Using Differential Scanning Calorimeter”. In: () .
- [51] Colomba Di Blasi. “Modeling and simulation of combustion processes of charring and non-charring solid fuels”. In: *Progress in Energy and Combustion Science* 19.1 (1993), pages 71–104. URL: <http://www.sciencedirect.com/science/article/pii/0360128593900227> (visited on 09/30/2015).
- [52] M. J. O’Neill. “Measurement of Specific Heat Functions by Differential Scanning Calorimetry.” In: *Anal. Chem.* 38.10 (Sept. 1, 1966), pages 1331–1336. URL: <http://dx.doi.org/10.1021/ac60242a011> (visited on 09/29/2015).
- [53] E. W. Lemmon and R. T. Jacobsen. “Viscosity and Thermal Conductivity Equations for Nitrogen, Oxygen, Argon, and Air”. In: *International Journal of Thermophysics* 25.1 (Jan. 2004), pages 21–69. URL: <http://link.springer.com/article/10.1023/B%3AIJOT.0000022327.04529.f3> (visited on 12/03/2015).
- [54] R. E. Taylor and H. Groot. *Thermophysical Properties of POCO Graphite*. July 1978.
- [55] Georg Widmann. “UserCom 13 - Interpreting TGA Curves”. In: *Mettler Toledo* (2001).
- [56] Hrvoje Jasak, Aleksandar Jemcov, and Z Tukovic. “OpenFOAM: A C++ library for complex physics simulations”. In: *International Workshop on Coupled Methods in Numerical Dynamics*. Dubrovnik, Croatia, 2007. URL: <http://powerlab.fsb.hr/ped/kturbo/openfoam/papers/CMND2007.pdf>.
- [57] Chris Greenshields. *OpenFOAM User Guide: CFD Direct, Architects of OpenFOAM*. CFD Direct. URL: <http://cf.direct/openfoam/user-guide/> (visited on 11/30/2015).
- [58] James B. Scoggins and Thierry E. Magin. “Gibbs function continuation for linearly constrained multiphase equilibria”. In: *Combustion and Flame* 162.12 (Dec. 2015), pages 4514–4522. URL: <http://www.sciencedirect.com/science/article/pii/S0010218015003016> (visited on 06/07/2016).
- [59] DSC - Compare prices and order services - Science Exchange. URL: <https://www.scienceexchange.com/services/dsc> (visited on 07/17/2016).

- [60] Amos Gilat. *MATLAB: An Introduction with Applications*, 5th Edition. Wiley Global Education, Jan. 8, 2014. 418 pages.
- [61] T. Coleman and Y. Li. “An Interior Trust Region Approach for Nonlinear Minimization Subject to Bounds”. In: *SIAM J. Optim.* 6.2 (May 1, 1996), pages 418–445. URL: <http://pubs.siam.org/doi/abs/10.1137/0806023> (visited on 04/04/2016).
- [62] D. Thierens. “Adaptive mutation rate control schemes in genetic algorithms”. In: *Proceedings of the 2002 Congress on Evolutionary Computation, 2002. CEC '02*. Proceedings of the 2002 Congress on Evolutionary Computation, 2002. CEC '02. Volume 1. May 2002, pages 980–985.
- [63] Haiyun Jiang et al. “The pyrolysis mechanism of phenol formaldehyde resin”. In: *Polymer Degradation and Stability* 97.8 (Aug. 2012), pages 1527–1533. URL: <http://www.sciencedirect.com/science/article/pii/S0141391012001644> (visited on 11/22/2015).
- [64] Hsi-Wu Wong et al. “Measurement of pyrolysis products from phenolic polymer thermal decomposition”. In: *52nd Aerospace Sciences Meeting*. American Institute of Aeronautics and Astronautics. URL: <http://arc.aiaa.org/doi/abs/10.2514/6.2014-1388> (visited on 12/03/2015).
- [65] E. SMITH et al. “Thermal/ablation model of low density cork phenolic for the Titan IVStage I engine thermal protection system”. In: *27th Thermophysics Conference*. American Institute of Aeronautics and Astronautics. URL: <http://arc.aiaa.org/doi/abs/10.2514/6.1992-2905> (visited on 12/03/2015).
- [66] Francesco Panerai et al. “Surface temperature jump beyond active oxidation of carbon/silicon carbide composites in extreme aerothermal conditions”. In: *Carbon* 71 (May 2014), pages 102–119. URL: <http://www.sciencedirect.com/science/article/pii/S0008622314000530> (visited on 12/03/2015).
- [67] K. A. Trick, T. E. Saliba, and S. S. Sandhu. “A kinetic model of the pyrolysis of phenolic resin in a carbon/phenolic composite”. In: *Carbon* 35.3 (1997), pages 393–401. URL: <http://www.sciencedirect.com/science/article/pii/S0008622397896108> (visited on 12/03/2015).
- [68] Komandoor Elayavalli Achyuthan et al. “Supramolecular Self-Assembled Chaos: Polyphenolic Lignins Barrier to Cost-Effective Lignocellulosic Biofuels”. In: *Molecules* 15.12 (Nov. 29, 2010), pages 8641–8688. URL: <http://www.mdpi.com/1420-3049/15/12/8641> (visited on 12/20/2015).
- [69] A. F. Roberts. “The heat of reaction during the pyrolysis of wood”. In: *Combustion and Flame* 17.1 (Aug. 1, 1971), pages 79–86. URL: <http://www.sciencedirect.com/science/article/pii/S0010218071801414> (visited on 12/03/2015).
- [70] J. Rath et al. “Heat of wood pyrolysis”. In: *Fuel* 82.1 (Jan. 2003), pages 81–91. URL: <http://www.sciencedirect.com/science/article/pii/S0016236102001382> (visited on 12/03/2015).

- [71] William S. L. Mok and Michael J. Antal. "Effects of pressure on biomass pyrolysis. II. Heats of reaction of cellulose pyrolysis". In: *Thermochimica Acta* 68.2 (Oct. 1, 1983), pages 165–186. URL: <http://www.sciencedirect.com/science/article/pii/0040603183802226> (visited on 12/03/2015).

A Simulation tools: *OpenFOAM* & *PATO*

A.1 *OpenFOAM*

*OpenFOAM*¹ is a C++ library maintained and distributed by The *OpenFOAM* Foundation under GNU GPL licence. The code is released as free and open source. The applications created with *OpenFOAM* are designed to solve a specific problem or task. Many different applications are already available in the distribution including solvers for different types of flows, meshing tools, postprocessing tools, etc. The name of the application usually gives an idea of the function (*simpleFoam* steady state solver for incompressible turbulent flow which uses the SIMPLE scheme for pressure link). In addition, tutorials (test cases) are provided for each application and they are usually used as a base for other cases.

Figure A.1 shows an overview of the structure of *OpenFOAM*. It can be observed that there are three different modules, which follows the typical structure of any CFD software:

- Pre-processing: *OpenFOAM* includes different utilities to mesh geometries (*blockMesh*, *snappyHexMesh*), to convert meshes generated with other software to the format used by OpenFOAM (*fluentMeshToFoam*, *gambitToFoam*, *star3ToFoam*, etc) or to manipulate them (*rotateMesh*, *transformPoints*, *mergeMeshes*, etc).
- Solving: there are many implemented solvers which are able to compute different types of flow. Laplacian equation solvers (*laplacianFoam*), incompressible and turbulent flows (*simpleFoam*), multiphase flows (*interFoam*), etc. Furthermore, users can create their own applications for specific purposes.
- Post-processing: there are many different ways to post process the solution. *ParaView* is a powerful visualization software ready to be used with *OpenFOAM*. Alternatives such as Matlab or *GNUPlot* are also very popular, especially when using probes (which track the value of a determined variable in a certain point).

The main difference between *OpenFOAM* and other CFD packages is the structure of the cases. *OpenFOAM* organizes the cases in folders. Each folder has some files which perform a specific function. This approach is very logical and allows the user to modify different parameters of a particular case (mesh, boundaries, solver, time step, etc) just by modifying a text file. Moreover, some parameters of the simulation can be modified at execution time (time step, Courant number, etc). It also simplifies the automation (i.e. create a script able to generate cases with different conditions automatically).

¹Since *OpenFOAM* is a well known software, only a small introduction is presented here. For more information: <http://www.openfoam.org/> and Jasak PhD thesis [56]

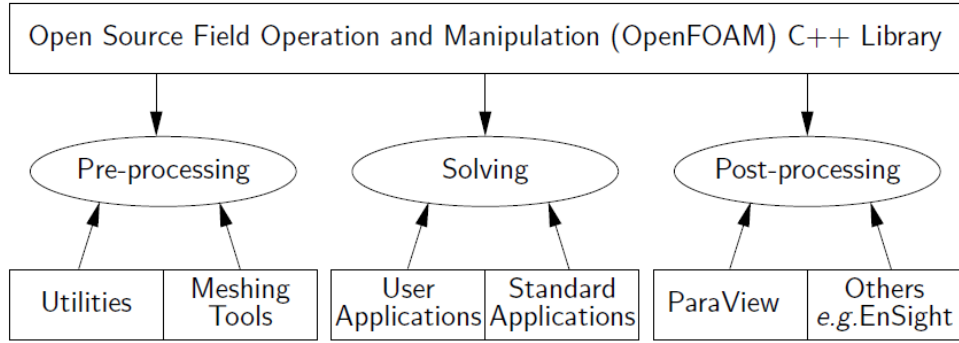


Figure A.1: Overview of *OpenFOAM* structure [57]

An *OpenFOAM* case usually has the following structure (Figure A.2), but it can change depending on the solver:

```

OpenFoamCase ..... Name of the main folder
└── 0 ..... contains the information of the initial conditions of the problem (pressure, temperature, velocity, etc)
└── Constant ..... Constants for material, BC and Mesh
    └── polyMesh ..... Folder that contains information of the mesh.
    └── transportProperties ..... in this file the physical properties are specified (viscosity, difusivity, conductivity, etc).
└── System ..... Schemes, control parameters, etc
    └── fvSchemes ..... Information about the numerical schemes for each operator.
    └── fvSolution ..... Solvers, tolerances and algorithms are specified in this file.
    └── controlDict ..... Information about time steps, writing data on files, starting and ending time is given here.

```

Figure A.2: Typical structure of folders of a *OpenFoam* case

Another important feature of *OpenFOAM* is that the way equations are implemented on solvers is similar to the mathematical writing. For example, the equation:

$$\frac{\partial \rho U}{\partial t} + \nabla \cdot \phi U - \nabla \cdot \mu \nabla U = -\nabla p \quad (\text{A.1})$$

Is represented by:

Listing A.1: Equation-like style of *OpenFOAM*

```

1 solve
2 (
3     fvm::ddt(rho, U)
4     + fvm::div(phi, U)
5     - fvm::laplacian(mu, U)
6     ==
7     - fvc::grad(p)
8 );

```

A.2 *PATO*

Porous material Analysis Toolbox based on OpenFOAM (PATO) [33] is an *OpenFOAM* library developed by Lachaud and Mansour as an analysis tool for research of porous media. *PATO* can be defined as a high fidelity ablation model solver[9]. This solver implements empirical relations based on volume-averaged equations for mass, momentum and energy. *PATO* is being specifically designed for ablative materials at high temperature (such as reentry flows) but it can be used in other applications.

The current release of *PATO*² is composed of two modules: *PAM* and *COACO*.

- *PAM* is applied to perform global analyses of a full ablative material from the macroscopic point of view, in other words, it applies volume averaged equations to calculate the different properties [47].
- *COACO* is used to study specific fundamental aspects from a microscopic point of view, for example, the detailed oxidation of carbon fibers.

PATO solves the equations sequentially. In other words, it is still not possible to use more than one processor to compute. Nevertheless, sequentially computation has some benefits in this case: equations can be added or modified without affecting the system and, several numerical schemes can be tested at execution time (which is an inherited characteristic from *OpenFOAM*).

In order to compute the chemistry and transport properties, *Mutation++* is used as a third party library. *Mutation++* is a opensource *C++* library developed at the VKI by Scoggins[58]. It is used to compute thermodynamic properties, transport properties in multicomponent systems, finite rate chemistry in thermal nonequilibrium, etc. It is specifically designed for hypersonics and Computational Fluid Dynamics, but it can be used in other fields.

Concerning the verification of *PAM*, it was decided to propose different test cases. This tests have been increased in complexity during years, starting with a 1D problem with chemistry, to a complete 3D problem with chemistry, surface recession, orthotropic material, etc [9].

Since the solver that is going to be used to perform the simulations is *PAM*, an overview of the structure of a test case is given in Figure A.3. It can be noted that the structure of a *PATO* case resembles to a normal *OpenFOAM* case (Figure A.2). Some folders are rearranged in a different way, and more files are added to consider the material, the chemistry and different properties.

²A fully detailed description of these solvers can be found in the paper by Jean Lachaud et al. [9]

```

AblationTestCase_X ..... Name of the main folder
  0 ..... Initial conditions
    ablaMat ..... Contains files for initial conditons (may vary)
      N2 & O2 ..... Initial composition of gas
      P ..... Initial volume averaged gas pressure
      rho_s ..... Initial density of the solid
      T ..... Initial temperature of the gas
      Ta ..... Initial volume-averaged temperature
      XsiDefault ..... Advancement of the reaction
  Constant ..... Constants for material, BC and Mesh
    ablaMat
      polyMesh..... Contains the mesh
      char ..... Tabulated properties of the char
      constantProperties ..... Universal constants and coefficients
      gasProperties ..... Table for gas properties
      virgin..... Tabulated properties of the virgin material
      environmentProperties ..... External properties
      boundaryConditions
    regionProperties ..... Defines type of material (solid, liquid, gas)
    setCase ..... Specifies the problem (type of boundaries and chemistry)
  Plots ..... Plots of the results
  System ..... Schemes, control parameters, etc
    ablaMat
      fvSchemes ..... Specifies the schemes
      fvSolution ..... Defines the methods used to solve each equation
      sampleDict ..... Defines probes positions
    controlDict ..... Specifies time parameters and writting controls

```

Figure A.3: Main structure of folders and files of a PAM tutorial.

B FiTGA User's Guide

In this Appendix, a summary of the FiTGA User's Guide is attached. The parts of this guide related with the models, the numerical methods and the implementation have been suppressed since they have been already explained in the main body of this thesis.



Universidad Politécnica de Valencia
ESCUELA TÉCNICA SUPERIOR DE INGENIERÍA DEL DISEÑO

von Kármán Institute for Fluid Dynamics
AERONAUTICS AND AEROSPACE DEPARTMENT



FiTGA User's Guide

Torres Herrador, Francisco José

Supervisor VKI:
Thierry Magin

Advisors VKI:
Vincent Leroy
Bernd Helber

Supervisor UPV:
Laura Contat Rodrigo

July 18, 2016

Contents

Contents	I
Nomenclature	II
1 Introduction	1
2 Installation	3
2.1 Matlab	3
2.2 Octave	3
2.3 Directory Structure	4
3 Tutorials	5
3.1 Implementing a new kinetic model: Airbus	5
3.2 Managing Materials	5
3.3 Managing Experimental Files Format	6
3.4 TGA Curve simulation	6
3.4.1 Simulate TGA data using input files	6
3.4.2 Simulate TGA data using GUI	7
3.5 Preprocessing of TGA experimental data	8
3.5.1 Preprocessing using input files	8
3.5.2 Preprocessing using GUI	9
3.6 Four law fitting of experimental data - <i>TACOT</i>	10
3.7 Adjusting two simulated curves at the same time	13
4 Cheating Sheet	14

Nomenclature

χ_i	Advancement of the reaction i -th [—].
ρ	Density [$\text{kg} \cdot \text{m}^{-3}$].
ρ_c	Density of the charred material [$\text{kg} \cdot \text{m}^{-3}$].
ρ_v	Density of the virgin material [$\text{kg} \cdot \text{m}^{-3}$].
$\rho_{t=0}$	Density at the beginning of the analysis [kg].
A	Pre-exponential factor [—].
E	Activation Energy [$\text{J} \cdot \text{mol}^{-1}$].
i	Subindex to point the i th Arrhenius Law.
m	Arrhenius parameter.
N	Number of experimental points.
n	Arrhenius parameter.
$nReactions$	Number of chemical reactions.
R	Universal gas constant [$8,31 \text{ J} \cdot \text{K}^{-1} \cdot \text{mol}^{-1}$].
T	Temperature [K].
RT	Room temperature.

1 Introduction

Thermogravimetric Analysis (TGA) is a technique in which the mass (or density¹) of a sample is measured as a function of a controlled temperature program. This experimental procedure will produce the so called thermograms (graphical representations of mass against temperature) which usually have a sigmoidal shape with different steps. These steps represent the weight loss produced due to volatile components which are generated in the different chemical (or physical) reactions that take place when the temperature increases (such as pyrolysis, combustion, evaporation, etc). The degradation process is usually complex and different models are used for different materials. These models are usually of the form:

$$\frac{d\chi_i}{dt} = A_i f(\chi) \exp\left(\frac{-E_i}{RT(t)}\right) \quad (1.1)$$

Where χ_i is the advancement of the reaction $i - th$. This parameter is related with the state of the reaction, in other words, when $\chi_i = 0$ the corresponding reaction has not started yet, when $\chi_i = 1$ the reaction has finished. At the same time, this parameter χ_i can be related with the density loss of the sample with a relation of the type:

$$\rho(t) = \rho_{t=0} (1 - \sum_i F_i \chi_i) \quad (1.2)$$

F_i represents the total density loss associated to the reaction $i - th$.

TGA experiments need to be processed in such a way that the kinetic parameters associated with each reaction are recovered. There are different ways to obtain them depending on the model used, but they usually rely on simplifications[1] or on commercial software. In addition, the models that are currently used in aerospace research are not available (yet) in commercial codes.

The main objective of this package is to provide an open-source environment to analyze TGA data for aerospace research. However, the implementation has been done in such a way that a user can implement and use new models easily. This package has been developed on Matlab^{2,3} since it offers the user a friendly programming environment, it has many built-in functions and it can be run in different OS.

¹In many cases volume is considered as constant during a TGA experiment, which makes a straightforward equivalence between mass and density. This is the case for this code, therefore from now on density will be the variable used.

²For those users not familiar with Matlab or Octave, the book of Gilat is a good recommendation.[2]

³Even it is commercial software, Matlab is usually available in research institutes and universities. In addition, this code is also compatible with GNU Octave (with some limitations).

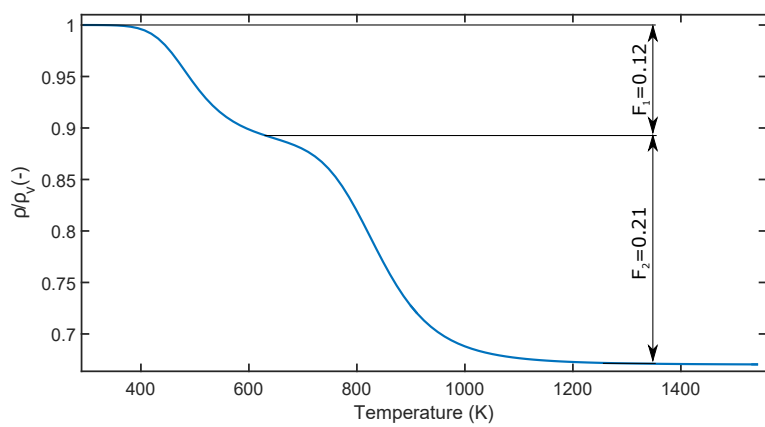


Figure 1.1: Simulated thermogram with arbitrary data. Two different reactions are observed with their their associated density loss.

2 Installation

This package can be run both in Matlab and Octave. Nevertheless, there are some differences that need a word of explanation.

2.1 Matlab

Matlab¹ works with the so called "search path". This means that for a function to be executed, it has to be in "the path". To add the needed folders to the path, the easiest way is to execute the function *setpathTGA* located in the main folder. From this moment, it is possible to call any of the functions contained in this folder from any other folder.

This action has to be done every time that Matlab is opened. However, these folders can be added to the path permanently following going to **Home** **Set Path** **Add Folder with Subfolders** ... **Functions**. Where the **...** represents the navigation path until the folder **Functions**. Having it highlighted, it is just needed to press **select folder** to finish.

2.2 Octave

In order to run this code on Octave², the following packages have to be installed (see Listing 2.1). This can also be done running the script **installOctavePackages**.

Listing 2.1: Commands to install extra packages needed.

```
1 pkg lst
2 pkg install --forge struct --auto;
3 pkg install --forge odepkg --auto;
4 pkg install --forge general --auto;
5 pkg install --forge optim --auto;
6 pkg install --forge io --auto;
7 pkg install --forge miscellaneous --auto;
```

After that, it is needed to add the folder **Functions** to the path³. In order to do this, the function *setpathTGA* located in the main folder needs to be executed.

¹The version used for this guide is Matlab 2015a.

²The version used for this guide is Octave 4.0.0.

³Both Matlab and Octave use the apostrophe when typing strings ('This is a string').

2.3 Directory Structure

```
FitGA
└── Documentation
└── Functions ..... Root folder for all the code of FitGA
    ├── catstruct..... Third party function to concatenate structures
    ├── Materials..... Reads material properties
    ├── Models ..... Reads decomposition models
    ├── struct2csv ..... Third party function to print Matlab structures in csv files
    └── YAMLMatlab_0.4.3 ..... Third party package to read YAML files in Matlab
└── Tutorials ..... Root directory for tutorials
    ├── CurveSimulation..... Generate simulated TGA data
    ├── 1Law ..... One-law fitting using simulated data
    ├── TACOT ..... Adjusting experimental data to a 4 reaction model
    └── 2CurvesFitting ..... Adjust two files at the same time
```

Figure 2.1: Main structure of folders and files of a FitGA

3 Tutorials

This section is intended to give an overview of the different capabilities of the code. Each of the tutorials covers a basic task (from implementing a new model, simulating TGA data, preprocessing experimental data, etc).

3.1 Implementing a new kinetic model: Airbus

In order to implement a new model, two files need to be created: one that specifies the parameters and the other one which defines the model. The name of the model should be in capital letters, for unambiguous identification of the function.

The parameter file should then be named as: *MODEL.yam* and its structure is shown in Listing 3.1.

Listing 3.1: Structure of paramAIRBUS.yam

```
1 [F, n, A, E]
```

In order to generate the file that defines the differential equation of the model, it is recommended to create a copy of an existing one and modify only the name of the file, name of the function and the differential equation. In the code, there are some lines that calculate the value of T in each iteration of the Runge-Kutta using linear interpolation. This is due to the fact that ode45 has adaptive time stepping and not always the point of integration is a point where the temperature is available. Therefore, these lines should be present in the model to get the proper temperature.

Listing 3.2: Structure of derAIRBUS.yam

```
1 function dchidt=derAirbus(t,chi,Temp, Rho, ArrhLaw,Rgas,time1)
2 dchidt = ArrhLaw.A*Rho.v^(1-ArrhLaw.n)*(Rho.v-Rho.c)^(ArrhLaw.n-1)
   *(1-chi)^ArrhLaw.n*exp(-ArrhLaw.E/(Rgas*T)); %calculates DchiDt
3 end
```

3.2 Managing Materials

The models implement in FiTGA usually use some material properties such as the density. Therefore, it was decided to include a material library in which the properties could be stored for future use. A material can be specified in  **Functions/materials** creating a new file with the name of the material and the properties needed. As an example, Listing 3.3 shows the

content of the file *TACOT.yaml*.

Listing 3.3: Structure of the material file *TACOT.yaml*

```
1 v: 280
2 c: 220
```

3.3 Managing Experimental Files Format

The default input data file format of FiTGA is a *.csv file with three columns (time, temperature and mass loss), but it also accepts other formats such as *.txt/* plt files. The main point is that the files should have a column structure of data using commas (or tabs) as separators (with or without headers). The user can define a specific format and unit conversion in ~~Functions~~/inputDataFormat (and, if needed, modifying the function plt2mat.m for new unit conversions). For the moment only two formats are specified: FiTGA and Netzsch. Listing 3.4 shows the structure of these files.

As said before, FiTGA uses a matrix in which the columns are the variables and the rows the data. If the input files use a different format, it needs to be specified expressing the corresponding column. For example, the default format of Netzsch is: Temperature, time, DSC signal and density. In the format specifier file this order should be specified as `order: [2, 1, 4]`. In other words, the second column of the Netzsch file corresponds to the first one in FiTGA (time); the first of Netzsch to the second of FiTGA (Temperature); and the fourth of Netzsch to the third of FiTGA. In addition, it will automatically change the temperature from °C to K and the time from minutes to seconds.

Listing 3.4: Structure of the input format file *Netzsch.yaml*

```
1 # The order in the original file is temperature , time , (DSC
  no need) , rho .
2 order: [2 , 1 , 4]
3 # Units
4 Temp: C
5 time: min
```

3.4 TGA Curve simulation

There are two ways to simulate TGA data in FiTGA: using input files or a GUI.

3.4.1 Simulate TGA data using input files

In order to simulate TGA data using input files, two files are needed: one to express the values of the different parameters and reactions (*reactions.yaml*), and another one to specify the model,

range of temperatures and other data (*data.yaml*). Examples of these files are provided in Listing 3.5 and 3.6. Once these files are ready, it is needed to change the directory to the folder where these files are located and type in the console the command `TGACurveGeneration`. A `*.csv` file will be generated with the three vectors needed to perform the optimization process: `Time`, `Temperature` and `rhoRatio`.

Listing 3.5: Structure of *reactions.yaml* using as example a two reaction case

```

1 # Reaction 1
2 - {F: 0.12, n: 0, A: 10747, E: 53000, mr: 2.8}
3 # Reaction 2
4 - {F: 0.21, n: 0, A: 60747, E: 105000, mr: 2.2}
```

Listing 3.6: Structure of *data.yaml*

```

1 # Name of the file generated
2 filename: '2law'
3 # Time
4 timeIni: 0
5 timeEnd: 1200
6 nPoints: 100
7 # Temperature
8 TempIni: 293
9 beta : 0.8333
10 # Equation
11 Eq: 'pato'
12 # Material
13 Material: 'TACOT'
```

3.4.2 Simulate TGA data using GUI

To simulate TGA data using the GUI, it is needed to type `TGACurveSimulationGUI` on the command window of Matlab and the GUI will appear. It is designed in such a way that some buttons are not available until some options are defined (material, model and number of reactions). Once these options are defined, a table will appear so the user can input the values for the parameters corresponding to each reaction. After that, the user will be able to plot it, and once the desired results are obtained, it can be saved in a `*.csv` pressing `[generate files!]`. A box dialog will appear if the process is been successful.

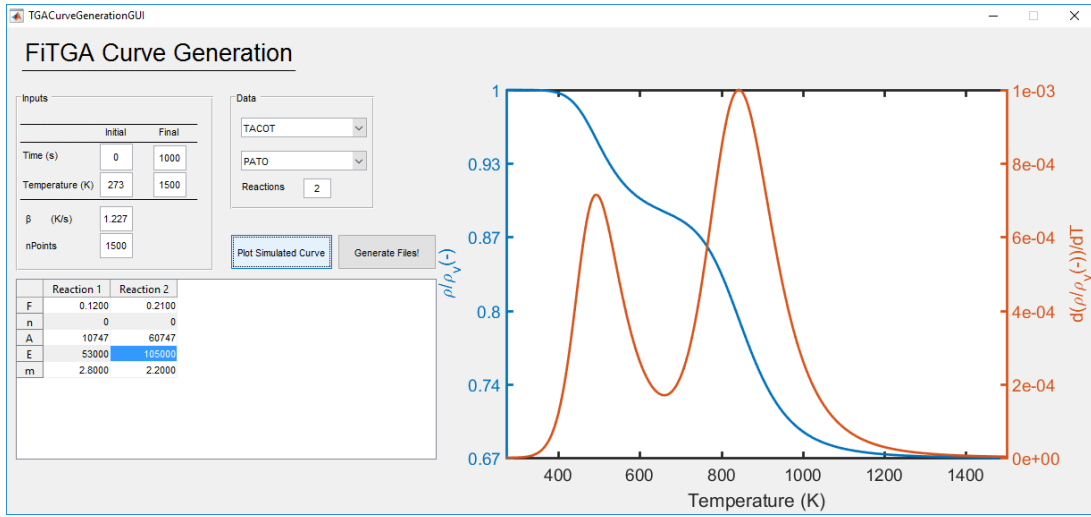


Figure 3.1: GUI to simulate data: example of a two reaction case using PATO as model.

3.5 Preprocessing of TGA experimental data

TGA data can be relatively noisy and usually the time step is very small, which increases the number of experimental points. A high number of experimental points will slow down the curve reconstruction process (because it will take a longer time to calculate the integrals), reducing performance of the code. Therefore, it is usually a good practice to filter the data performing some sampling and smoothing in the preprocessing step. In addition, a specific range of temperatures can be chosen to perform the study.

This preprocessing step can be done in two different ways (as for simulation) using input files or a GUI.

3.5.1 Preprocessing using input files

In the case of using input files, two different files need to be provided: the experimental data, another file specifying the parameters for the preprocessing and the model, algorithm, the number of reactions considered and the format of the input data.

A example of this file is provided in Listing 3.7. Once this files are ready, the preprocessing can be launched writting `preprocessingTGA` in the command window of Matlab.

Listing 3.7: Structure of `data.yaml`

```

1 # Preprocessing
2 file: 'filename.csv'
3 Sampling: 'no'
4 Smoothing: 'Yes'
```

```

5 | TempRange: 'Yes'
6 | Range:
7 | - [0, 3000]
8 | nReactions: 3
9 | Eq: 'pato'
10 | Material: 'TACOT'
11 | Algorithm: 'GA'
12 | InputFormat: 'FitGA'

```

3.5.2 Preprocessing using GUI

In order to simplify the preprocessing step and make it more visual, a GUI has been developed. It can be executed by typing `preprocessingGUI` on the command window. The first thing to do is to input a `*.csv` file using the button `Browse file`. Once the file is loaded, the user should specify which format has the input file and after that some other options will become available. To select a temperature range¹, the user can specify directly the bounds in the text boxes or click on `Select Points` and click on the graph to select the first and last point of the temperature interval.

After that, the user can also define some parameters for the fitting such as the material, model or algorithm. It is also possible to input some parameters and have a first approach using the table provided and pressing the button `Plot Simulated Curve`. Once the user is happy enough with the results, `Generate Files!` can be pressed and the files needed to perform the fitting will be generated: a `*.csv` file with the preprocessed values, a file with the data needed to perform the optimization (`data.yaml`) and a file with the reactions (`guessingPoint.yaml`). This file will have the values provided in the table, the lower and the upper bound². These values should be checked and modified if needed.

The file `data.yaml` generated will have some instructions for the fitting process and for the post processing, all these options can be also modified manually afterwards.

¹If the selected temperature is out of the range, it will take the closest value

²These values are calculated as as percentage of the initial guess (called `start` in the `*.yaml` file and it can be modified in `Functions/boundsPercentage.yaml`).

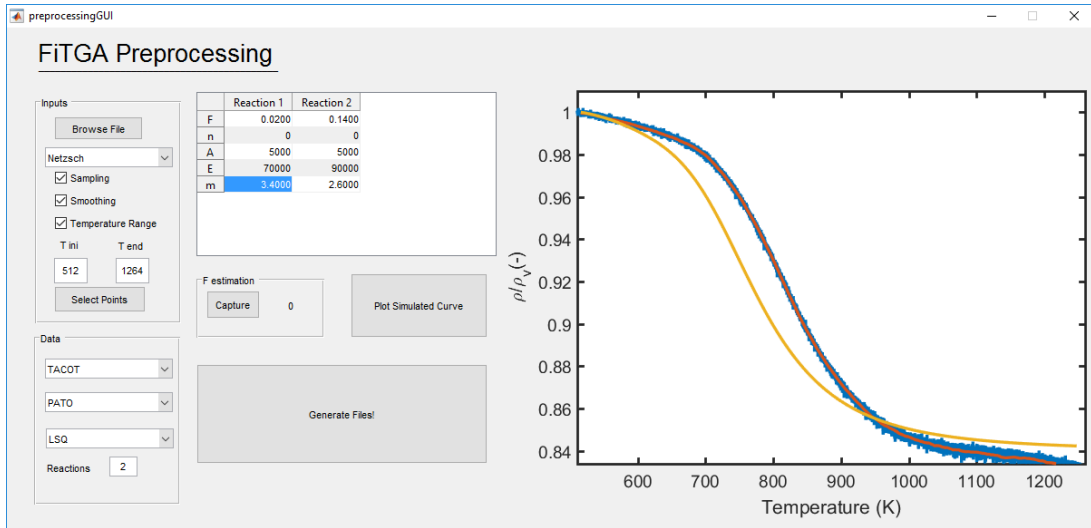


Figure 3.2: Preprocessing GUI. On the graph it can be observed: a) in blue the experimental curve b) in red the preprocessed curve and c) in yellow the first approach to the solution

3.6 Four law fitting of experimental data - *TACOT*

This tutorial consists in fitting experimental data provided by J. Lachaud using a 4-law model[4].

First of all, the data needs to be preprocessed. In order to do so using the GUI, the command `preprocessingGUI` should be typed on the command window. Let's consider a case with curve sampling, smoothing and temperature range between 350 K to 1300 K. The model used to describe this experimental data will be the one proposed by J. Lachaud using a four reaction decomposition approach based on the model proposed by Sykes and explained in [3]. With some ability and previous experience, some values for the initial guess can be given for each parameter, leading to a first approach shown in Figure 3.3.

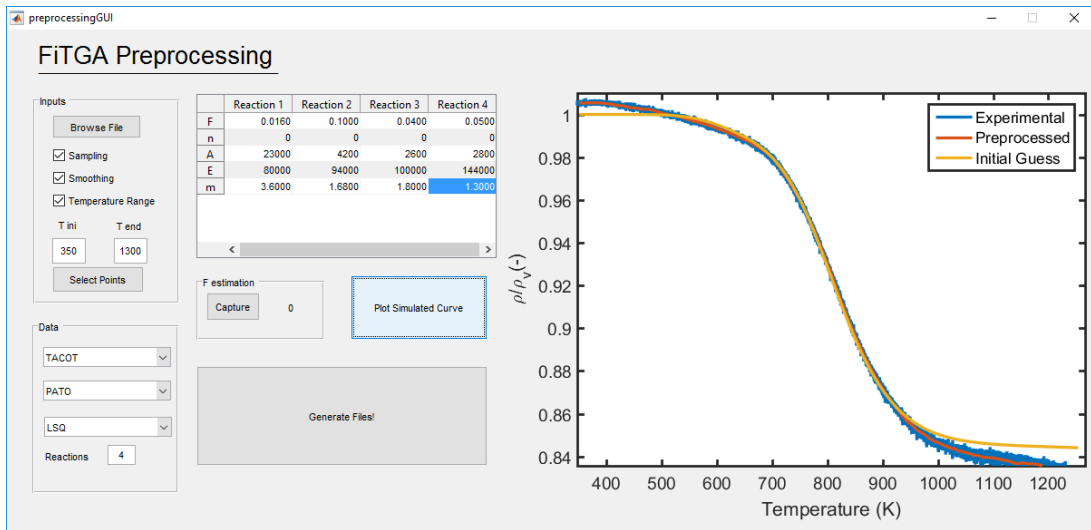


Figure 3.3: Preprocessing of experimental data. On the graph it can be observed: a) in blue the experimental curve b) in red the preprocessed curve and c) in yellow the first approach to the solution

The file *guessingPoint.yaml* should be reviewed. For this model, it should be checked that the variable *m* should not go to values equal or smaller than 1 (for physical reasons) and also it will generate an almost step function which is very hard to solve with `ode45`, therefore a good minimum value for *m* could be 1.3. For the upper boundary, it can be assumed a *m*=5 as a maximum order of reaction. The other variables have good boundaries for this case. The values are shown in Listing 3.8.

Listing 3.8: Guessing Point for TACOT

```

1 lowerBound:
2   - {F: 0.008 ,n: 0,A: 11500 ,E: 40000 ,m: 1.3}
3   - {F: 0.05 ,n: 0,A: 2100 ,E: 47000 ,m: 1.3}
4   - {F: 0.02 ,n: 0,A: 1300 ,E: 50000 ,m: 1.3}
5   - {F: 0.025 ,n: 0,A: 1400 ,E: 97000 ,m: 1.3}
6 start:
7   - {F: 0.016 ,n: 0,A: 23000 ,E: 80000 ,m: 3.6}
8   - {F: 0.1 ,n: 0,A: 4200 ,E: 94000 ,m: 1.68}
9   - {F: 0.04 ,n: 0,A: 2600 ,E: 100000 ,m: 1.8}
10  - {F: 0.05 ,n: 0,A: 2800 ,E: 194000 ,m: 1.3}
11 upperBound:
12  - {F: 0.032 ,n: 0,A: 46000 ,E: 160000 ,m: 5}
13  - {F: 0.2 ,n: 0,A: 8400 ,E: 188000 ,m: 5}
14  - {F: 0.08 ,n: 0,A: 5200 ,E: 200000 ,m: 5}
15  - {F: 0.1 ,n: 0,A: 5600 ,E: 388000 ,m: 5}

```

The contents of the file *data.yaml* are shown in Listing 3.9, in this case it is not necessary to modify it. Nevertheless, the user can modify the different options if needed.

Listing 3.9: Input file for TACOT

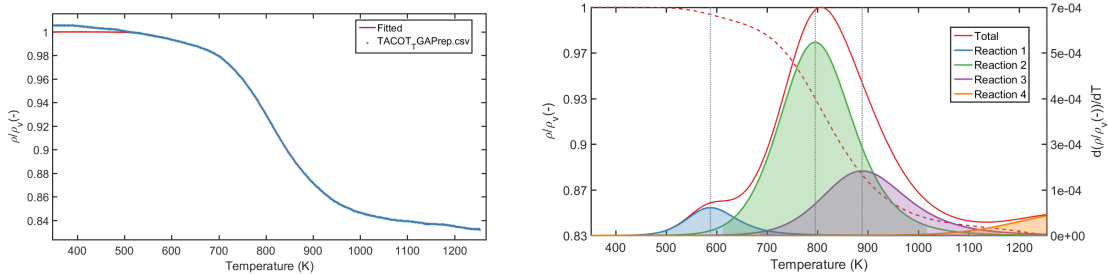
```

1 # Name of the files used
2 files: 'TACOT_TGAPrep.csv'
3 # Equation
4 Eq: PATO
5 # Material
6 Material: TACOT
7 # Solver
8 Algorithm: LSQ
9
10 # PostProcessing
11 Latex: 'yes'
12 Plot: 'yes'
13 Extrapolate: 'no'
14 DecomposeTGA: 'yes'
```

The fitting process can be executed typing **fitting** on the command window. When the process is finished³, it will automatically launch the post processing with the options specified in the *data.yaml* file.

Figure 3.4a shows the both the experimental and the adjusted curve, it can be observed that the adjusted curve follows very precisely the experimental points. Only at the beginning there is a discrepancy but this is due to experimental problems that need further investigation.

Figure 3.4b shows the total differential TGA (DTGA) curve and the different contributions of each reaction to the total. It also shows the TGA curve in red dashed line.



(a) Density ratio evolution: In blue the experimental points, in red the adjusted curve.

(b) Decomposition of the reaction process. In red the totals (dashed line: TGA, solid line DTGA) and in the other colors the different contributions to the total DTGA.

Figure 3.4: Results obtained for TACOT with a 4-reaction model.

³It usually takes about 20 min to compute a case like this one, so you can go and get a coffee.

3.7 Adjusting two simulated curves at the same time

The main objective of this tutorial is to show the capability of FiTGA to perform an optimization process handling several files at the same time⁴.

In order to proceed with this analysis, two simulated curves with three reactions with arbitrary data will be generated using the Airbus model keeping all the parameters as constants but the decomposition F_i .

Figures 3.5a and 3.5b show the inputs for the three reactions in each simulated curve. It can be observed that only small variations have been imposed.

	Reaction 1	Reaction 2	Reaction 3
F	0.0500	0.1000	0.1500
n	2	1.4000	1.5000
A	20000	2500	300
E	40000	60000	90000

	Reaction 1	Reaction 2	Reaction 3
F	0.0550	0.0900	0.1200
n	2	1.4000	1.5000
A	20000	2500	300
E	40000	60000	90000

(a) Input parameters for curve1.

(b) Input parameters for curve2.

Figure 3.5: Three reaction decomposition process using the kinetic model of Airbus

The results obtained using the non linear least squares approach are shown in Table 3.1. Comparing the results obtained using this method with the inputs (see Figure 3.5), it can be observed that the curve recovers input parameters pretty well, there are only small variations for the variables A_i and E_i but the errors are smaller than a 5% in all the cases. The values obtained for the variable F_i (the one that was not kept constant) are more or less in between of F_i imposed in the simulated curves.

Figure 3.6 shows the two simulated data (in green and blue) and the adjusted curve in red. It can be observed that the adjusted curve lays in between of the simulated curves.

Table 3.1: Arrhenius parameters for Adjusted Curve

	Reaction 1	Reaction 2	Reaction 3
F	0.05	0.09	0.13
n	2.01	1.40	1.50
A	20158.15	2604.64	302.39
E	39999.96	60169.75	90054.17

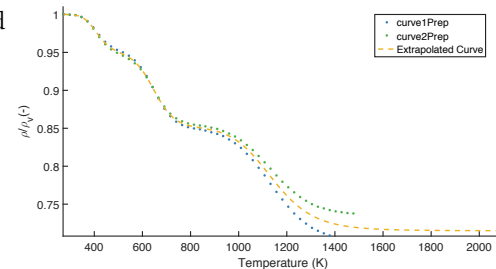


Figure 3.6: Density evolution for the two simulated curves and the adjusted one

⁴For the moment, it is thought that performing several analysis at once will lead to a more robust method than performing the optimization procedures separately and doing a statistical analysis a posteriori

4 Cheating Sheet

TGA data simulation	
<code>TGACurveGeneration</code>	This function is capable of simulating TGA data given two files: <i>reaction.yaml</i> and <i>data.yaml</i> . A tutorial is given in Section 3.4.1.
<code>TGACurveGenerationGUI</code>	This command launches a GUI which facilitates the task of generating simulated TGA data (See Section 3.4.2).
Preprocessing Step	
<code>plt2mat('filename','format')</code>	This function converts a plt or txt file in a mat file. Inputs: <ul style="list-style-type: none">• 'filename': name of the file with extension.• 'format': format of the input files (FiTGA/Netzsch).
<code>preprocessingTGA</code>	Function to preprocess a file with TGA data. It needs a file called <i>preproData.yaml</i> with the instructions needed (see Section 3.5.1).
<code>preprocessingGUI</code>	Launches a GUI which facilitates the preprocessing step, more information is given in Section 3.5.2.
Fitting Step	
<code>fitting</code>	Modify the parameters needed in <i>guessingPoint.yaml</i> and <i>data.yaml</i> created automatically during the preprocessing step. For an example, check Section 3.6.
PostProcess Step	

```
postProcessTGA(folder,  
fileDataVectors, fileArrhLaw)
```

It needs that the input file *data.yaml* used for the fitting includes the instructions needed for postprocessing.

- folder: path to the folder where the outputs will be saved.
 - fileDataVectors: path to the solution *.csv file created at the end of the fitting process.
 - fileArrhLaw: path to the *ArrhLaw.yaml* file with solution parameters.
-